MECHANICS OF PORCINE BRAIN TISSUE: EFFECTS OF STRAIN RATE, REGION, AND ANISOTROPY

by

Gregory Michael Boiczyk

A dissertation submitted to the faculty of
The University of Utah
in partial fulfillment of the requirements for the degree of

Doctor of Philosophy

Department of Biomedical Engineering

The University of Utah

August 2023

The University of Utah Graduate School

STATEMENT OF DISSERTATION APPROVAL

The dissertation of **Gregory Michael Boiczyk**

has been approved by the following supervisory committee members:

Kenneth L. Monson	, Chair	**07/07/2023** Date Approved
Lucas H. Timmins	, Member	**07/11/2023** Date Approved
Jeffrey A. Weiss	, Member	**07/10/2023** Date Approved
Richard D. Rabbitt	, Member	**07/10/2023** Date Approved
Brittany Coats	, Member	**07/06/2023** Date Approved

and by **David W. Grainger**, Chair/Dean of the Department/College/School of **Biomedical Engineering**

and by Darryl P. Butt, Dean of The Graduate School.

ABSTRACT

Traumatic brain injury (TBI) is a significant cause of injury in civilian and military populations. Computational simulations play an important role in developing a deeper understanding of the underlying biomechanics of TBI and evaluating injury criteria and safety measures. The results of these models are highly dependent on the material properties assigned to the various tissue types in the model. Reported material properties of brain tissue vary by several orders of magnitude between studies and are often limited in scope to a single region of the brain and a small range of strain rates, especially at strain rates seen in blast injury. This research aims to quantify the material properties in porcine brain tissue in a range of strain rates and injury modes relevant to conventional and blast TBI. To this end, two studies are presented on the constitutive modeling of porcine brain tissue. In the first study, we tested tissue from adolescent male Göttingen minipigs from the cerebrum, cerebellum, and brainstem in unconfined compression in simple shear at strain rates ranging from quasi-static (QS) to 300 s^{-1}. Using these data, we fit hyper-viscoelastic constitutive models to both compression and shear, which can be readily implemented in existing finite element (FE) software packages. In the second study, we evaluated tissue from the cerebrum and cerebellum in oscillatory shear over a large range of strain rates in one of three directions relative to axon fibers. These data were fit to anisotropic hyper-viscoelastic constitutive models fit

using dynamic inverse FE methods, and the resulting constitutive models can be readily implemented in FE simulations of brain injury.

TABLE OF CONTENTS

LIST OF TABLES

Tables

CHAPTER 1

INTRODUCTION

1.1 Motivation

Traumatic brain injury (TBI) is a major cause of injury and death. In the United States, there were over 220,000 TBI-related hospitalizations resulting in 60,000 deaths in 2019 [1]. TBIs can be caused by various injurious events, with unintentional falls and motor vehicle crashes making up 29.9% and 17% of all US TBI fatalities, respectively. TBI is also a major cause of casualties in modern military conflicts. In an analysis of 2.5 million US service members who served between 2002 and 2021, 17.5% sustained a mild TBI while 3% sustained a moderate or severe TBI, with service members who sustained even a mild TBI having a significantly higher all-cause mortality rate than those who did not, with the fatality rate increasing with TBI severity [2]. Depending on the severity of the injury, TBIs can cause a host of chronic neurological and physiological problems, significantly affecting the victim's quality of life. Even mild TBIs can cause debilitating chronic health problems such as recurring headaches, depression, and post-traumatic stress disorder [3].

Biomechanical evaluation of TBI has been an ongoing field of research for decades [4], producing a large body of work. During this time, experimental evaluation of deformations produced during injury has evolved from relatively simplistic gelatin

models of the brain and skull [5] to neutral density embedded markers which can be visualized via high-speed x-ray during a simulated injury [6]. Additionally, animal models have often been used to evaluate the relationship between potential injurious events and the development of injuries and to evaluate long-term pathologies related to injuries [7, 8].

However, due to the complex geometrical and structural nature of the head and brain, it is difficult to assess injury biomechanics in experimental and animal injury models fully. As a result, finite element (FE) simulations of the tissues of human and animal heads subjected to various simulated injurious loading modes have become a popular tool in studying TBI. Using FE models, authors have examined multiple aspects related to TBI biomechanics, including developing scaling laws between models of injury in different species [9-11], the evaluation of helmets [12-16], the development and evaluation of injury criteria [17-21], the mechanical response of the brain to blast [22-27], and the evaluation of proposed injury mechanisms [24, 28-30]. The biofidelity of these FE models is highly dependent on the material properties used to represent the soft tissues in the models. This is especially evident in brain tissue, where published mechanical properties can vary by several orders of magnitude depending on testing conditions, species, and loading rates [31]. Indeed, FE simulations using the same model geometry and boundary conditions but different brain tissue material properties showed substantially different strain responses [32]. To accurately simulate injurious events, material parameters should be chosen which are derived from experiments that produce similar loading modes and loading rates to those expected in the FE model.

Traumatic brain injury can result from many injuries to the head, from impacts to penetrating injuries to explosive blasts. While many injurious events can cause TBI, a mechanism of considerable interest to this research is primary blast injury caused by high-rate brain tissue deformations due to the shockwave resulting from an explosion. Deformations due to blast injury occur at strain rates far higher than those seen in conventional TBI, with strain rates on the order of several hundred per second in blast injury compared to 10-100 s^{-1} in conventional TBI [33] in humans. In animal models of brain injury, however, strain rates for all injury modes can be substantially increased owing to the smaller brain size. For instance, peak strain rates in simulated impact injuries in porcine brains can reach 235 s^{-1} compared to 65 s^{-1} in human injury models [34]. Compression and tension waves resulting from a blast propagate through the brain at the speed of sound (around 1500 m/s). Within a few milliseconds, the compressive and tensile waves transform into much slower shear waves (on the order of 1-10 m/s), which can then cause tissue deformation for up to hundreds of milliseconds before dissipating [35]. Like most soft tissues, brain tissue is viscoelastic and exhibits substantial rate dependence [36]. As a result, computational models of blast events require material models of soft tissues that have been validated at high strain rates and derived from the brain-simulated species.

1.2 Hypothesis and Objective

The work presented in this dissertation aimed to develop constitutive models of Göttingen minipig brain tissue at rates and loading modes suitable for FE simulations of blast injury. We hypothesized that brain tissue exhibited rate and direction dependence

and differences in mechanical response between the cerebrum, cerebellum, and brainstem. Additionally, we hypothesized that hyper-viscoelastic constitutive model formulations would be able to account for wave propagation observed in high-rate shear experiments on brain tissue if fit using inverse FE methods.

1.3 Overview of Work

In the work presented in this dissertation, we investigated large deformations of Göttingen minipig brain tissue over a large range of strain rates. In Chapter 3, we developed a family of constitutive models suitable for the simulation of blast injury validated at strain rates of 0.02 to 300 s^{-1} in both shear and compression for tissue from the cerebrum, cerebellum, and brainstem. In Chapter 4, we utilized inverse FE models to develop a family of transversely-isotropic hyper-viscoelastic constitutive models for the cerebrum and cerebellum validated at strain rates between 0.025 and 250 s^{-1} can account for large degrees of wave propagation we observed during high-rate oscillatory loading.

1.4 References

[1] Prevention, C.f.D.C.a., *Surveillance Report of Traumatic Brain Injury-Related Deaths by Age Group, Sex, and Mechanism of Injury—United States, 2018 and 2019.* 2022, , U.S. Department of Health and Human Services.

[2] Howard, J.T., et al., Association of Traumatic Brain Injury with Mortality among Military Veterans Serving after September 11, 2001. *JAMA Netw Open*, 2022. **5**(2): e2148150.

[3] Tanielian, T.L., *Invisible Wounds of War : Psychological and Cognitive Injuries, Their Consequences, and Services to Assist Recovery*. 2008, Santa Monica, CA: RAND Corporation.

[4] Goldsmith, W. and K.L. Monson, The State of Head Injury Biomechanics: Past, Present, and Future Part 2: Physical Experimentation. *Crit. Rev. Biomed. Eng.*, 2005. **33**(2): 105-207.

[5] Holbourn, A.H.S., Mechanics of Head Injuries. *The Lancet*, 1943. **242**(6267): 438-441.

[6] Hardy, W.N., et al., A Study of the Response of the Human Cadaver Head to Impact. *Stapp Car Crash J*, 2007. **51**: 17-80.

[7] O'Connor, W.T., A. Smyth, and M.D. Gilchrist, Animal Models of Traumatic Brain Injury: A Critical Evaluation. *Pharmacol Ther*, 2011. **130**(2): 106-13.

[8] Xiong, Y., A. Mahmood, and M. Chopp, Animal Models of Traumatic Brain Injury. *Nat. Rev. Neurosci.*, 2013. **14**(2): 128-42.

[9] Sundaramurthy, A., et al., A 3-D Finite-Element Minipig Model to Assess Brain Biomechanical Responses to Blast Exposure. *Front Bioeng Biotechnol*, 2021. **9**.

[10] Wu, T., et al., Investigation of Cross-Species Scaling Methods for Traumatic Brain Injury Using Finite Element Analysis. *J. Neurotrauma*, 2020. **37**(2): 410-422.

[11] Jean, A., et al., An Animal-to-Human Scaling Law for Blast-Induced Traumatic Brain Injury Risk Assessment. *Proc. Natl. Acad. Sci. U. S. A.*, 2014. **111**(43): 15310-5.

[12] Zhang, L., R. Makwana, and S. Sharma, Brain Response to Primary Blast Wave Using Validated Finite Element Models of Human Head and Advanced Combat Helmet. *Front. Neurol.*, 2013. **4**: 88.

[13] Forero Rueda, M.A., L. Cui, and M.D. Gilchrist, Finite Element Modelling of Equestrian Helmet Impacts Exposes the Need to Address Rotational Kinematics in Future Helmet Designs. *Comput. Methods Biomech. Biomed. Engin.*, 2011. **14**(12): 1021-31.

[14] Tse, K.M., et al., Effect of Helmet Liner Systems and Impact Directions on Severity of Head Injuries Sustained in Ballistic Impacts: A Finite Element (Fe) Study. *Med Biol Eng Comput*, 2017. **55**(4): 641-662.

[15] Fahlstedt, M., P. Halldin, and S. Kleiven, The Protective Effect of a Helmet in Three Bicycle Accidents--a Finite Element Study. *Accid Anal Prev*, 2016. **91**: 135-43.

[16] Jenson, D. and V.U. Unnikrishnan, Energy Dissipation of Nanocomposite Based Helmets for Blast-Induced Traumatic Brain Injury Mitigation. *Composite Structures*, 2015. **121**: 211-216.

[17] Kleiven, S., Evaluation of Head Injury Criteria Using a Finite Element Model Validated against Experiments on Localized Brain Motion, Intracerebral Acceleration, and Intracranial Pressure. *Int. J. Crashworthiness*, 2006. **11**(1): 65-79.

[18] Deck, C. and R. Willinger, Improved Head Injury Criteria Based on Head Fe Model. *Int. J. Crashworthiness*, 2008. **13**(6): 667-678.

[19] Premi, S., et al., Mechanical Threshold for Concussion Based on Computation of Axonal Strain Using a Finite Element Rat Brain Model. *Brain Multiphysics*, 2021. **2**.

[20] Sahoo, D., C. Deck, and R. Willinger, Brain Injury Tolerance Limit Based on Computation of Axonal Strain. *Accid Anal Prev*, 2016. **92**: 53-70.

[21] Wright, R.M. and K.T. Ramesh, An Axonal Strain Injury Criterion for Traumatic Brain Injury. *Biomech. Model. Mechanobiol.*, 2012. **11**(1-2): 245-60.

[22] Wang, C., et al., Computational Study of Human Head Response to Primary Blast Waves of Five Levels from Three Directions. *PLoS One*, 2014. **9**(11): e113264.

[23] Rezaei, A., et al., A Computational Study on Brain Tissue under Blast: Primary and Tertiary Blast Injuries. *Int. J. Numer. Method. Biomed. Eng.*, 2014. **30**(8): 781-95.

[24] Grujicic, M., et al., A Study of the Blast-Induced Brain White-Matter Damage and the Associated Diffuse Axonal Injury. *Multidiscip. Model. Mater.*, 2012. **8**(2): 213-245.

[25] Chafi, M.S., G. Karami, and M. Ziejewski, Biomechanical Assessment of Brain Dynamic Responses Due to Blast Pressure Waves. *Ann. Biomed. Eng.*, 2010. **38**(2): 490-504.

[26] Townsend, M.T., et al., Effect of Tissue Material Properties in Blast Loading: Coupled Experimentation and Finite Element Simulation. *Ann. Biomed. Eng.*, 2019. **47**(9): 2019-2032.

[27] Moore, D.F., et al., Computational Biology - Modeling of Primary Blast Effects on the Central Nervous System. *Neuroimage*, 2009. **47 Suppl 2**: T10-20.

[28] Garimella, H.T., R.H. Kraft, and A.J. Przekwas, Do Blast Induced Skull Flexures Result in Axonal Deformation? *PLoS One*, 2018. **13**(3): e0190881.

[29] Panzer, M.B., et al., Development of a Finite Element Model for Blast Brain Injury and the Effects of Csf Cavitation. *Ann. Biomed. Eng.*, 2012. **40**(7): 1530-1544.

[30] Salzar, R.S., et al., Experimental Investigation of Cavitation as a Possible Damage Mechanism in Blast-Induced Traumatic Brain Injury in Post-Mortem Human Subject Heads. *J. Neurotrauma*, 2017. **34**(8): 1589-1602.

[31] Meaney, D.F., B. Morrison, and C. Dale Bass, The Mechanics of Traumatic Brain Injury: A Review of What We Know and What We Need to Know for Reducing Its Societal Burden. *J. Biomech. Eng.*, 2014. **136**(2).

[32] Zhao, W., B. Choate, and S. Ji, Material Properties of the Brain in Injury-Relevant Conditions - Experiments and Computational Modeling. *J. Mech. Behav. Biomed. Mater.*, 2018. **80**: 222-234.

[33] Bell, E.D., et al., Material Properties of Rat Middle Cerebral Arteries at High Strain Rates. *J. Biomech. Eng.*, 2018.

[34] Wu, T., et al., Evaluation of Tissue-Level Brain Injury Metrics Using Species-Specific Simulations. *J. Neurotrauma*, 2021. **38**(13): 1879-1888.

[35] Przekwas, A., M.R. Somayaji, and R.K. Gupta, Synaptic Mechanisms of Blast-Induced Brain Injury. *Front. Neurol.*, 2016. **7**: 2.

[36] Budday, S., et al., Fifty Shades of Brain: A Review on the Mechanical Testing and Modeling of Brain Tissue. *Arch. Comput. Methods Eng.*, 2019. **27**(4): 1187-1230.

CHAPTER 2

BACKGROUND

2.1 Brain Tissue ECM and Structure

Brain tissue's extracellular matrix (ECM) is unique to other tissues and contains very few structural fibrous proteins, such as collagen. Instead, the ECM is mainly composed of proteoglycans. The ECM primarily consists of a hyaluronan backbone that binds to additional glycoproteins, namely lecticans and tenascins [1, 2]. Due to the high proteoglycan content, brain tissue is highly hydrated and is composed of 68-80% water depending on the brain region [3].

Brain tissue can primarily be classified as either gray matter or white matter. Gray matter consists of neuronal cell bodies and smaller glial cells. White matter consists of axonal projections, which connect neurons in different gray matter regions and glial cells. Most of the axons in white matter, especially those of larger diameters, are wrapped in a fatty sheath [4], which has been shown to contribute to tissue stiffness [5]. Owing to this difference in structure, many authors have demonstrated a significant difference in mechanical response between these regions [6-10]. To adequately isolate white and gray matter samples, these either tested small regions of tissues through indentation or tested tissue from human brains, where white matter and gray matter regions are much larger than those in porcine or ovine brains. Due to the need to test relatively large samples to

reduce boundary conditions in this work and this work's focus on relatively small brains from juvenile Göttingen minipigs, we opted to neglect the influence of white matter or gray matter in tested cerebral or cerebellar samples and instead model the bulk response of the tissue.

2.2 Experimental Methods of Brain Tissue Characterization

Owing to its unique structure, brain tissue is one of the softest tissues in the body, with a shear modulus on the order of one kilopascal [6]. Additionally, brain tissue exhibits substantial viscoelastic effects, showing pronounced strain rate dependence [11-14]. As a result, experimental methods used to quantify the material response of brain tissue should be carefully designed to account for this. It is also important to consider various loading modes when testing brain tissue. In addition to the shear and compression tests which are the focus of the work presented here, other groups have tested brain tissue in tension [6, 12, 15, 16], with Budday et al. demonstrating a notable tension/compression asymmetry [6], as well as in combined shear and compression loading [6, 17]. Considering constitutive models calibrated to these loading modes may be necessary depending on the simulated condition in a given FE model. However, the FE models of blast injury, which informed the work presented here, only required constitutive models calibrated in unconfined compression and simple shear [18], with shear loading particularly important for impulse injuries [19]. Additionally, due to the high ratio of bulk modulus to shear modulus, brain tissue is likely to fail in shear rather than compression [20].

2.2.1 Unconfined Compression of Brain Tissue

A large body of work exists testing brain tissue in unconfined compression, where brain tissue is compressed between two rigid, impermeable platens, but the tissue is not constrained in other dimensions. Many authors focused on low, often quasi-static, rates [6, 7, 21-29] below 1 s^{-1}. Other authors have examined brain tissue in unconfined compression over a larger range of strain rates [11, 30-34], but little examination of brain tissue at strain rates above 100 s^{-1} has been performed. Examination of brain tissue in compression at higher rates (several hundred per second) has been performed by multiple authors [28, 35-37] utilizing split-Hopkinson pressure bars (SHPB). While SHPBs allow the determination of compressive properties of brain tissue at very high rates and high maximum strain levels to be examined, they lack resolution at the lower strain levels seen in blast injury [38], making the results possibly ill-suited for constitutive modeling aimed at simulations of blast.

2.2.2 Simple Shear of Brain Tissue

A similarly large body of work exists examining brain tissue in simple shear. Broadly, shear testing of brain tissue can be broken down into two broad experimental categories: parallel plate shear, where the tissue is adhered (utilizing either adhesives or surface tension) between two plates, which are then displaced relative to one another to produce simple shear, or rheology where tissue is torn through torsional loading.

Authors have conducted shear tests in parallel plate shear as either single ramps or oscillatory frequency sweeps, where tissue is subject to multiple cycles of repeated loading at many different frequencies. In single ramp shear, most authors focused on

relatively low deformations at strain rates below 50 s^{-1} [6, 7, 33, 39], making the resulting models ill-suited for modeling high-rate injuries. For higher strain rates, even fewer papers have been published. Only Haslach et al. [17] and Rashid et al. [40] tested brain tissue in single ramp shear at higher rates, though the rates in these papers still capped out at 100 s^{-1} and 120 s^{-1}, respectively. In oscillatory shear, few authors have examined brain tissue at strain amplitudes and driven frequencies high enough to produce strain rates above 100 s^{-1} [41-43]. Many authors test tissue at strain rates on the order of 1 to 10 s^{-1} [20, 44, 45]. Papers relying on rheological testing [13, 27, 46-50] have tended to test brain tissue at even lower strain rates, with maximum driven frequencies often in the range of about 1-10 Hz (compared to 100 Hz in parallel plate shear) and many papers focusing on characterizing brain tissue at low amplitudes [13, 27, 47-50] (1% shear strain or lower). Regardless of the testing mode, no published data examine brain tissue at strain rates above 120 s^{-1} subject to large deformations.

2.2.3 Other Testing Modes

Additional brain tissue mechanical properties evaluation has been done using indentation [5, 8, 9, 45, 51-58]. Indentation testing allows for the direct probing of regional properties of brain tissue with boundary conditions similar to confined compression [59]. At high strain rates, it is expected that the highly-hydrated brain tissue will behave similarly to biphasic tissues, such as cartilage, which see little fluid flux over short times, thus behaving similarly to an incompressible elastic material [60], suggesting that less complicated unconfined compression experiments are sufficient to model the response of brain tissue at rates seen in injury.

Other authors have quantified the mechanical response of brain tissue using magnetic resonance elastography (MRE) [61-67]. MRE uses low-amplitude vibrations applied to the region of interest to induce shear waves in tissues under an MRI scanner. Velocity information from the propagating shear waves encoded in the MRI data is then used to generate a map of tissue stiffnesses [68] in the region of interest. While the resulting data can reveal information about *in vivo* tissue stiffness in different regions over the whole brain, it has historically been limited to examining either linear viscoelastic or linear elastic effects [59] due to fundamental underlying assumptions. However, recent work has utilized inverse FE models of MRE experiments to fit hyper-viscoelastic constitutive models more traditionally used in TBI simulations [69], though it should be noted that only MRE data acquired at a single rate and deformations on the order of microns were used to fit the model, which may not result in an adequate representation of the brain's response to injurious loading conditions.

2.2.4 Regional Variation

Due to variations in tissue structure, function, and the relative distribution of white and gray matter, it is reasonable to expect material properties to vary between different brain regions. By far, the largest body of work is concerned with testing the cerebrum's mechanical properties, the brain's largest single region. Multiple authors have examined the response of mixed white/gray matter samples from the cerebrum [17, 20, 27, 39-41, 43, 44, 46, 49, 70-72], while other authors have sought to isolate tissue from certain structures in the cerebrum to compare differences not just between white matter and gray matter [7, 13, 44, 45, 73] but also report the differences in properties of different

white matter and gray matter regions [6, 33, 74-77] (e.g., comparing thalamic and cortical gray matter [33]). An even smaller body of work exists examining tissue in the brainstem [13, 17, 21, 39, 42, 56, 78, 79] or cerebellum [17, 39, 56] despite the critical function of these regions and a possible increased risk of injury in them [80, 81].

Works examining tissue from multiple regions with the same testing conditions are limited. MacManus et al. [56] reported that the shear modulus determined by indentations at a rate of 10 s^{-1} was higher in the cerebral cortex than the brainstem medulla, which was stiffer than the cerebellum in porcine brain tissue. Li et al. [39] reported that the brainstem was stiffer than the cerebellum and cerebrum in shear, unconfined compression, and tension. The cerebellum was stiffer than the cerebrum in compression at rates of 0.01 to 50 s^{-1}. Similar to Li, Felfelian et al. [21] reported that tissue from the brainstem tested in unconfined compression at low strain rates was stiffer than tissue from the cerebrum while Eskandari et al. [79] reported that brainstem white matter tested in tension responded similarly to cerebral gray matter when tested perpendicularly to the fiber direction but was stiffer when tested along the fiber direction, suggesting that some regional variation may be explained by anisotropy. The disagreement between the results of MacManus and Li may indicate differences in experimental boundary conditions or the difference in applied deformation magnitude (around 50 μm in the indentation in MacManus et al. vs. several mm in the unconfined compression in Li et al.). Data comparing multiple regions with the same testing conditions is lacking at rates above 50 s^{-1}, necessitating additional research.

2.3 Brain Tissue Anisotropy

Due to the stiffening effect of myelin [5], it is reasonable to assume that white matter exhibits some degree of direction-dependent stiffness, especially in regions where axon fibers are highly aligned, such as the brainstem and corpus callosum. Authors have examined the effects of fiber direction in the highly aligned brainstem [42, 79, 82] but also in cerebral tissue from the corpus callosum [6, 7, 33, 45, 77] and corona radiata [6, 7, 33, 44, 77]. Tissue has been tested in compression [6, 33, 45, 77] as well as tension [6, 33, 79, 82] and shear [6, 7, 33, 42, 44, 45]. Many authors have found that the brain tissue exhibited anisotropy [33, 42, 45]. Jin et al. [33] observed direction dependence in human brain samples taken from the corona radiata in shear but not compression or tension. While there seems to be a slight trend towards tissue being stiffer when stretched or compressed along the fibers, there appears to be a considerable variation between tests, potentially masking any anisotropy. Similarly, Li et al. [77] reported that tissue from the corona radiata did not show a significantly increased storage modulus in low or high-rate compression. However, the means for samples compressed along the fiber direction are higher than those compressed perpendicularly. In contrast, Budday et al. [6] and Nicolle et al. [44] did not see statistically significant direction effects in tissue tested in multiple loading modes or shear, respectively. However, it should be noted that Budday tested tissue at low rates where resulting loads are low, and any anisotropic effects may not be distinguishable from inter-sample variation. Nicolle tested tissue at very low strain magnitudes where anisotropic effects may not be readily apparent. Overall, the literature seems to suggest that brain tissue from regions of highly aligned white matter exhibits

some degree of anisotropy, highlighting the importance of developing constitutive models that account for it.

2.4 Hyperelastic Modeling of Brain Tissue

2.4.1 Finite Deformations

Soft tissues undergo large deformations and exhibit a highly non-linear stress-strain response, making their description inappropriate for the infinitesimal strain and linear elasticity frameworks used to evaluate traditional engineering materials [83]. Instead, quantification of the material response of brain tissue relies on finite strain theory.

It is helpful first to consider the deformation of a material. For any point on a body, we can define the position of any point on a body in its deformed state ($\boldsymbol{x}$) as a relationship between its initial position ($\boldsymbol{X}$) and a displacement vector ($\boldsymbol{u}$) such that $\boldsymbol{x} = \boldsymbol{X} + \boldsymbol{u}$. Using this relationship, we can also define the deformation gradient as $\boldsymbol{F} = \frac{\partial \boldsymbol{x}}{\partial \boldsymbol{X}}$, which produces a second-order tensor. The deformation gradient allows for the isolation of stretches and rotations from rigid body motions as the deformation gradient will resolve to the identity matrix when under rigid body motion alone. If needed, the deformation gradient can be further decomposed into a rotation and a stretch using the identity $\boldsymbol{F} = \boldsymbol{RU} = \boldsymbol{vR}$, where $\boldsymbol{R}$ is a rotation tensor and $\boldsymbol{U}$ and $\boldsymbol{v}$ are stretch tensors in the reference (right) and current (left) configuration, respectively. We can then define the right and left Cauchy-Green tensors as $\boldsymbol{C} = \boldsymbol{F}^T\boldsymbol{F} = \boldsymbol{U}^2$ and $\boldsymbol{B} = \boldsymbol{F}\boldsymbol{F}^T = \boldsymbol{v}^2$.

In constitutive modeling of soft tissues, it is common to further break down the deformation gradient into volumetric (volume preserving) and deviatoric (volume

changing) components such that $\boldsymbol{F} = \boldsymbol{F}_{vol}\widetilde{\boldsymbol{F}}$. The volumetric and deviatoric deformation gradients can then be defined as $\boldsymbol{F}_{vol} = J^{\frac{1}{3}}\boldsymbol{I}$ and $\widetilde{\boldsymbol{F}} = J^{-\frac{1}{3}}\boldsymbol{F}$, where the Jacobian ($J$) is given by $J = \det(\boldsymbol{F})$, and $\boldsymbol{I}$ is the identity matrix. The deviatoric deformation gradient can then be used to calculate deviatoric right and left Cauchy-Green tensors such that $\widetilde{\boldsymbol{C}} = \widetilde{\boldsymbol{F}}^T\widetilde{\boldsymbol{F}}$ and $\widetilde{\boldsymbol{B}} = \widetilde{\boldsymbol{F}}\widetilde{\boldsymbol{F}}^T$.

For analytical solutions of soft tissue deformations, it is common to assume that the tissue tested undergoes a homogeneous deformation, meaning that deformation and strain tensors are independent of coordinates (i.e., the deformation tensor is the same throughout the body) [84]. This assumption allows a single deformation gradient to derive the stress state at any point in the body. For the work in this dissertation, we considered deformations in simple shear and unconfined compression, respectively. Additionally, many soft tissues can be modeled as incompressible. For these deformations, we can define the deformation gradient as $\boldsymbol{F} = \begin{bmatrix} 1 & K & 0 \\ 0 & 1 & 0 \\ 0 & 0 & 1 \end{bmatrix}$ for shear and $\boldsymbol{F} = \begin{bmatrix} 1/\sqrt{\lambda} & 0 & 0 \\ 0 & \lambda & 0 \\ 0 & 0 & 1/\sqrt{\lambda} \end{bmatrix}$, where $K = \frac{x_1 - X_1}{X_2}$ and $\lambda = \frac{x_1}{X_1}$.

2.4.2 Stress Tensors

Three stress tensors are commonly used to represent stress in soft tissue biomechanics. The Cauchy or true stress tensor ($\boldsymbol{T}$) is the current force divided by the current cross-sectional area. First Piola-Kirchoff (1st PK) ($\boldsymbol{P}$) or engineering stress represents the pullback of one of the legs of the Cauchy tensor to the reference configuration and is defined as the current force divided by the reference area. The 1st PK

stress can be related to Cauchy stress by the equation $\boldsymbol{P} = J\boldsymbol{T}\boldsymbol{F}^{-T}$. The final stress measure used is the second Piola-Kirchoff (2nd PK) ($\boldsymbol{S}$) stress which is the pullback of both legs of the Cauchy stress tensor to the reference configuration and is related to the true stress by the equation $\boldsymbol{S} = J\boldsymbol{F}^{-1}\boldsymbol{T}\boldsymbol{F}^{-T}$. This stress does not have a direct physical interpretation but is mathematically convenient when working with strain energy.

2.4.3 Strain Energy Functions

Soft tissues, including the brain, are frequently modeled as hyperelastic materials. Energy in hyperelastic materials is defined by a Helmholtz free energy function. If an isothermal process is assumed, the free energy depends only on the deformation and reduces to the strain energy function $W(\boldsymbol{F})$. The stress in a material for any given deformation can then be obtained from the free energy function by the equation $\boldsymbol{S} = 2\frac{\partial W}{\partial \boldsymbol{C}}$. Strain energy functions are commonly represented as functions of invariants of $\boldsymbol{C}$ which are independent of material coordinate frame rotations such that, by chain rule, $\boldsymbol{S} = 2(\frac{\partial W}{\partial I_1}\frac{\partial I_1}{\partial \boldsymbol{C}} + \frac{\partial W}{\partial I_2}\frac{\partial I_2}{\partial \boldsymbol{C}} + \frac{\partial W}{\partial I_3}\frac{\partial I_3}{\partial \boldsymbol{C}})$, where the invariants $I_1 = tr(\boldsymbol{C})$, $I_2 = \frac{1}{2}[tr(\boldsymbol{C})^2 - tr(\boldsymbol{C}^2)]$, and $I_3 = \det(\boldsymbol{C})$. The 2nd PK stress derived from these equations is commonly pushed forward to either 1st PK or Cauchy stress.

2.4.4 Hyperelastic Models of Brain Tissue

Brain tissue is commonly modeled as either a hyperelastic material or a viscoelastic material with a hyperelastic component. Authors have examined many different hyperelastic models at different strain rates. The most used model used to represent brain tissue in literature is the Ogden model [6, 7, 11, 12, 15, 16, 40, 51, 71, 74-

76, 79] given by the strain energy function $W = \sum_{i=1}^{N} \frac{\mu_i}{\alpha_i^2}\left(\lambda_1^{\alpha_i} + \lambda_2^{\alpha_i} + \lambda_3^{\alpha_i} - 3\right)$, where μ_i is a shear stiffness, α_i is a non-linearity parameter, λ_i are the principle stretches, and N is the number of terms, typically one or two. Authors have also modeled brain tissue using the Mooney-Rivlin model [6, 40, 41, 48-50, 85, 86] given by the strain energy function $W = C_1(I_1 - 3) + C_2(I_2 - 3)$, where C_i are material stiffness parameters. It should be noted that while used by many authors due to its simplicity, the Mooney-Rivlin model will reduce to a linear model with the stress equation $S_{12} = 2(C_1 + C_2)K$ in simple shear, making it ill-suited to capture any non-linearity seen during shear tests [40]. Authors have also modeled brain tissue's isotropic hyperelastic response using the Fung hyperelastic model [11, 12, 15, 16, 40] given by the strain energy function $W = \frac{\mu_0}{2b}\left(e^{b(I_1-3)} - 1\right)$, where μ_0 is the shear modulus and b is a stiffening parameter. Additional evaluation of isotropic constitutive models has also examined models such as the Neo-Hookean and Gent models [6], but they were found to be less able to capture the brain tissue response than the Ogden model. Overall, the Ogden model, especially using the one-term formulation, is widely reported to be the best-performing hyperelastic model [6, 11, 12, 40]. As a result, hyperelastic constitutive modeling in our work was focused on the Ogden model, namely the single-term model. However, additional comparisons were made with the Mooney-Rivlin and two-term Ogden models.

2.4.5 Anisotropic Modeling

The hyperelastic framework used above can be easily modified to account for anisotropic effects. Experimental characterization of brain tissue in regions of white matter with highly aligned axons has demonstrated that the tissue exhibits a preferred

loading direction along which it is stiffest [42], suggesting the tissue can be modeled as a transversely isotropic material. For transverse isotropy, fibers are modeled as running along a unit vector $\boldsymbol{a}^0$, where the material will be stiffest when stretched along this direction. This will lead to a general form of a strain energy function for the material given by $W(\boldsymbol{C}, \boldsymbol{a}^0) = W(I_1, I_2, I_3, I_4, I_5)$, where the pseudo-invariants (I_4, I_5) are given by $I_4 = \boldsymbol{a}^0 \boldsymbol{C} \boldsymbol{a}^0 = \lambda^2$ and $I_5 = \boldsymbol{a}^0 \boldsymbol{C}^2 \boldsymbol{a}^0$, where λ is the fiber stretch vector. In practice, it is common to adopt an additive decomposition of the strain energy [87] between the matrix, fiber, and any matrix/fiber interactions:

$$W(\boldsymbol{C}, \boldsymbol{a}^0) = W_{mat}(I_1, I_2) + W_{fib}(\lambda) + W_{inter}(I_1, I_2, \lambda) \qquad \text{Eq 2.1}$$

2.4.6 Anisotropic Modeling of Brain Tissue

Anisotropic constitutive modeling of brain tissue is more varied in the literature than the modeling of isotropic hyperelasticity. Chatelin et al. [88] used a version of the additive decomposition of the strain energy function in Eq 2.1, with the matrix defined as a Mooney-Rivlin material and the fiber strain energy function given by the equation $\frac{\tilde{\lambda}\left(\partial W^d_{Fibers}\right)}{\partial \lambda}\left(\tilde{\lambda}\right) = \begin{cases} 0, & 0 \le \tilde{\lambda} \le 1 \\ c_3\left(e^{c_4(\tilde{\lambda}-1)} - 1\right), & \tilde{\lambda} \ge 1 \end{cases}$, where $\tilde{\lambda}$ is the deviatoric fiber stretch and c_3, c_4 are material parameters. More recent anisotropic modeling has modeled brain tissue with a modified Holzapfel-Gasser-Ogden (HGO) [89-91] model. This model uses an additive decomposition of matrix and fiber stretch with $W_{mat} = \frac{G}{2}\left(\widetilde{I_1} - 3\right) + K\left(\frac{J^2-1}{4} - \frac{1}{2}\ln(J)\right) + \frac{k_1}{2k_2}\left(e^{k_2 \tilde{E}^2_\alpha} - 1\right)$, where G is the shear modulus, K is the bulk modulus, k_1 is a stress-like parameter, k_2 is a dimensionless scaling parameter, and $\tilde{E}^2_\alpha = \frac{1}{3}(\widetilde{I_1} - 3)$. The fiber strain energy function then takes the form $W_{fib} = \frac{k_1}{2k_2}(e^{k_2 E^2_\alpha} - 1)$,

where $E_\alpha = \kappa(I_1 - 3) + (1 - 3\kappa)(I_4 - 1)$ where κ is a dimensionless fiber dispersion parameter such that at $\kappa = 0$ fibers are perfectly aligned, and at $\kappa = \frac{1}{3}$, fibers are randomly oriented and the response becomes isotropic. This modified HGO form is particularly convenient in FE models incorporating tractography data, as the dispersion value can be directly calculated from fractional anisotropy maps [89]. As generating sample-specific data on axon fiber dispersion was not possible, in Chapter 4, we opted to instead model the matrix as a one-term Ogden material and model the fibers using the exponential-power law material implemented in FEBio [92, 93] with the strain energy function $\widetilde{W}_{fib} = \frac{\xi}{\alpha\beta}(exp\left[\alpha\left(\widetilde{I}_4 - 1\right)^\beta\right] - 1)$, while in Chapter 5 we implemented a version of the model used by Chatelin et al. [88] but used a one-term Ogden model for the matrix component.

2.5 Brain Tissue Rate-Dependent Modeling

2.5.1 Viscoelasticity Overview

Soft tissues, including brain tissue, exhibit viscoelastic behavior, where the tissue exhibits a combination of viscous and elastic properties. Viscoelasticity can result from both solid-state effects (e.g., internal friction [94], the reaction between intracellular components [59], or the breaking and reforming of bonds within a tissue [95]) as well as fluid-solid interactions within the material. Due to the high water content of brain tissue, it is likely that fluid plays an important role, though authors have suggested that solid-state viscoelasticity also plays a role [32, 51]. Brain tissue, like other soft tissues, exhibits strain rate-dependent stiffening [12, 17, 40, 73] and shows noticeable stress relaxation, where measured loads decrease when the tissue is held at a constant strain [6, 12, 40], as

well as creep [96], where the tissue will continue to deform over time when held at a constant load. Brain tissue also exhibits substantial hysteresis [24, 29, 76], where loading and unloading stress-strain curves do not follow the same path.

2.5.2 Linear Viscoelasticity in the Brain

In a viscoelastic material subject to cyclic loading, the stress and strain waveforms will be out of phase by an amount between 0 (purely elastic) and 90 (purely viscous) degrees, with stress leading strain. The strain waveform can be represented by the equation $\varepsilon = \varepsilon_0 e^{i\omega t}$, where ε_0 is the strain amplitude, and ω is the angular frequency, while the stress waveform can be given by $\sigma = \sigma_0 e^{i(\omega t+\phi)}$, where σ_0 is the stress amplitude and $0 \leq \phi \leq 90$ is the phase angle between the stress and strain waveforms. To provide a relative measure of the stiffness of the material, the complex, or dynamic, modulus is given by $G = \frac{\sigma_0}{\varepsilon_0} e^{i\phi}$, though it is commonly referred to by its magnitude $|G| = \frac{\sigma_0}{\varepsilon_0}$. The dynamic modulus can be further broken down into the storage modulus, the elastic portion of the modulus given by $G' = Re(G) = |G|\cos(\phi)$, and the viscous portion of the dynamic modulus, the loss modulus, given by $G'' = Im(G) = |G|\sin(\phi)$ [94]. Additionally, a viscoelastic material's damping or internal friction can be directly calculated as $\tan(\phi) = \frac{G''}{G'}$.

Examination of dynamic, storage, and loss moduli is frequently done in the context of linear viscoelasticity, where the stress and strain response can be represented by discrete element models comprising a series of springs (elastic response) and dashpots (viscous response). While linear viscoelastic models do not adequately represent soft tissues undergoing finite deformations, authors have examined brain tissue using linear

viscoelastic frameworks [44, 47] and have shown to hold for strain magnitudes under 0.2%. Regardless of the overall validity of linear viscoelastic methods, comparison of dynamic, storage, and loss moduli can provide information about the evolution of rate stiffening and energy loss in soft tissues and has previously been used for validation of quasi-linear viscoelastic constitutive models [41, 69].

2.5.3 Quasi-Linear Viscoelasticity

To address specific issues with linear viscoelasticity that arise under finite deformations and especially in soft tissues, Fung [94] developed the theory of quasi-linear viscoelasticity (QLV). QLV represents the stress in a material subject to step displacement as a combination of elastic stress $\boldsymbol{S^e}$ and a reduced relaxation function $G(t)$. Extending this over the entire strain or loading history results in a convolution between the elastic stress and relaxation function. The viscoelastic stress can thus be written as $\boldsymbol{S}(t) = \int_0^t G(t-s)\frac{\partial \boldsymbol{s^e}}{\partial s} ds.$

In deriving the relaxation function, Fung notes that many biological soft tissues display rate independence in hysteresis (specifically the ratio of the area between loading and unloading curves to the area under the curve [97]) over several orders of magnitude, which suggests constant damping. This constant damping cannot be accounted for through discrete element models and requires the development of a relaxation function with a continuous relaxation spectrum. In this work, we adopt a Prony series approximation of the continuous relaxation spectrum derived by Fung, commonly used in FE modeling of soft tissues [87] and the brain [98-101]. The Prony series is given by the equation $G(t) = g_0 + \sum_{i=1}^{N} g_i \exp\left(\frac{-t}{\tau_i}\right)$ where g_0, g_i are viscoelastic parameters, and τ_i

are characteristic time constants. This formulation of viscoelasticity is frequently used successfully in the brain tissue literature [11, 12, 25, 40, 75, 79] and implemented in FE packages [93, 102], making it ideal for use in the inverse fitting of experiments. It is worth noting that Darvish and Crandall [41] observed an inability of a QLV model to predict brain stiffness or phase at higher rates adequately. They demonstrated that a fully non-linear Green-Rivlin model was better at predicting stiffnesses at higher rates but still underpredicted them. However, both stress formulations used to fit these constitutive models (as well as the formulations of QLV presented in this section) neglected inertial effects, which can lead to higher stiffnesses and phase lag at higher rates observed in their experiments. Proper use of viscoelastic models at high rates may need to consider inertial effects, which can be implemented in FE software using a dynamic solver. We also note that the concept of a continuous relaxation spectrum may not hold at higher strain rates and may validate the underlying assumptions of QLV, though this is difficult to properly examine due to the influence of inertial effects.

2.6 Inverse Finite Element Analysis

2.6.1 Inverse Finite Element Modeling of Soft Tissue

Inverse FE modeling has become an increasingly common tool to determine material parameters in the brain. Inverse FE modeling works by attempting to solve a finite element model where the solution to the FE model (in this case the stress measured by a load cell) is known but individual model parameters (in this case constitutive model parameters) are not [93]. This is done by repeatedly running the finite element model with parameters which are adjusted through an optimization algorithm until they

converge, producing the set of parameters which best predict the known solution. Inverse FE models have been used to fit constitutive models of brain tissue based on elastography data [69] and fit a constitutive model for axonal fibers [89]. Several authors have utilized inverse models to optimize material properties from indentation experiments [8, 56, 103, 104]. On larger samples, authors have used inverse FE models to fit hyperelastic models to tensile, compressive, and shear tests of human brain tissue [105], fit hyperelastic models to tensile tests of porcine brain tissue [106], utilized DIC and inverse FE models to fit hyper-viscoelastic models of the brain in compression [21], and develop poroelastic models of brain tissue in compression [32]. In other soft tissues, inverse FE methods have been used to model multiple tissues, including hyperelastic [107] and viscoelastic modeling of muscle tissue [108], as well anisotropic hyperelastic modeling of heart valves [109] and lung tissue [110].

2.6.2 Dynamic Finite Element Analysis

In high-rate loading, consideration of inertial effects may become necessary. While these effects are almost always considered in injury simulations [111-113], they are often ignored when fitting constitutive models. In the work presented in Chapters 3 and 4, we observed some degree of strain wave propagation which our stress formulation used to fit constitutive models could not capture due to the lack of inertial terms. This was especially true in the work in Chapter 4, where large degrees of phase lag and poor fitting at high rates led to the shift from more traditional methods of constitutive model fitting relying on numerical optimizations, which assumed a homogeneous deformation and neglected inertial effects, to inverse FE models of experiments.

For the work in Chapter 4, all FE models were developed using FEBio [92]. For all inverse FE models, the implicit dynamic solver was used. In contrast to the statics solver, the governing equations for the dynamic FE solver include inertial terms, which allow it to account for wave propagation through the material [114, 115]. Additionally, dynamic inverse FE enables us to account for any inhomogeneous deformations that may occur during testing. This is particularly important as wave propagation through the sample will lead to a highly inhomogeneous deformation during high-rate testing.

2.7 References

[1] Ruoslahti, E., Brain Extracellular Matrix. *Glycobiology*, 1996. **6**(5): 489-492.

[2] Burnside, E.R. and E.J. Bradbury, Manipulating the Extracellular Matrix and Its Role in Brain and Spinal Cord Plasticity and Repair. *Neuropathol Appl Neurobiol*, 2014. **40**(1): 26-59.

[3] Fatouros, P.P. and A. Marmarou, Use of Magnetic Resonance Imaging for in Vivo Measurements of Water Content in Human Brain: Method and Normal Values. *J. Neurosurg.*, 1999. **90**(1): 109-15.

[4] Simons, M. and K. Trajkovic, Neuron-Glia Communication in the Control of Oligodendrocyte Function and Myelin Biogenesis. *J. Cell Sci.*, 2006. **119**(Pt 21): 4381-9.

[5] Weickenmeier, J., et al., The Mechanical Importance of Myelination in the Central Nervous System. *J. Mech. Behav. Biomed. Mater.*, 2017. **76**: 119-124.

[6] Budday, S., et al., Mechanical Characterization of Human Brain Tissue. *Acta Biomater.*, 2017. **48**: 319-340.

[7] Prange, M.T. and S.S. Margulies, Regional, Directional, and Age-Dependent Properties of the Brain Undergoing Large Deformation. *J. Biomech. Eng.*, 2002. **124**(2): 244-252.

[8] Kaster, T., I. Sack, and A. Samani, Measurement of the Hyperelastic Properties of Ex Vivo Brain Tissue Slices. *J. Biomech.*, 2011. **44**(6): 1158-1163.

[9] Budday, S., et al., Mechanical Properties of Gray and White Matter Brain Tissue by Indentation. *J. Mech. Behav. Biomed. Mater.*, 2015. **46**: 318-330.

[10] van Dommelen, J.A., et al., Mechanical Properties of Brain Tissue by Indentation: Interregional Variation. *J. Mech. Behav. Biomed. Mater.*, 2010. **3**(2): 158-66.

[11] Rashid, B., M. Destrade, and M.D. Gilchrist, Mechanical Characterization of Brain Tissue in Compression at Dynamic Strain Rates. *J. Mech. Behav. Biomed. Mater.*, 2012. **10**: 23-38.

[12] Rashid, B., M. Destrade, and M.D. Gilchrist, Mechanical Characterization of Brain Tissue in Tension at Dynamic Strain Rates. *J. Mech. Behav. Biomed. Mater.*, 2014. **33**: 43-54.

[13] Chatelin, S., et al., Towards Child Versus Adult Brain Mechanical Properties. *J. Mech. Behav. Biomed. Mater.*, 2012. **6**: 166-173.

[14] Hosseini-Farid, M., et al., Rate-Dependent Constitutive Modeling of Brain Tissue. *Biomech. Model. Mechanobiol.*, 2020. **19**(2): 621-632.

[15] Zhao, H., et al., Mechanical Characterization of Immature Porcine Brainstem in Tension at Dynamic Strain Rates. *Med Sci Monit Basic Res*, 2016. **22**: 6-13.

[16] Li, K., et al., Material Properties and Constitutive Modeling of Infant Porcine Cerebellum Tissue in Tension at High Strain Rate. *PLoS One*, 2015. **10**(4): e0123506.

[17] Haslach, H.W., Jr., J.M. Gipple, and L.N. Leahy, Influence of High Deformation Rate, Brain Region, Transverse Compression, and Specimen Size on Rat Brain Shear Stress Morphology and Magnitude. *J. Mech. Behav. Biomed. Mater.*, 2017. **68**: 88-102.

[18] Sundaramurthy, A., et al., A 3-D Finite-Element Minipig Model to Assess Brain Biomechanical Responses to Blast Exposure. *Front Bioeng Biotechnol*, 2021. **9**.

[19] Goldsmith, W., The State of Head Injury Biomechanics: Past, Present, and Future: Part 1. *Crit. Rev. Biomed. Eng.*, 2001. **29**(5-6): 441-600.

[20] Thibault, K.L. and S.S. Margulies, Age-Dependent Material Properties of the Porcine Cerebrum: Effect on Pediatric Inertial Head Injury Criteria. *J. Biomech.*, 1998. **31**(12): 1119-26.

[21] Felfelian, A.M., et al., Determining Constitutive Behavior of the Brain Tissue Using Digital Image Correlation and Finite Element Modeling. *Biomech. Model. Mechanobiol.*, 2019. **18**(6): 1927-1945.

[22] Begonia, M.T., et al., The Influence of Strain Rate Dependency on the Structure-Property Relations of Porcine Brain. *Ann. Biomed. Eng.*, 2010. **38**(10): 3043-3057.

[23] Karimi, A., S.M. Rahmati, and R. Razaghi, A Combination of Experimental Measurement, Constitutive Damage Model, and Diffusion Tensor Imaging to Characterize the Mechanical Properties of the Human Brain. *Comput. Methods Biomech. Biomed. Engin.*, 2017. **20**(12): 1350-1363.

[24] Prevost, T.P., et al., Biomechanics of Brain Tissue. *Acta Biomater.*, 2011. **7**(1): 83-95.

[25] Cheng, S. and L.E. Bilston, Unconfined Compression of White Matter. *J. Biomech.*, 2007. **40**(1): 117-24.

[26] McCarty, A.K., et al., Influence of Saline Solution Absorption and Compressive Rate on the Material Properties of Brain Tissue. *J. Mech. Behav. Biomed. Mater.*, 2019. **97**: 355-364.

[27] Hrapko, M., et al., Characterisation of the Mechanical Behaviour of Brain Tissue in Compression and Shear. *Biorheology*, 2008. **45**(6): 663-76.

[28] Prabhu, R.K., et al., Compressive Mechanical Properties of Porcine Brain: Experimentation and Modeling of the Tissue Hydration Effects. *Bioengineering*, 2019. **6**(2).

[29] Franceschini, G., et al., Brain Tissue Deforms Similarly to Filled Elastomers and Follows Consolidation Theory. *J Mech Phys Solids*, 2006. **54**(12): 2592-2620.

[30] Tamura, A., et al., Mechanical Characterization of Brain Tissue in High-Rate Compression. *J. Biomech. Sci. Eng.*, 2007. **2**(3): 115-126.

[31] Rashid, B., M. Destrade, and M.D. Gilchrist, Temperature Effects on Brain Tissue in Compression. *J. Mech. Behav. Biomed. Mater.*, 2012. **14**: 113-118.

[32] Hosseini-Farid, M., et al., A Poro-Hyper-Viscoelastic Rate-Dependent Constitutive Modeling for the Analysis of Brain Tissues. *J. Mech. Behav. Biomed. Mater.*, 2020. **102**.

[33] Jin, X., et al., A Comprehensive Experimental Study on Material Properties of Human Brain Tissue. *J. Biomech.*, 2013. **46**(16): 2795-2801.

[34] Li, Z., et al., Compressive Properties and Constitutive Modeling of Different Regions of 8-Week-Old Pediatric Porcine Brain under Large Strain and Wide Strain Rates. *J. Mech. Behav. Biomed. Mater.*, 2019. **89**: 122-131.

[35] Zhang, J., et al., Effects of Tissue Preservation Temperature on High Strain-Rate Material Properties of Brain. *J. Biomech.*, 2011. **44**(3): 391-396.

[36] Sarntinoranont, M., et al., High-Strain-Rate Brain Injury Model Using Submerged Acute Rat Brain Tissue Slices. *J. Neurotrauma*, 2012. **29**(2): 418-29.

[37] Prabhu, R., et al., Coupled Experiment/Finite Element Analysis on the Mechanical Response of Porcine Brain under High Strain Rates. *J. Mech. Behav. Biomed. Mater.*, 2011. **4**(7): 1067-80.

[38] Meaney, D.F., B. Morrison, and C. Dale Bass, The Mechanics of Traumatic Brain Injury: A Review of What We Know and What We Need to Know for Reducing Its Societal Burden. *J. Biomech. Eng.*, 2014. **136**(2).

[39] Li, Z., et al., A Comprehensive Study on the Mechanical Properties of Different Regions of 8-Week-Old Pediatric Porcine Brain under Tension, Shear, and Compression at Various Strain Rates. *J. Biomech.*, 2020. **98**.

[40] Rashid, B., M. Destrade, and M.D. Gilchrist, Mechanical Characterization of Brain Tissue in Simple Shear at Dynamic Strain Rates. *J. Mech. Behav. Biomed. Mater.*, 2013. **28**: 71-85.

[41] Darvish, K.K. and J.R. Crandall, Nonlinear Viscoelastic Effects in Oscillatory Shear Deformation of Brain Tissue. *Med Eng Phys*, 2001. **23**(9): 633-645.

[42] Arbogast, K.B. and S.S. Margulies, Material Characterization of the Brainstem from Oscillatory Shear Tests. *J. Biomech.*, 1998. **31**(9): 801-807.

[43] Gipple, J.M. and H.W. Haslach, Jr., Damage to the Rat Cerebrum under in Vitro Sinusoidal Translational Shear Deformation. *J. Mech. Behav. Biomed. Mater.*, 2020. **110**: 103969.

[44] Nicolle, S., et al., Shear Linear Behavior of Brain Tissue over a Large Frequency Range. *Biorheology*, 2005. **42**(3): 209-223.

[45] Feng, Y., et al., Measurements of Mechanical Anisotropy in Brain Tissue and Implications for Transversely Isotropic Material Models of White Matter. *J. Mech. Behav. Biomed. Mater.*, 2013. **23**: 117-132.

[46] Hrapko, M., et al., The Influence of Test Conditions on Characterization of the Mechanical Properties of Brain Tissue. *J. Biomech. Eng.*, 2008. **130**(3): 031003.

[47] Bilston, L., Z. Liu, and N. Phan-Thien, Linear Viscoelastic Properties of Bovine Brain Tissue in Shear. *Biorheology*, 1997. **34**(6): 377-385.

[48] Brands, D.W.A., P.H.M. Bovendeerd, and G.W.M. Peters, *Finite Shear Behaviour of Brain Tissue under Impact Loading*, in *ASME Symposium on Crashworthiness, Occupant Protection and Biomechanics in Transportation Systems*. 2000. p. 175-188.

[49] Brands, D.W., P.H. Bovendeerd, and G.W. Peters, *Finite Shear Behavior of Brain Tissue under Impact Loading*, in *ASME International Mechanical Engineering Congress and Exposition*. 2000, American Society of Mechanical Engineers: Orlando, Florida, USA. p. 175-88.

[50] Bilston, L., Z. Liu, and N. Phan-Thien, Large Strain Behaviour of Brain Tissue in Shear: Some Experimental Data and Differential Constitutive Model. *Biorheology* 2001. **38**(4): 335-45.

[51] Greiner, A., et al., Poro-Viscoelastic Effects During Biomechanical Testing of Human Brain Tissue. *Front. Mech. Eng.*, 2021. **7**.

[52] Qian, L., et al., Influence of Strain Rate on Indentation Response of Porcine Brain. *J. Mech. Behav. Biomed. Mater.*, 2018. **82**: 210-217.

[53] Qiu, S., et al., Viscoelastic Characterization of Injured Brain Tissue after Controlled Cortical Impact (Cci) Using a Mouse Model. *J. Neurosci. Methods*, 2020. **330**: 108463.

[54] Christ, A.F., et al., Mechanical Difference between White and Gray Matter in the Rat Cerebellum Measured by Scanning Force Microscopy. *J. Biomech.*, 2010. **43**(15): 2986-2992.

[55] Gefen, A. and S.S. Margulies, Are in Vivo and in Situ Brain Tissues Mechanically Similar? *J. Biomech.*, 2004. **37**(9): 1339-1352.

[56] MacManus, D.B., et al., Region and Species Dependent Mechanical Properties of Adolescent and Young Adult Brain Tissue. *Sci. Rep.*, 2017. **7**(1).

[57] Miller, K., et al., Mechanical Properties of Brain Tissue in-Vivo: Experiment and Computer Simulation. *J. Biomech.*, 2000. **33**(11): 1369-1376.

[58] Prevost, T.P., et al., Dynamic Mechanical Response of Brain Tissue in Indentation in Vivo, in Situ and in Vitro. *Acta Biomater.*, 2011. **7**(12): 4090-101.

[59] Budday, S., et al., Fifty Shades of Brain: A Review on the Mechanical Testing and Modeling of Brain Tissue. *Arch. Comput. Methods Eng.*, 2019. **27**(4): 1187-1230.

[60] Ateshian, G.A., B.J. Ellis, and J.A. Weiss, Equivalence between Short-Time Biphasic and Incompressible Elastic Material Responses. *J. Biomech. Eng.*, 2007. **129**(3): 405-12.

[61] Bertalan, G., et al., Biomechanical Properties of the Hypoxic and Dying Brain Quantified by Magnetic Resonance Elastography. *Acta Biomater.*, 2020. **101**: 395-402.

[62] Hiscox, L.V., et al., Standard-Space Atlas of the Viscoelastic Properties of the Human Brain. *Hum. Brain Mapp.*, 2020. **41**(18): 5282-5300.

[63] Zhang, J., et al., Viscoelastic Properties of Human Cerebellum Using Magnetic Resonance Elastography. *J. Biomech.*, 2011. **44**(10): 1909-1913.

[64] Weickenmeier, J., et al., Magnetic Resonance Elastography of the Brain: A Comparison between Pigs and Humans. *J. Mech. Behav. Biomed. Mater.*, 2018. **77**: 702-710.

[65] Kruse, S.A., et al., Magnetic Resonance Elastography of the Brain. *Neuroimage*, 2008. **39**(1): 231-7.

[66] Sack, I., et al., Non-Invasive Measurement of Brain Viscoelasticity Using Magnetic Resonance Elastography. *NMR Biomed.*, 2008. **21**(3): 265-71.

[67] Hamhaber, U., et al., Three-Dimensional Analysis of Shear Wave Propagation Observed by in Vivo Magnetic Resonance Elastography of the Brain. *Acta Biomater.*, 2007. **3**(1): 127-37.

[68] Mariappan, Y.K., K.J. Glaser, and R.L. Ehman, Magnetic Resonance Elastography: A Review. *Clin. Anat.*, 2010. **23**(5): 497-511.

[69] Giudice, J.S., et al., Calibration of a Heterogeneous Brain Model Using a Subject-Specific Inverse Finite Element Approach. *Front Bioeng Biotechnol*, 2021. **9**: 664268.

[70] Haslach, H.W., Jr., L.N. Leahy, and A.H. Hsieh, Transient Solid-Fluid Interactions in Rat Brain Tissue under Combined Translational Shear and Fixed Compression. *J. Mech. Behav. Biomed. Mater.*, 2015. **48**: 12-27.

[71] Coats, B. and S.S. Margulies, Material Properties of Porcine Parietal Cortex. *J. Biomech.*, 2006. **39**(13): 2521-2525.

[72] Donnelly, B.R. and J. Medige, Shear Properties of Human Brain Tissue. *J. Biomech. Eng.*, 1997. **119**(4): 423-432.

[73] Nicolle, S., M. Lounis, and R. Willinger, Shear Properties of Brain Tissue over a Frequency Range Relevant for Automotive Impact Situations: New Experimental Results. *Stapp Car Crash J*, 2004. **48**: 239-258.

[74] Budday, S., et al., Rheological Characterization of Human Brain Tissue. *Acta Biomater.*, 2017. **60**: 315-329.

[75] Budday, S., et al., Towards Microstructure-Informed Material Models for Human Brain Tissue. *Acta Biomater.*, 2020. **104**: 53-65.

[76] Budday, S., et al., Viscoelastic Parameter Identification of Human Brain Tissue. *J. Mech. Behav. Biomed. Mater.*, 2017. **74**: 463-476.

[77] Li, W., D.E.T. Shepherd, and D.M. Espino, Dynamic Mechanical Characterization and Viscoelastic Modeling of Bovine Brain Tissue. *J. Mech. Behav. Biomed. Mater.*, 2021. **114**: 104204.

[78] Ning, X., et al., A Transversely Isotropic Viscoelastic Constitutive Equation for Brainstem Undergoing Finite Deformation. *J. Biomech. Eng.*, 2006. **128**(6): 925-33.

[79] Eskandari, F., et al., Structural Anisotropy Vs. Mechanical Anisotropy: The Contribution of Axonal Fibers to the Material Properties of Brain White Matter. *Ann. Biomed. Eng.*, 2021. **49**(3): 991-999.

[80] Garman, R.H., et al., Blast Exposure in Rats with Body Shielding Is Characterized Primarily by Diffuse Axonal Injury. *J. Neurotrauma*, 2011. **28**(6): 947-59.

[81] Wang, Z., et al., Altered Cerebellar White Matter Integrity in Patients with Mild Traumatic Brain Injury in the Acute Stage. *PLoS One*, 2016. **11**(3): e0151489.

[82] Eskandari, F., et al., The Importance of Axonal Directions in the Brainstem Injury During Neurosurgical Interventions. *Injury*, 2021. **52**(6): 1271-1276.

[83] Fung, Y.C., Elasticity of Soft Tissues in Simple Elongation. *Am. J. Physiol.*, 1967. **213**(6): 1532-44.

[84] Spencer, A.J.M., *Continuum Mechanics*. Dover Books on Physics. 2004, New York: Dover Publications.

[85] Laksari, K., M. Shafieian, and K. Darvish, Constitutive Model for Brain Tissue under Finite Compression. *J. Biomech.*, 2012. **45**(4): 642-646.

[86] Miller, K. and K. Chinzei, Constitutive Modelling of Brain Tissue: Experiment and Theory. *J. Biomech.*, 1997. **30**(11-12): 1115-21.

[87] Puso, M.A. and J.A. Weiss, Finite Element Implementation of Anisotropic Quasi-Linear Viscoelasticity Using a Discrete Spectrum Approximation. *J. Biomech. Eng.*, 1998. **120**(1): 62-70.

[88] Chatelin, S., C. Deck, and R. Willinger, An Anisotropic Viscous Hyperelastic Constitutive Law for Brain Material Finite-Element Modeling. *J Biorheol*, 2012. **27**(1-2): 26-37.

[89] Wu, T., et al., Explicit Modeling of White Matter Axonal Fiber Tracts in a Finite Element Brain Model. *Ann. Biomed. Eng.*, 2019. **47**(9): 1908-1922.

[90] Zhao, W. and S. Ji, White Matter Anisotropy for Impact Simulation and Response Sampling in Traumatic Brain Injury. *J. Neurotrauma*, 2019. **36**(2): 250-263.

[91] Cloots, R.J., et al., Multi-Scale Mechanics of Traumatic Brain Injury: Predicting Axonal Strains from Head Loads. *Biomech. Model. Mechanobiol.*, 2013. **12**(1): 137-50.

[92] Maas, S.A., et al., Febio: Finite Elements for Biomechanics. *J. Biomech. Eng.*, 2012. **134**(1): 011005.

[93] Maas, S.A. and J.A. Weiss. *Febio Theory Manual*. 2007 [cited 2023 2/16/2023]; Available from: https://help.febio.org/docs/FEBioTheory-4-0/.

[94] Fung, Y.C., *Biomechanics: Mechanical Properties of Living Tissues.* 2 ed. 1993, New York: Springer.

[95] Ateshian, G.A., Viscoelasticity Using Reactive Constrained Solid Mixtures. *J. Biomech.*, 2015. **48**(6): 941-7.

[96] Dodgson, M.C.H., Colloidal Structure of Brain. *Biorheology*, 1962. **1**: 21-30.

[97] Fung, Y.C., Structure and Stress-Strain Relationship of Soft Tissues. *Am. Zool.*, 1984. **24**(1): 13-22.

[98] Finan, J.D., et al., Regional Mechanical Properties of Human Brain Tissue for Computational Models of Traumatic Brain Injury. *Acta Biomater.*, 2017. **55**: 333-339.

[99] Sahoo, D., C. Deck, and R. Willinger, Brain Injury Tolerance Limit Based on Computation of Axonal Strain. *Accid Anal Prev*, 2016. **92**: 53-70.

[100] de Rooij, R. and E. Kuhl, Constitutive Modeling of Brain Tissue: Current Perspectives. *Appl. Mech. Rev.*, 2016. **68**(1).

[101] Chafi, M.S., G. Karami, and M. Ziejewski, Biomechanical Assessment of Brain Dynamic Responses Due to Blast Pressure Waves. *Ann. Biomed. Eng.*, 2010. **38**(2): 490-504.

[102] Simulia. *Abaqus Analysis User's Manual*. [cited 2023 2023/03/29]; Available from: http://130.149.89.49:2080/v6.7/books/usb/default.htm?startat=pt05ch17s07abm12.html.

[103] Feng, Y., et al., Characterizing White Matter Tissue in Large Strain Via Asymmetric Indentation and Inverse Finite Element Modeling. *J. Mech. Behav. Biomed. Mater.*, 2017. **65**: 490-501.

[104] MacManus, D.B., et al., Towards Animal Surrogates for Characterising Large Strain Dynamic Mechanical Properties of Human Brain Tissue. *Brain Multiphysics*, 2020. **1**.

[105] Moran, R., J.H. Smith, and J.J. Garcia, Fitted Hyperelastic Parameters for Human Brain Tissue from Reported Tension, Compression, and Shear Tests. *J. Biomech.*, 2014. **47**(15): 3762-3766.

[106] Rashid, B., M. Destrade, and M.D. Gilchrist, Inhomogeneous Deformation of Brain Tissue During Tension Tests. *Comput. Mater. Sci.*, 2012. **64**: 295-300.

[107] Silva, M.E.T., et al., Biomechanical Properties of the Pelvic Floor Muscles of Continent and Incontinent Women Using an Inverse Finite Element Analysis. *Comput. Methods Biomech. Biomed. Engin.*, 2017. **20**(8): 842-852.

[108] Chawla, A., S. Mukherjee, and B. Karthikeyan, Characterization of Human Passive Muscles for Impact Loads Using Genetic Algorithm and Inverse Finite Element Methods. *Biomech. Model. Mechanobiol.*, 2009. **8**(1): 67-76.

[109] Abbasi, M., et al., Characterization of Three-Dimensional Anisotropic Heart Valve Tissue Mechanical Properties Using Inverse Finite Element Analysis. *J Mech Behav Biomed Mater*, 2016. **62**: 33-44.

[110] Maghsoudi-Ganjeh, M., et al., Developing a Lung Model in the Age of Covid-19: A Digital Image Correlation and Inverse Finite Element Analysis Framework. *Front Bioeng Biotechnol*, 2021. **9**: 684778.

[111] Sundaramurthy, A., et al., Blast-Induced Biomechanical Loading of the Rat: An Experimental and Anatomically Accurate Computational Blast Injury Model. *J. Neurotrauma*, 2012. **29**(13): 2352-2364.

[112] Premi, S., et al., Mechanical Threshold for Concussion Based on Computation of Axonal Strain Using a Finite Element Rat Brain Model. *Brain Multiphysics*, 2021. **2**.

[113] Panzer, M.B., et al., Development of a Finite Element Model for Blast Brain Injury and the Effects of Csf Cavitation. *Ann. Biomed. Eng.*, 2012. **40**(7): 1530-1544.

[114] Palmeri, M.L., et al., A Finite-Element Method Model of Soft Tissue Response to Impulsive Acoustic Radiation Force. *IEEE Trans Ultrason Ferroelectr Freq Control*, 2005. **52**(10): 1699-712.

[115] Blank, J.L., et al., Sensitivity of the Shear Wave Speed-Stress Relationship to Soft Tissue Material Properties and Fiber Alignment. *J. Mech. Behav. Biomed. Mater.*, 2022. **125**: 104964.

CHAPTER 3

RATE- AND REGION-DEPENDENT MECHANICAL PROPERTIES OF GÖTTINGEN MINIPIG BRAIN TISSUE IN SIMPLE SHEAR AND UNCONFINED COMPRESSION

Boiczyk, Gregory. M, Pearson, N, Kote, V. B., Sundaramurthy, A., Subramaniam, D. R., Rubio, J. E., Unnikrishnan, G., Reifman, J., Monson, K.L. (February 6, 2023). "Rate- And Region-Dependent Mechanical Properties of Göttingen Minipig Brain Tissue in Simple Shear and Unconfined Compression."

Reprinted with permission from

ASME. J. Biomech Eng. June 2023; 145(6): 061004.

https://doi.org/10.1115/1.4056480

Gregory M. Boiczyk
Department of Biomedical Engineering,
The University of Utah,
36 S. Wasatch Drive,
Salt Lake City, UT 84112
e-mail: g.boiczyk@utah.edu

Noah Pearson
Department of Mechanical Engineering,
The University of Utah,
1495 E 100 S,
Salt Lake City, UT 84112
e-mail: noah.pearson@utah.edu

Vivek Bhaskar Kote
Department of Defense Biotechnology,
High Performance Computing Software Applications Institute,
Telemedicine and Advanced Technology Research Center,
United States Army Medical Research and Development Command,
2405 Whittier Drive, Suite 200,
Frederick, MD 21702;
The Henry M. Jackson Foundation for the Advancement of Military Medicine, Inc.,
6720A Rockledge Drive,
Bethesda, MD 20817
e-mail: vkote@bhsai.org

Aravind Sundaramurthy
Department of Defense Biotechnology,
High Performance Computing Software Applications Institute,
Telemedicine and Advanced Technology Research Center,
United States Army Medical Research and Development Command,
2405 Whittier Drive, Suite 200,
Frederick, MD 21702;
The Henry M. Jackson Foundation for the Advancement of Military Medicine, Inc.,
6720A Rockledge Drive,
Bethesda, MD 20817
e-mail: asundaramurthy@bhsai.org

Dhananjay Radhakrishnan Subramaniam
Department of Defense Biotechnology,
High Performance Computing Software Applications Institute,
Telemedicine and Advanced Technology Research Center,
United States Army Medical Research and Development Command,
2405 Whittier Drive, Suite 200,
Frederick, MD 21702;
The Henry M. Jackson Foundation for the Advancement of Military Medicine, Inc.,
6720A Rockledge Drive,
Bethesda, MD 20817
e-mail: dsubramaniam@bhsai.org

Rate- and Region-Dependent Mechanical Properties of Göttingen Minipig Brain Tissue in Simple Shear and Unconfined Compression

Traumatic brain injury (TBI), particularly from explosive blasts, is a major cause of casualties in modern military conflicts. Computational models are an important tool in understanding the underlying biomechanics of TBI but are highly dependent on the mechanical properties of soft tissue to produce accurate results. Reported material properties of brain tissue can vary by several orders of magnitude between studies, and no published set of material parameters exists for porcine brain tissue at strain rates relevant to blast. In this work, brain tissue from the brainstem, cerebellum, and cerebrum of freshly euthanized adolescent male Göttingen minipigs was tested in simple shear and unconfined compression at strain rates ranging from quasi-static (QS) to 300 s^{-1}. Brain tissue showed significant strain rate stiffening in both shear and compression. Minimal differences were seen between different regions of the brain. Both hyperelastic and hyper-viscoelastic constitutive models were fit to experimental stress, considering data from either a single loading mode (unidirectional) or two loading modes together (bidirectional). The unidirectional hyper-viscoelastic models with an Ogden hyperelastic representation and a one-term Prony series best captured the response of brain tissue in all regions and rates. The bidirectional models were generally able to capture the response of the tissue in high-rate shear and all compression modes, but not the QS shear. Our constitutive models describe the first set of material parameters for porcine brain tissue relevant to loading modes and rates seen in blast injury. [DOI: 10.1115/1.4056480]

[1]Corresponding author.
Manuscript received July 8, 2022; final manuscript received December 9, 2022; published online February 6, 2023. Assoc. Editor: Matthew B. Panzer.

Jose E. Rubio
Department of Defense Biotechnology,
High Performance Computing Software
Applications Institute,
Telemedicine and Advanced Technology
Research Center,
United States Army Medical Research and
Development Command,
2405 Whittier Drive, Suite 200,
Frederick, MD 21702;
The Henry M. Jackson Foundation for the
Advancement of Military Medicine, Inc.,
6720A Rockledge Drive,
Bethesda, MD 20817
e-mail: jrubio@bhsai.org

Ginu Unnikrishnan
Department of Defense Biotechnology,
High Performance Computing Software
Applications Institute,
Telemedicine and Advanced Technology
Research Center,
United States Army Medical Research and
Development Command,
2405 Whittier Drive, Suite 200,
Frederick, MD 21702;
The Henry M. Jackson Foundation for the
Advancement of Military Medicine, Inc.,
6720A Rockledge Drive,
Bethesda, MD 20817
e-mail: gunnikrishnan@i-a-i.com

Jaques Reifman
Department of Defense Biotechnology,
High Performance Computing Software
Applications Institute,
Telemedicine and Advanced Technology
Research Center,
United States Army Medical Research and
Development Command,
2405 Whittier Drive, Suite 200,
Frederick, MD 21702
e-mail: jaques.reifman.civ@mail.mil

Kenneth L. Monson[1]
Department of Mechanical Engineering,
The University of Utah,
1495 E 100 S,
Salt Lake City, UT 84112;
Department of Biomedical Engineering,
The University of Utah,
36 S. Wasatch Drive,
Salt Lake City, UT 84112
email: ken.monson@mech.utah.edu

Introduction

Traumatic brain injury (TBI) is a major cause of injury and death. In the United States (U.S.), TBI is responsible for over two million emergency department visits per year and contributes to the deaths of over 50,000 people, with the incidence of TBI-related emergency department visits in the U.S. increasing in recent years [1]. TBI is also an increasing problem in modern military conflicts, with an estimated 300,000 of the 1.6 million U.S. service members deployed to Iraq and Afghanistan sustaining at least one mild TBI between 2001 and 2007 [2].

Finite element (FE) simulations are an important tool to understand the complex mechanics of TBI [3,4], but the selection and definition of their material models significantly influence their predictions [5]. Clearly, the use of constitutive models not validated for strains and strain rates relevant to TBI may introduce error [6]. Experimental characterization of brain tissue began in the late 1960s. Experiments since have examined a variety of loading modes, directions, and rates; brain regions; and animal species. Properties for some combinations of these variables still need characterization, but it is notable that comparable experimental studies show wide variation in material properties [7]. This

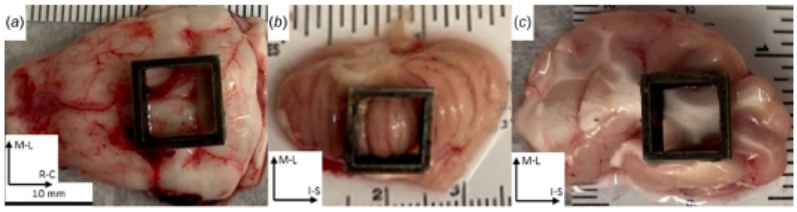

Fig. 1 Custom die and sample harvesting location from: (*a*) brainstem, (*b*) cerebellum, and (*c*) cerebrum. M–L: medial–lateral direction, R–C: rostral–caudal direction, I–S: inferior–superior direction.

variation is evidence of the difficulty of characterizing brain tissue, likely because of its high water content [8,9], relatively soft structure (stiffness of the order of 100–1000 Pa [10]), and strong dependence on strain rate [11–13].

Explosive blast produces complex loading modes in the brain, causing both increased intracranial pressure and shearing [14]. As a result, constitutive models used to study blast TBI should consider both compressive and shear properties of brain tissue. Further, while many investigations of brain tissue include evaluation at high strain rates, most do not include rates relevant to blast exposure. Strain rates in finite element models of human blast events have been reported of the order of ten [15,16] to several hundred per second [17] depending on the model used. Strain rate data from blast simulations on porcine brains is lacking in the literature, but due to the smaller size of the porcine brain it is reasonable to expect rates to be larger than those seen in human brain simulations. Modeling of impact injuries in porcine and human brains has shown that peak strain rates are indeed higher in pigs than humans [18], with peak strain rates being an order of magnitude higher in pigs (up to 235 s^{-1}) compared to humans (up to 65 s^{-1}). Given this, there is a need for the development of validated constitutive models at high strain rates based on experimental data from both shear and compression to aid in modeling both impact and blast injuries.

Few authors have examined the response of brain tissue ramps in simple shear, and most of these studied the tissue at strain rates below 50 s^{-1} ([19–23]). A more substantial body of literature reports the properties of brain tissue in unconfined compression, but like shear, many of these papers focus on lower rates (below 50 s^{-1}) or quasi-static (QS) compression [21–31]. To date, no author has performed the experiments necessary to fully define and model the rate dependent response of brain tissue in both simple shear and unconfined compression over the range of strain rates relevant to blast injury.

Most studies on brain tissue focus on tissue harvested from the cerebrum. Few authors have examined tissue from the brainstem, despite both its physiological importance and its propensity for injury in TBI [32]. The majority of the published brainstem studies tested the tissue in simple shear [22,23,33–35]. No compression data exist for the brainstem above a rate of 50 s^{-1}. In addition, few authors have investigated the material properties of the cerebellum. While the cerebellum is broadly a mix of white and gray matter, much like the cerebrum, material properties measured by magnetic resonance elastography show that the cerebellum is softer than the cerebrum [36], suggesting the need to model it as a separate material. Other authors have examined murine cerebellar tissue exposed to high-rate shear [35] and compression [23,25] as well as porcine and murine tissue using low-rate micro-indentation [37] (producing boundary conditions similar to confined compression [10]). No high-rate data exists for porcine cerebellar tissue in either shear or unconfined compression at strain rates above 50 s^{-1}.

In this study, we deformed brain tissue from the cerebrum, cerebellum, and brainstem of adolescent male Göttingen minipigs in shear and compression at a quasi-static strain rate of 0.02 s^{-1}, an intermediate strain rate of 150 s^{-1}, and a high strain rate of 300 s^{-1}. While strain rates in porcine blast may be higher than the 300 s^{-1} rate, we chose this rate as it was on the upper end of the velocities achievable by our test equipment while allowing for larger tissue samples that minimize the influence of boundary conditions. Tests were conducted with the objective of defining a constitutive model that would be appropriate for blast simulations in these animals. Mooney–Rivlin and both first and second-order Ogden hyperelastic models, each coupled with a one-term Prony series to capture rate dependence, were evaluated as potential constitutive representations of the measured material response. Taken together, this research provides a set of experimentally fit constitutive models appropriate over a wide range of strain rates that can be used in computational simulations of TBI [3].

Methods

Sample Preparation. Thirty-five juvenile (aged 4–5 months) male Göttingen minipigs were euthanized via intravenous phenytoin and pentobarbital. Both the Animal Care and Use Review Office of the U.S. Army Medical Research and Development Command, Fort Detrick, MD, and the Institutional Animal Care and Use Committee at the University of Utah approved all experimental protocols. The braincase was carefully opened with a hammer and chisel. The brain was then freed from the dura and cranial nerves, removed from the skull, and placed in a PEG buffer (7.5% by weight polyethylene glycol in phosphate buffered saline) to minimize swelling relative to the native tissue state [38]. To minimize the potential influence of tissue temperature [31,39], all tissue was stored and tested at room temperature (21 °C).

Tissue samples were harvested from the cerebrum, cerebellum, and brainstem immediately prior to mechanical testing (completed within 8 h of death). The brain was first sectioned into thick (roughly 10 mm) coronal slices and then cut using a custom square die having inner dimensions of 8 mm × 8 mm, with a height of 7 mm for cerebrum and cerebellum samples and 5 mm for brainstem samples. A scalpel was run over the surface of the die to ensure that the surface of the specimen was uniformly cut to the correct height.

Samples from the brainstem (Fig. 1(*a*)) were harvested from the medulla and cut so that the direction of shear was applied in the rostral-caudal direction and compression was applied in the inferior-superior direction. Samples from the cerebellum (Fig. 1(*b*)) were cut so that the direction of shear was applied in the inferior-superior direction and compression applied in the rostral-caudal direction. Samples from the cerebrum (Fig. 1(*c*)) were cut from the corona radiata so that the direction of shear was applied in the inferior-superior direction and compression applied in the rostral-caudal direction. For each brain, 2 to 3 samples were harvested from both the cerebellum and brainstem, and 2 to 4 samples were harvested from the cerebrum, for a total of $n = 8$ samples per group. While the relatively large size of the human brain allows investigators to examine isolated white and gray matter samples [19], studies using smaller animal brains generally test

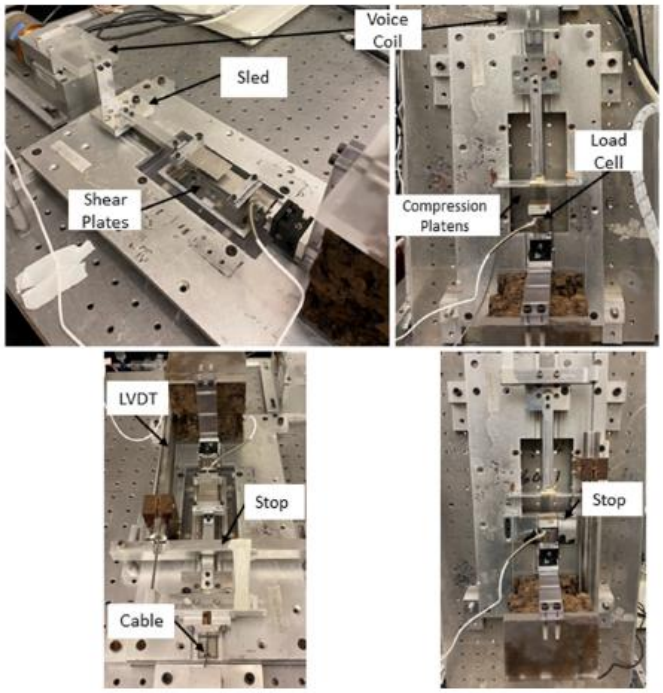

Fig. 2 Tissue testers for quasi-static shear (top left), quasi-static compression (top right), high-rate shear (bottom left), and high-rate compression (bottom right)

mixed white and gray matter samples [11,23–26,28–30,35,40–49] due to size constraints.

Testing Apparatus. Tissue testing was performed on a custom soft tissue tester previously used by our group [50] to test cerebral blood vessels at high strain rates (over $1000\,s^{-1}$). Tissue was mounted (Fig. 2, top row) to produce either shear or compression between the sled and either a 250-gram load cell for shear tests (model 31 Low, Honeywell, Golden Valley, MN) or a 1000-gram load cell for compression tests (model 31 Mid, Honeywell, Golden Valley, MN). Displacement was measured either via a hall effect sensor built into a voice coil (MGV52-25-1.0, Akribis Systems, Singapore) for QS tests or a linear variable differential transformer (LVDT, DC-SE 2000, TE Connectivity, Schaffhausen, Switzerland) and a high-speed camera (Phantom Micro-EX4; Vision Research, Wayne, NJ) for high-rate tests. Sensor data were acquired using a DAQ card capable of simultaneous sampling (PXI-6133, National Instruments, Austin, TX) controlled by a custom program in LABVIEW (National Instruments, Austin, TX).

Using a voice coil actuator directly connected to a low-friction sled, the tester was capable of QS motions, which was directly controllable via a LABVIEW VI. High-rate deformations were achieved by replacing the voice coil with a drop tube (Fig. 2, bottom row) connected to the sled via steel cabling attached to a foam-padded can. Velocities corresponding to strain rates of 150 and $300\,s^{-1}$ were consistently achieved by dropping a mass into the can from a predefined height.

Sample Mounting and Testing. Samples were mounted on the tester after securing the sled in place with a set screw. Prior to mounting, all samples were measured with calipers and photographed. For shear tests, the samples were glued between two parallel shear plates with a thin layer of cyanoacrylate adhesive. For compression tests, the sample was placed on a Teflon tape covered compression platen; no adhesive was used.

Quasi-static shear tests were conducted to deformations of $K = 1$ at a rate of approximately $0.02\,s^{-1}$. For high-rate shear tests, the sled was secured in place with masking tape before loosening the set screw. A steel ball was then dropped from a height of 25 or 81 cm within the drop tube to shear the tissue to failure at a target strain rate of 150 or $300\,s^{-1}$, respectively.

For compression tests, the sled was secured in place with a set screw so that the compression platen was either 1, 10, or 15 mm above the tissue for QS, $150\,s^{-1}$, or $300\,s^{-1}$ tests, respectively. In QS tests, samples were compressed to deformations of 40% at a strain rate of approximately $0.2\,s^{-1}$. For the 150 and $300\,s^{-1}$ tests, the steel ball was dropped from a height of 20 cm, with the difference in velocity controlled by securing the moving platen 10 or 15 mm, respectively, above the fixed platen. An aluminum stop was positioned to arrest high-rate compression 3 mm from the bottom of the tissue, producing maximum compressive deformations of 60% for the brainstem and 43% for the cerebellum and cerebrum.

Data Processing. Noise in the load and displacement signals was smoothed using the Butterworth, 4-pole, phaseless filter

specified in the SAE J211 standard [50] with a cutoff frequency of 81 Hz. Load and displacement data were then converted into First Piola–Kirchoff (first PK) stress. The first PK stress was calculated by dividing the load signal by the cross-sectional area of the tissue, defined as the product of the measured length and width. Deformation was quantified using either the F_{11} (λ) or F_{12} (K) component of the deformation gradient for compression or shear tests, respectively. F_{11} was computed by dividing the measured compressive displacement by the specimen height, while F_{12} was computed by dividing the measured shear displacement by the specimen height.

For each group, an average stress versus deformation curve was created. This was done by interpolating stress values from each test at deformation gradient increments of 0.01 between 0 and 0.35 for shear and 1.0 and 0.7 for compression (0 to 30%), using the *interp1* function in MATLAB (MathWorks, Natick, MA). The upper value for shear was chosen due to tissue failure occurring at about $K = 0.35$ in many high-rate shear tests. For compression, the upper threshold of 0.30 was chosen based on the compression stop height. Average stress values and the corresponding standard deviations at each interpolated point were then determined for each group by averaging the interpolated stress data from individual tests within each group.

Constitutive Modeling. Constitutive models were fit to our experimental data in multiple steps. First, we fit three different hyperelastic models, that have previously been shown to provide good quality fits in brain tissue, to our quasi-static data. For each brain region, we performed unidirectional fits, where shear or compression model parameters were optimized using only shear or compression data (two sets of parameters per region), as well as bidirectional fits, where we required the models to fit both the compression and shear data together (one set of parameters per region). We then used the best-performing hyperelastic model as the basis of a hyper-viscoelastic model, which was optimized across all strain rates, again for both unidirectional and bidirectional fits. All constitutive models chosen here are available in commonly used finite element packages.

Hyperelastic Modeling. Hyperelastic models were fit to the QS experimental data using the one-term and two-term Ogden models [51] and the Mooney–Rivlin model [52]. The one- and two-term Ogden models were chosen due to their previously demonstrated ability to fit brain tissue well [11,19,45], while the Mooney–Rivlin model was chosen to evaluate the response with a simpler constitutive model.

The strain energy function for the N-term Ogden model is given by

$$W_{\mathrm{Ogd}} = \sum_{i=1}^{N} \frac{\mu_i}{\alpha_i^2}\left(\lambda_1^{\alpha_i} + \lambda_2^{\alpha_i} + \lambda_3^{\alpha_i} - 3\right) \tag{1}$$

where λ_i are the principal stretches, and the coefficients $\mu_i \geq 0$ and α_i are the shear moduli and nonlinear stiffening parameters, respectively. The first PK stress expressions then becomes

$$P_{12,\mathrm{Ogd}} = \sum_{i=1}^{N} \frac{\mu_i}{\alpha_i} \frac{1}{\sqrt{1+\frac{K^2}{4}}}\left[\left(\frac{K}{2}+\sqrt{1+\frac{K^2}{4}}\right)^{\alpha_i} - \left(\frac{-K}{2}+\sqrt{1+\frac{K^2}{4}}\right)^{\alpha_i}\right] \tag{2}$$

in shear [11], where K is the F_{12} component of the deformation gradient, and

$$P_{11,\mathrm{Ogd}} = \sum_{i=1}^{N} \frac{2\mu_i}{\alpha_i^2}\left(\lambda^{\alpha_i - 1} - \lambda^{-\left(\frac{\alpha_i}{2}+1\right)}\right) \tag{3}$$

in compression [45], where λ is the stretch value from the F_{11} component of the deformation gradient.

The strain energy function for the Mooney–Rivlin model is given by

$$W_{\mathrm{MR}} = C_1(I_1 - 3) + C_2(I_2 - 3) \tag{4}$$

where $C_1 \geq 0$ and $C_2 \geq 0$ are material constants and I_n is the nth invariant of the right Cauchy-Green tensor $\mathbf{C} = \mathbf{F}^{\mathrm{T}}\mathbf{F}$. The first PK stress expressions for the Mooney–Rivlin model are

$$P_{12,\mathrm{MR}} = 2(C_1 + C_2)K \tag{5}$$

in shear and

$$P_{11,\mathrm{MR}} = 2C_1\left(\lambda^2 - \frac{1}{\lambda}\right) + 2C^2\left(\lambda - \frac{1}{\lambda^2}\right) \tag{6}$$

in compression.

Several different methods were used to fit the hyperelastic models. First, a one-term Ogden model was used to parameterize each stress–strain curve, allowing evaluation of differences in the μ and α parameters between groups. The average stress from each group was then used to fit both the one- and two-term Ogden models, as well as the Mooney–Rivlin model, for each group to generate unidirectional (shear or compression alone) fit parameters. We then optimized model parameters to fit both compression and shear data together, producing a single set of parameters to predict response of brain tissue for both loading modes; we refer to these as bidirectional fits, but it should be clear that no biaxial experiments were conducted. Unidirectional and bidirectional parameter optimizations were performed by minimizing the objective functions defined by Eqs. (7) and (8), respectively, using the *fminsearchbnd* function [53] in MATLAB. For both the unidirectional and bidirectional fits, a grid search was performed over several orders of magnitude on the initial values of fit parameters to reduce the likelihood that the optimizer settled at a local minimum

$$\chi^2_{\mathrm{uni}} = \sum_{i}^{n_s} \frac{(P - P^{\psi})_i^2}{P_{\max}} \tag{7}$$

$$\chi^2_{bi} = \sum_{i}^{n_s} \frac{\left(P_{12} - P_{12}^{\psi}\right)_i^2}{P_{12,\max}} + \sum_{j}^{n_s} \frac{\left(P_{11} - P_{11}^{\psi}\right)_j^2}{P_{11,\max}} \tag{8}$$

Here, P_{ij} is the experimental stress and P_{ij}^{ψ} is the predicted stress.

Hyper-Viscoelastic Modeling. The stress expression for the hyper-viscoelastic function [54] takes the form

$$\mathbf{P}(\mathbf{C}, t) = \int_0^t G(t-s)\frac{d\mathbf{P}^{\mathbf{e}}}{ds}ds \tag{9}$$

where the elastic stress $\mathbf{P}^{\mathbf{e}}(\mathbf{C})$ is given by the one-term Ogden model (Eqs. (1) and (3)), and the relaxation function $G(t)$ is given by a one-term Prony series

$$G(t) = G_\infty + G_1 e^{-\frac{t}{\tau}} \tag{10}$$

where the fit parameters G_∞ and G_1 are constants, which scale the effect of the elastic and viscous response, subject to the constraint

$$G_\infty + G_1 = 1 \tag{11}$$

and the fit parameter τ is a characteristic time scale.

Three versions of the hyper-viscoelastic model were used to fit the two unidirectional and one bidirectional datasets by minimizing the objective functions in Eqs. (7) and (8), respectively, in

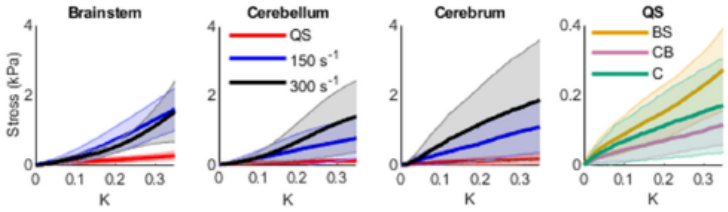

Fig. 3 Average ± standard deviation shear stress verus shear strain (*K*) curves for each region at various strain rates (*n* = 8 per curve; legend in center panel applies to all three panels on left). Note that the QS data are replotted using a different scale to allow better visualization (right panel), BS: brainstem; CB: cerebellum; and C: cerebrum.

Table 1 Pairwise comparisons for shear tests (* indicates statistical significance)

Shear modulus (μ)—strain rate		
QS versus 150 s^{-1} $p < 0.001$*	QS versus 300 s^{-1} $p < 0.001$*	150 versus 300 s^{-1} $p = 0.130$
Nonlinearity coefficient (α)—region		
Brainstem versus cerebellum $p = 0.11$	Brainstem versus cerebrum $p = 0.003$*	Cerebellum versus cerebrum $p = 0.350$

MATLAB. Hyperelastic parameters were fixed to the values determined during the previous quasi-static fitting, so only viscoelastic parameters were allowed to vary during the optimization. Initial values for the viscoelastic parameters were evaluated over several orders of magnitude via a grid search.

Statistical Analysis. For both compression and shear data, statistical analysis was performed on the one-term Ogden parameters that were fit to each sample, such that $n = 8$ sets of parameters were present per group. MANOVA tests were performed for each mode of loading using the dependent variables of stiffness (μ) and nonlinearity (α), with independent variables of strain rate and brain region. Where a statistical difference of $p < 0.05$ was detected, a Tukey Test was performed to examine pairwise differences in either stiffness or nonlinearity between rates and regions.

Results

Shear Testing. The average shear stress–strain data for all brain regions at all rates are presented in Fig. 3 (results for individual samples are shown in Supplemental Figure 1 available in the Supplemental Materials on the ASME Digital Collection.). QS data generally demonstrate a concave-down shape, regardless of tissue region, while the shapes of the high-rate curves were variable. Brainstem behavior was concave-up at both 150 and 300 s^{-1}, where the 300 s^{-1} average demonstrated a larger degree of curvature. The cerebellum showed a concave-down curve for the 150 s^{-1} group and a sigmoidal-like curve for the 300 s^{-1} group, while the cerebrum was concave-down for all groups. Stress levels were comparable between all regions. Cerebrum data showed the greatest amount of scatter, followed by cerebellum; variability was highest in high-rate tests. Additionally, high-rate curves showed a stiffer response than QS curves. Note that for the brainstem the two high-rate curves were similar.

Statistical characterization (Table 1) showed that shear strain rate had a significant effect on μ ($p < 0.001$), with established differences between each of the high rates and the QS rate, but no difference between the two high rates. None of the other variables had a significant effect on μ. The only variable that significantly affected α was brain region ($p = 0.004$), with the comparison between brainstem and cerebrum being significant.

Compression Testing. Average compressive stress–strain curves for all regions and rates are presented in Fig. 4 (results for individual samples are included in Supplemental Figure 2 available in the Supplemental Materials). All results demonstrated a concave-up response. The brainstem showed immediate exponential stiffening as soon as deformations were applied, while the cerebrum and cerebellum did not stiffen until about 10% compression. Stress values (and data scatter) were significantly higher for

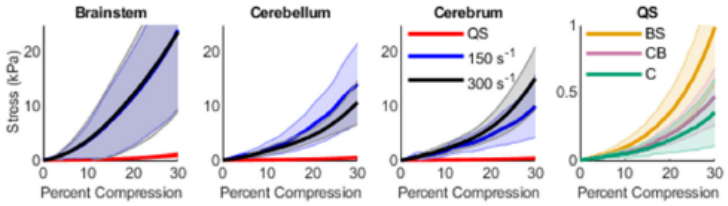

Fig. 4 Average ± standard deviation compressive stress verus percent compression curves for each region at various strain rates (*n* = 8 per curve). Note the change in comparison from strain rate to region in the right most panel.

Table 2 Pairwise comparisons for compression tests (* indicates significance)

Shear modulus (μ)—*Strain rate*		
QS versus 150 s^{-1}	QS versus 300 s^{-1}	150 versus 300 s^{-1}
$p < 0.001$*	$p < 0.001$*	$p = 0.410$

brainstem than for cerebellum and cerebrum, which were similar to one another. It is notable that compressive stress values were an order of magnitude higher than shear stresses. As with the shear data, the high-rate curves were substantially stiffer than the QS curves. For the brainstem, the 150 and 300 s^{-1} curves were not distinct, producing almost identical responses. For the cerebellum, the 150 s^{-1} curve was unexpectedly stiffer than the 300 s^{-1} curve after 12% compression, before which the curves overlap. In contrast, the cerebrum showed a stiffer response in the 300 s^{-1} curve after 12% compression than the 150 s^{-1} curve, prior to which the curves overlap, though none of the observed differences between the high-rate curves were statistically significant.

Statistical evaluation revealed that compressive strain rate, as with shear, had a significant effect on μ ($p < 0.001$), again with established differences between each of the high rates and the QS rate but no difference between the two high rates (Table 2). No other variables had a significant effect on μ, and there were no differences in α between compression groups.

Hyperelastic Modeling of Quasi-Static Shear and Compression. The one- and two-term Ogden models resulted in good quality fits for all regions and loading modes (Supplemental Figures 3 and 4 available in the Supplemental Materials on the ASME Digital Collection). The Mooney–Rivlin model had lower quality fits, especially in compression. For all groups, the one- and two-term Ogden models provided equivalent fits in both shear and compression. The Mooney–Rivlin model performed poorly for all groups, resulting in a linear fit in all cases. The one-term Ogden and Mooney–Rivlin model parameters for each fit are shown in Supplemental Table 1 available in the Supplemental Materials, while the two-term Ogden parameters are shown in Supplemental Table 2 available in the Supplemental Materials.

None of the models fit the combined data (bidirectional fits) as well as they did unidirectional data. For all regions except the cerebrum, the two-term Ogden model performed best (Figs. 5 and 6 and Supplemental Tables 3 and 4 available in the Supplemental Materials). In the cerebrum, the two-term model performed best in shear, but the one-term model performed best in compression. The one-term Ogden model performed almost identically to the two-term model for all regions but the cerebrum. The Mooney–Rivlin model once again performed the poorest, resulting in linear predictions of both shear and compression.

Hyper-Viscoelastic Modeling. As the one-term Ogden model provided almost identical fits to the slightly better performing two-term Ogden model and has 2 less parameters, this model was coupled with a Prony series to simulate the rate dependent (viscoelastic) response of the brain tissue. Unidirectional viscoelastic model fits to data across all strain rates for shear and compression, for each brain region are shown in Figs. 7 and 8, respectively. Model parameters for each of these fits are shown in Table 3. Note that six separate sets of model parameters were derived, one for each combination of brain region and loading mode. Generally, the model was able to capture the response of the experimental data. In particular, it was able to simulate the experimentally observed rate-stiffening behavior for both shear and compression, but the shapes of the predicted curves were not always consistent with the experimental data, at least in shear, likely because these shapes were variable in the experimental data. While model fits showed deviation from experimental values in several cases (most notably in QS shear in the brainstem and cerebellum), the curves remained within one standard deviation of the mean for all cases

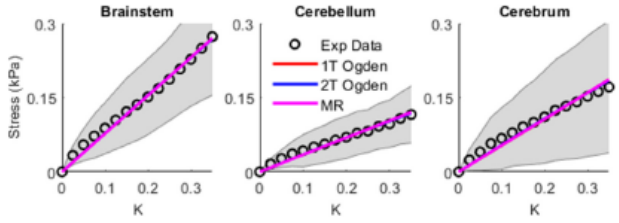

Fig. 5 Bidirectional fits of the quasi-static shear data for the one-term (1T) and two-term (2T) Ogden and Mooney–Rivlin (MR) models

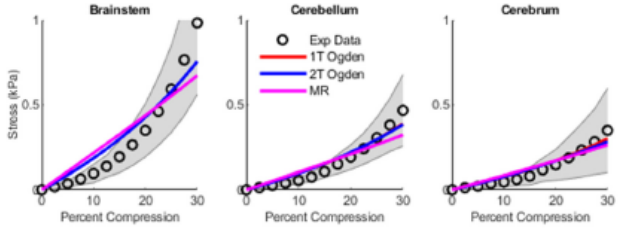

Fig. 6 Bidirectional fits of the quasi-static compression data for the one-term (1T) and two-term (2T) Ogden and Mooney-Rivlin (MR) models

Table 3 Unidirectional viscoelastic model parameters

Region	Loading mode	G_∞	G	τ (s)	μ (Pa)	α	R^2 QS	R^2 150 s^{-1}	R^2 300 s^{-1}
Brainstem	Shear	2.00×10^{-1}	8.00×10^{-1}	8.40×10^{-1}	3.82×10^{3}	1.70×10^{-1}	0.76	0.94	0.86
	Compression	3.04×10^{-2}	9.70×10^{-1}	2.57×10^{-2}	1.51×10^{5}	9.74×10^{0}	0.96	0.99	0.99
Cerebellum	Shear	1.72×10^{-3}	9.98×10^{-1}	1.05×10^{-5}	1.44×10^{5}	9.47×10^{0}	0.74	0.98	0.91
	Compression	3.55×10^{-2}	9.64×10^{-1}	2.42×10^{-2}	6.80×10^{2}	1.00×10^{-1}	0.93	0.85	0.95
Cerebrum	Shear	1.31×10^{-3}	9.99×10^{-1}	8.81×10^{-6}	3.43×10^{5}	7.45×10^{0}	0.88	0.99	0.96
	Compression	2.30×10^{-2}	9.77×10^{-1}	2.38×10^{-3}	8.55×10^{2}	1.00×10^{-1}	0.96	0.94	0.90

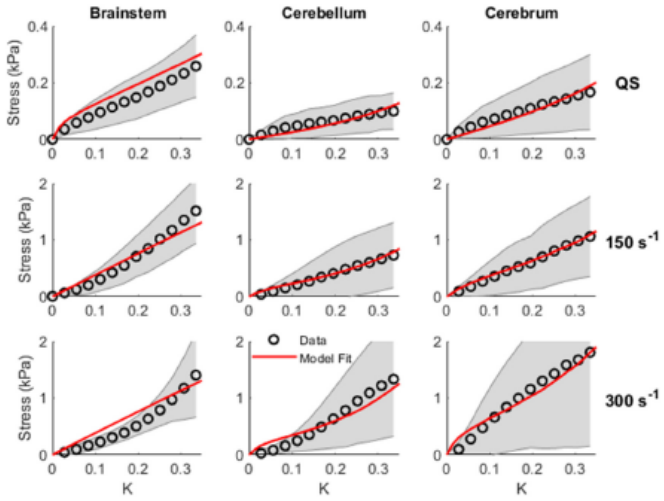

Fig. 7 Unidirectional viscoelastic model fits—shear

except for 300 s^{-1} shear in the brainstem. R^2 values for the viscoelastic fits in shear ranged from 0.74 to 0.99. Compression models generally fit better than shear models, with R^2 values between 0.85 to 0.99. For compression, the lowest R^2 values for each region were the QS rate for the brainstem, 150 s^{-1} for the cerebellum, and 300 s^{-1} for the cerebrum, but all compression curves followed the trends of the experimental data.

Bidirectional viscoelastic model fits are shown in Figs. 9 (shear) and 10 (compression). Corresponding model parameters for the combined shear and compression fits are shown in Table 4. In this case, three sets of model parameters were determined, one for each brain region. The bidirectional fits produced notably worse models than the unidirectional fits. This was especially apparent for brainstem and cerebrum, where the QS shear stress was substantially underpredicted, and for cerebellum, where the QS compressive stress was substantially overpredicted. For the high-rate groups, the model did a better job predicting the stress response in both shear and compression. Still, overprediction can be seen in the cerebellum and cerebrum in shear at 150 s^{-1}, and notable underprediction occurred after compressive stretches of 20% in the cerebellum and cerebrum at high rates. R^2 values for the bidirectional fits in shear ranged from −1.99 to 0.99. The lowest R^2 values in shear for each region were the QS rates for the brainstem and cerebrum and the 150 s^{-1} rate for the cerebellum. In contrast to the unidirectional fits, compression models performed similarly to shear models with R^2 values ranging from −2.75 to 0.98. The lowest R^2 in each compression group corresponded to the QS rate for the brainstem and the cerebellum, and the 300 s^{-1} rate for the cerebrum.

Discussion

The objective of this work was to quantify and model the material behavior of Göttingen minipig brain tissue from the cerebrum, cerebellum, and brainstem in low- and high-rate shear and compression. Results reveal rate stiffening in all regions for both loading modes. The presented viscoelastic model, a combination of a one-term Ogden model and a one-term Prony series, provides a reasonably good fit of the stiffening behavior for shear and compression separately, but it is less accurate when modeling both loading modes together. This is the first study to quantify the response of minipig brain tissue from multiple regions at strain rates relevant to blast injury using a unified set of experimental methods.

Experimental Findings. It is notable that the observed rate stiffening (i.e., dependence of μ on strain rate) across all brain regions and both loading modes was significant in the comparison between both high rates and the QS rate but not between the high rate (150 and 300 s^{-1}) groups. Generally, the 300 s^{-1} group had a slightly larger peak stress than the 150 s^{-1} specimens, but the comparison was not statistically significant. This observation

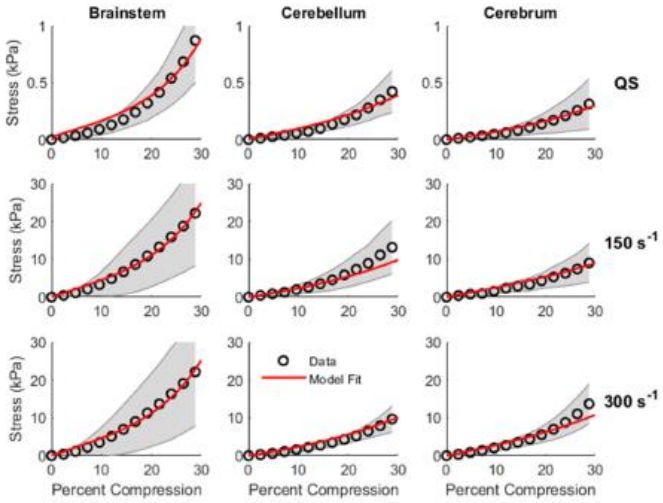

Fig. 8 Unidirectional viscoelastic model fits—compression

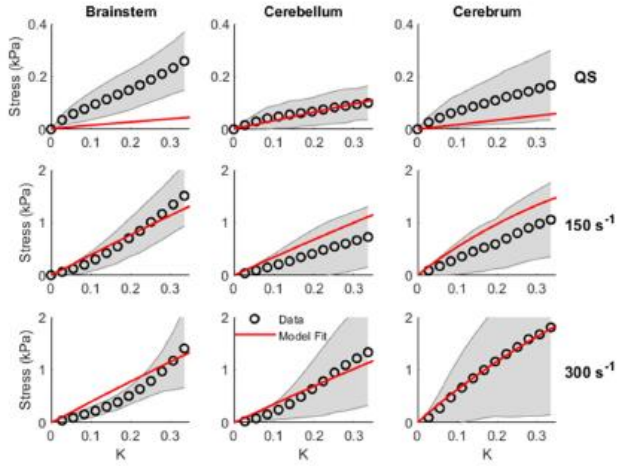

Fig. 9 Bidirectional viscoelastic fits for all shear groups

suggests that rate dependent effects may be lost in observational error between the two high-rate groups, as the $150\,s^{-1}$ rate is several orders of magnitude higher than the $0.02\,s^{-1}$ rate used for QS tests, while being only half the $300\,s^{-1}$ rate. It is also possible that a threshold exists above which the tissue no longer stiffens at increasing strain rates, as suggested by Fung's theory of quasi-linear viscoelasticity [55]. Multiple studies have shown that brain tissue subject to oscillatory shear at low strain levels exhibits a nonlinear increase in dynamic modulus, for which parameters fit at only two strain rates likely would not be able to fully capture [56]. Future work should aim to quantify the response of brain tissue at lower intermediate strain rates to more comprehensively characterize the evolution of rate dependence [11,57].

Shear data displayed notable variability in concavity from group to group, both among regions and rates. This phenomenon was especially apparent in the QS shear experiments. While most tests resulted in a concave-down response, a few in each group demonstrated a concave-up behavior. This concavity variation is also present in experimental shear data in brain tissue from multiple species published by Rashid et al. [11] (porcine), Mihai et al. [58] (human), and Haslach et al. ([35,59]) (murine). Notably, Haslach examined not just simple shear but also shear tests where the

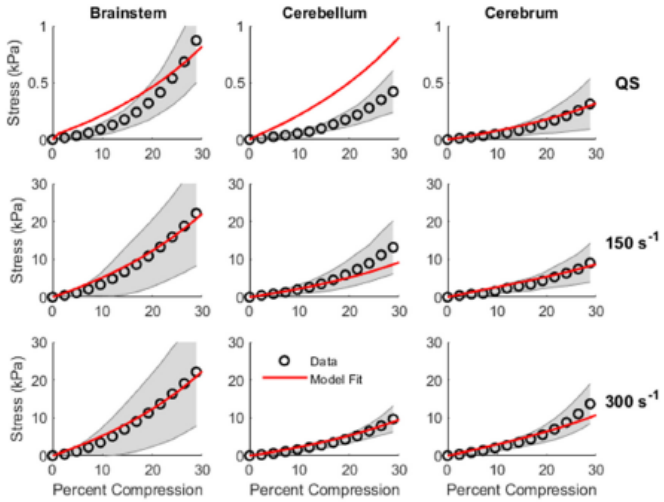

Fig. 10 Bidirectional viscoelastic fits for all compression groups

Table 4 Bidirectional viscoelastic model parameters

Region	Loading mode	G_∞	G	τ (s)	μ (Pa)	α	R^2 QS	R^2 150 s^{-1}	R^2 300 s^{-1}
Brainstem	Shear	3.24×10^{-2}	9.70×10^{-1}	3.72×10^{-2}	3.95×10^{-1}	2.60×10^{-1}	−1.98	0.94	0.84
	Compression						0.87	0.98	0.98
Cerebellum	Shear	9.14×10^{-2}	9.10×10^{-1}	1.94×10^{-2}	3.54×10^{-1}	5.40×10^{-1}	0.93	−0.11	0.93
	Compression						−2.75	0.79	0.96
Cerebrum	Shear	2.37×10^{-2}	9.80×10^{-1}	2.00×10^{-3}	7.32×10^{-1}	7.90×10^{-1}	−1.31	0.20	0.99
	Compression						0.94	0.93	0.89

tissue was subjected to varying degrees of precompression. These experiments showed that tissue subjected to no transverse compression exhibited an initial concave-down response followed by a concave-up response, while samples subjected to transverse compression exhibited a purely concave-down response throughout the test. These results suggest that precompression may have been present for some of our samples. While we attempted to minimize this, a small amount of initial compression was required to get the tissue to adhere to both plates. After lowering the upper plate to generate this force, the plate was again raised to return the tissue to its original height, but our measurement of this was approximate, so it is possible that there was some variability in the degree of tissue compression. Preliminary finite element modeling of quasi-static shear tests subjected to varying degrees of precompression showed increasing softening and a more concave-down stress–strain response as the degree of precompression increased. Considering this, future work should examine this effect, both through additional experiments examining varying degrees of precompression as well as finite element modeling. This is likely to be especially valuable in understanding the response of brain tissue as the tissue seems to expand slightly after it is cut, suggesting that it is under some degree of precompression in vivo.

Constitutive Modeling. For both the unidirectional and bidirectional QS datasets, the best-performing hyperelastic model was the two-term Ogden model, though it was only slightly better at fitting data than the one-term Ogden model. Notably the two-term model performed better or equivalent to the one-term model for all regions but the bidirectional fits for the cerebrum, where the one-term performed best in compression. This appears to largely be a result of the better fit of the two-term model in shear, though fit quality between the one- and two-term models remains close. While all models could not always capture the concavity of the shear tests, the Mooney–Rivlin model was especially unable to do so, as in simple shear it reduced to a linear function. The one-term Ogden models presented by Rashid et al. [11] also showed an inability to fit the initial concavity of shear tests, producing a mostly linear fit. In contrast, the one-term Ogden models presented by Budday et al. [19] showed a greater ability to predict the concavity in shear for unidirectional fitting and in both shear and compression for bidirectional fitting. However, constitutive model fits in that study were only fit to shear strains of $K = 0.2$ and up to 10% compression, compared to the shear strains of $K = 0.0$–0.35 and compressive strains of up to 30% reported here. As the experimental shear data becomes roughly linear at strains above 0.2, the linear region may be influencing fit quality more so than in other studies with lower strains.

Few studies have attempted to model both shear and compressive loading of brain tissue with a single set of parameters. However, both Budday et al. [19,60] and Moran et al. [61] fit tridirectional experimental data from isolated white and gray matter

samples of human brain tissue using shear, tension, and compression data. Interestingly, both groups presented models with a greater fit quality in both shear and compression than shown here. It is possible that this is due to increased variability resulting from the use of mixed white and gray matter samples in our study, as opposed to the isolated gray or white matter samples used by these researchers. Additionally, the inclusion of tensile data in both studies may have contributed to greater fit quality.

In this work, the optimized one-term Ogden model, based on QS shear of cerebrum, resulted in a shear modulus (μ) of 540 Pa and nonlinearity parameter (α) of 1.43×10^{-6}. Several other authors have reported Ogden model fits for porcine cerebral tissue loaded in simple shear at a variety of strain rates. Rashid et al. [11] reported moduli of 1038 Pa at a rate of 30 s^{-1} and 2073 Pa at a rate of 120 s^{-1} (corresponding α values of 2.77 and 3.23). Prange and Margulies [22] reported stiffness values of 296 Pa in thalamic gray matter and 254.2 Pa in corona radiata white matter at a strain rate of 4 s^{-1} (corresponding α values of 0.04 and 0.06), while Coats and Margulies [20] reported stiffnesses of 208 Pa in thalamic gray matter and 190 Pa in white matter from the corona radiata at a rate of 3 s^{-1} (α values of 0.04 and 0.06). As expected, the modulus of our tissue is substantially lower than that of the much higher rate tests performed by Rashid but relatively close to the lower rate tests performed by Coats and Prange. While these tests have lower stiffness values, it is worth noting that they have higher values for α, which may lead to a lower optimized value of μ.

In compression, our reported QS moduli were 5680 Pa in the brainstem, 2890 Pa in the cerebellum, and 2150 Pa in the cerebrum, with corresponding nonlinearity parameters of 14.3, 12.5, and 11.6. Several authors report comparable values for porcine brain tissue loaded at multiple strain rates. Rashid et al. [45] reported moduli of 6000 Pa at 30 s^{-1} and 12642 at 90 s^{-1} (corresponding α values of 0.59 and 5.05), while Singh et al. [62] reported a value of 36 Pa (corresponding α of 9.97) for quasi-static compression. Additionally, Li et al. [63] report shear modulus values, for quasi-static compression of the brainstem, cerebellum, and cerebrum of 8-week old piglets, of 300 Pa, 390 Pa, and 360 Pa, respectively (α values of 7.30, 6.95, and 7.70). Interestingly, our quasi-static results seem most like the 30 s^{-1} results reported by Rashid, with cerebral samples being roughly 1/3rd the stiffness compared to at least an order of magnitude stiffer than the more similar tests performed by Li and Singh. However, it is worth noting that as Li's tests were in piglets, the brain tissue may be substantially softer than in older pigs [56]. Reported material properties for human brains in quasi-static compression [19] show a stiffness of 1630 Pa and a nonlinearity parameter of 16.5, which is similar to the porcine compression properties we report here.

The unidirectional viscoelastic fits were generally able to capture the response of brain tissue at all rates for all regions, especially at higher rates relevant to head trauma. However, these fits still could not capture the response of the tissue in shear, with the poorest performance at QS rates. The shear fits were more linear than the experimental data, especially for the concave-up experimental curves of the brainstem at high rates. Published viscoelastic models for high-rate simple shear of brain tissue over large deformations are limited ([11,64]). These previous studies used stress relaxation data to fit viscoelastic parameters and reported higher levels of fit quality ($R^2 > 0.89$ compared to the $R^2 > 0.74$ seen here). These studies also used higher-order Prony series having more than the two viscous parameters used in this work. Many studies model brain tissue using at least a two-term Prony series [65] in order to capture both the short- and long-time viscous response [34]. However, due to the large difference in strain rates examined here, we opted to use a single term and to allow the QS response to be governed by the G_∞ term in the model, thus reducing the number of parameters needed to be fit and reduce the risk of overfitting.

The viscoelastic models were unable to adequately predict the response of tissue in both compression and shear (bidirectional data), suggesting that additional modeling considerations are needed. Previous work suggests that a biphasic model with a hyper-viscoelastic solid component may be useful [26]. Unfortunately, our experiments were not designed to determine the tissue permeability critical to the biphasic framework [66]. To our knowledge, no models capturing brain response for multiple loading modes at high strain rates have been published to date. However, Wu et al. [67] modeled brain tissue data from shear, compression, and tension tests at strain rates of 0.5 to 30 s^{-1} using a viscoelastic model. They showed relatively good quality fitting in all loading modes but 30 s^{-1} tension, though results from their compression model showed a notable difference in shape compared to experimental data, and their model in shear tended to deviate from experimental results at higher strains. In contrast, our model is generally able to capture the response of brain tissue in both shear and compression over a larger range of strain rates. However, a direct comparison between these models is difficult due to the difference in tested strain rates as well as the inclusion of tensile test data in the Wu model, which is not present in ours. Budday et al. ([60,68]) modeled both shear and compression using a viscoelastic framework based on cyclic shear, compression, and tension experiments, but only at low strain rates. Their models showed substantial underestimation of initial cycles of both shear and compression, similar to what was seen with the models for the QS rates in the cerebrum and brainstem in our work. Interestingly their models showed better predictive accuracy for subsequent conditioned cycles. This suggests that the modeling of viscoelasticity alone may be unable to capture the unconditioned response of brain tissue. It may also be that biaxial data, where the tissue is loaded at various levels of compression and shear simultaneously, would be more useful for developing models that capture both responses.

Other considerations may also improve model performance. For example, approaches which capture anisotropy, possibly by explicitly modeling fiber contributions, may improve the fit quality for shear samples, especially in the brainstem and cerebrum where QS stresses were substantially under-predicted by our isotropic viscoelastic model. Future work should aim to model brain tissue as a biphasic material with viscoelastic reinforcing fibers to better model the physical response of brain tissue in addition to relying on the purely phenomenological viscoelastic and hyperelastic models used here.

Limitations. Our work had several limitations that warrant discussion. First, the experimental stress–strain response includes a significant amount of scatter. This is especially notable in the shear tests of tissue from the cerebellum and cerebrum, though the QS brainstem results also show a large degree of scatter. Li et al. [23] reported standard deviations similar to ours for the brainstem in shear, but our standard deviations for the cerebrum and cerebellum in shear are more than two times higher than theirs for the same tissues. Interestingly, tensile tests from their study show higher spread for the cerebellum than the brainstem or the cerebrum. It is possible that differences in experimental configuration and the exact location of sample harvest from each of the three regions may contribute to this difference.

It is unlikely that the spread seen in our stress and strain data can be explained by outliers that do not necessarily capture the average tissue response. Prior to performing any constitutive model fitting, we performed outlier analysis on the μ and α values of the individual one-term Ogden model fits as well as on the slope of a linear fit to the data from each sample. We plotted all values for each of these parameters in a group together in a boxplot and any sample was excluded if either both the Ogden parameters or the slope of the linear fit was 1.5 times the interquartile range below the 25th percentile value or above the 75th percentile value was excluded if either the stiffness. Test video from all excluded samples was inspected and notable issues with tests such

as poor glue adherence or presence of meninges on the outside of the sample was noted in all excluded tests.

To some degree, this level of variation in the cerebellum and cerebrum is expected because the tissue samples were made up of differing proportions of white and gray matter which were not consistent between samples. Multiple studies have demonstrated a difference in the mechanical properties of white and gray matter [19,37,44,69,70], so different proportions would be expected to introduce variability into the results. The effect of this variation may be especially pronounced in shear compared to compression, because compressive response is expected to be strongly influenced by fluid flux, while shear behavior is likely a direct result of the tissue matrix itself. Additionally, variability in cerebellar and cerebral shear could result in slip planes created by the presence of sulci in the samples. This effect would be especially pronounced in the cerebral samples due to the larger number of sulci in the cerebrum. Future work could aim to quantify and model the response of isolated white and gray matter specimens at high rates either using smaller samples to measure each region independently (though these may be subject to boundary conditions), or attempting to capture the contributions of each through inverse modeling.

As the brainstem is comprised almost entirely of white matter, differing contributions of white and gray matter do not explain the high degree of scatter seen in brainstem tests. Instead, potential sources of error may be due to the influence of anisotropy or precompression. While we attempted to keep the orientation of samples the same, we did not apply any markings to the surface of the tissue sample prior to cutting, so it is possible that some samples may have been tested in a slightly different orientation than others. As the brainstem has been shown to be transversely isotropic [33], this could be partially responsible for the spread seen in the brainstem data, especially in shear. Additionally, as previously mentioned, unintentional precompression of the tissue may lead to a softer response and a change in the shape of the stress–strain curve, further compounding error. High-rate tests appear to have a larger degree of variability than QS tests. In shear, all samples exhibit a higher standard deviation, as a percentage of the mean, at $300\,s^{-1}$ than QS tests, though this is not consistently the case between the QS and $150\,s^{-1}$ groups. This suggests that some source of experimental error may be amplified at $300\,s^{-1}$, potentially due to an increased level of vibration in the tester.

An additional source of error in this work may be due to variations in sample geometry. Due to the ultrasoft nature of brain tissue and the complex geometry of the brain, cutting uniformly sized and shaped samples proved difficult, and brain tissue samples would often slightly deform in an unpredictable way once removed from the tissue punch, though we attempted to minimize swelling by using the PEG buffer. While sample measurements were taken after the tissue was removed from the punch, and either glued to one of the two shear platens or placed on the compression platen, some degree of creep may have also occurred prior to testing. Tissue dimension measurements and stress calculations also relied on the assumption that samples were a perfect cuboid, which is likely not the case. To deal with both inhomogeneous deformations and inconsistent sample geometry, future experiments should be designed to capture fiducial markers on multiple planes of the specimen and used to generate a deformation map using digital image correlation (DIC) before fitting a constitutive model using inverse finite element methods. DIC coupled with inverse finite element modeling has been demonstrated as an effective way to fit anisotropic hyper-viscoelastic models of the brainstem in low-rate compression [71] as well as hyperelastic models of soft tissue phantoms [72] and lung tissue [73].

Test videos suggested that induced deformations were not perfectly homogeneous, due to both boundary conditions and inertial effects at high rates. Evaluation of shear test video showed some degree of deformation inhomogeneity at lower strain levels ($K \leq 0.05$), with areas closer to the moving plate appearing to begin moving several frames before the rest of the tissue. This phenomenon was evident in both QS and high-rate tests for all tested regions. As the level of applied strain increased, the tissue generally began to respond more uniformly. In compression, sample deformation was uniform in QS tests, consistent with a lack of boundary effects on the Teflon-coated platens. At high rates, some samples expanded laterally more at the top (moving) platen than bottom (fixed) platen. No obvious wave propagation was observed in the high-rate shear test videos, but preliminary finite element analysis showed clear stress wave propagation in high-rate simulations in both shear and compression, suggesting that high-rate deformations were not homogenous as assumed. The DIC and inverse modeling approach suggested in the previous paragraph may help clarify this in future research.

Finally, this work did not address anisotropy of the brain tissue. Brain stiffness has been shown to correlate with myelin content [48], which may lead to axons acting as reinforcing fibers and associated anisotropy in aligned regions of the brain. Other studies have previously shown that the brainstem exhibits transversely isotropic behavior in shear [33], though anisotropy in other regions of the brain remains poorly defined, with some authors finding cerebral white matter to exhibit direction dependence [21,39,64,74] and others reporting no direction dependence [19,75,76]. Due to the physiological importance of the brainstem as well as the susceptibility of these regions to diffuse axonal injury in blast [77], future work should aim to better quantify the response of brain tissue in multiple loading directions.

Conclusion

The work presented here comprises the first set of experimentally derived constitutive models for minipig cerebrum, cerebellum, and brainstem in response to simple shear and unconfined compression at rates consistent with blast exposure. Our results show that the response of brain tissue can be well modeled in either compression or shear over a range of strain rates using a hyper-viscoelastic model with a one-term Ogden hyperelastic component. Bidirectional models, which fit both shear and compression data to a single set of parameters, generally perform worse, suggesting additional parameters may be needed to capture the compression and shear response together.

Disclaimer

The opinions and assertions contained herein are the private views of the authors and are not to be construed as official or as reflecting the views of the U.S. Army, the U.S. Department of Defense (DoD), or The Henry M. Jackson Foundation for the Advancement of Military Medicine, Inc. (HJF). This paper has been approved for public release with unlimited distribution.

Funding Data

- National Science Foundation (Award No. 2027367; Funder IDs: 10.13039/100000001 and 10.13039/100000147).
- U.S. Army Medical Research and Materiel Command (Award No. W81XWH-17-2-0008; Funder IDs: 10.13039/100000182 and 10.13039/100016156).
- U.S. DoD (Funder ID: 10.13039/100000005).
- U.S. Army Military Operational Medicine Research Program Area Directorate (Funder ID: 10.13039/100000090).

Nomenclature

$\mathbf{C}$ = right Cauchy-Green tensor
C_1 and C_2 = coefficients of the Mooney–Rivlin hyperelastic model (Pa)
$\mathbf{F}$ = deformation gradient
G_∞ = long term time response coefficient of the viscoelastic model

G_1 = viscoelastic coefficient scaling response at relaxation time τ
K = amount of shear defined as the component of $\mathbf{F}$ in the 1,2 (shear) direction
I_1 and I_2 = first and second invariants of $\mathbf{C}$
P = first Piola–Kirchoff (first PK) stress (Pa)
W = strain energy
μ = Ogden hyperelastic model stiffness coefficient (Pa)
λ = component of $\mathbf{F}$ in the 1,1 (compressive) direction
α = Ogden hyperelastic model non-linearity coefficient
λ_i = ith principle strain
χ = objective function value
t = time (s)
τ = relaxation time

Subscripts and Superscripts

bi = bidirectional
e = elastic
max = maximum value
MR = Mooney–Rivlin hyperelastic model
Ogd = n-term Ogden hyperelastic model
uni = unidirectional
ψ = predicted value

Acronyms and Abbreviations

BS = brainstem
CB = cerebellum
C = cerebrum
First PK = first Piola-Kirchoff stress
MR = Mooney–Rivlin hyperelastic model
PEG = polyethylene glycol
QS = quasi-static
TBI = traumatic brain injury
1T Ogden = one-term Ogden hyperelastic model
2T Ogden = two-term Ogden hyperelastic model

References

[1] Taylor, C. A., Bell, J. M., Breiding, M. J., and Xu, L., 2017, "Traumatic Brain Injury-Related Emergency Department Visits, Hospitalizations, and Deaths - United States, 2007 and 2013," MMWR Surveill. Summ., 66(9), pp. 1–16.
[2] Tanielian, T. L., 2008, *Invisible Wounds of War: Psychological and Cognitive Injuries, Their Consequences, and Services to Assist Recovery*, RAND Corporation, Santa Monica, CA.
[3] Sundaramurthy, A., Kote, V. B., Pearson, N., Boiczyk, G. M., McNeil, E. M., Nelson, A. J., Subramaniam, D. R., et al., 2021, "A 3-D Finite-Element Minipig Model to Assess Brain Biomechanical Responses to Blast Exposure," Front. Bioeng. Biotechnol., 9, p. 757755.
[4] Sundaramurthy, A., Alai, A., Ganpule, S., Holmberg, A., Plougonven, E., and Chandra, N., 2012, "Blast-Induced Biomechanical Loading of the Rat: An Experimental and Anatomically Accurate Computational Blast Injury Model," J. Neurotrauma, 29(13), pp. 2352–2364.
[5] Zhao, W., Choate, B., and Ji, S., 2018, "Material Properties of the Brain in Injury-Relevant conditions - Experiments and Computational Modeling," J. Mech. Behav. Biomed. Mater., 80, pp. 222–234.
[6] Unnikrishnan, G., Mao, H., Sundaramurthy, A., Bell, E. D., Yeoh, S., Monson, K., and Reifman, J., 2019, "A 3-D Rat Brain Model for Blast-Wave Exposure: Effects of Brain Vasculature and Material Properties," Ann. Biomed. Eng., 47(9), pp. 2033–2044.
[7] Meaney, D. F., Morrison, B., and Bass, C. D., 2014, "The Mechanics of Traumatic Brain Injury: A Review of What we Know and What we Need to Know for Reducing Its Societal Burden," ASME J. Biomech. Eng., 136(2), p. 021008.
[8] Sood, D., Chwalek, K., Stuntz, E., Pouli, D., Du, C., Tang-Schomer, M., Georgakoudi, I., Black, L. D., and Kaplan, D. L., 2016, "Fetal Brain Extracellular Matrix Boosts Neuronal Network Formation in 3D Bioengineered Model of Cortical Brain Tissue," ACS Biomater. Sci. Eng., 2(1), pp. 131–140.
[9] Ruoslahti, E., 1996, "Brain Extracellular Matrix," Glycobiology, 6(5), pp. 489–492.
[10] Budday, S., Ovaert, T. C., Holzapfel, G. A., Steinmann, P., and Kuhl, E., 2020, "Fifty Shades of Brain: A Review on the Mechanical Testing and Modeling of Brain Tissue," Arch. Comput. Methods Eng., 27(4), pp. 1187–1230.
[11] Rashid, B., Destrade, M., and Gilchrist, M. D., 2013, "Mechanical Characterization of Brain Tissue in Simple Shear at Dynamic Strain Rates," J. Mech. Behav. Biomed. Mater., 28, pp. 71–85.
[12] Donnelly, B. R., and Medige, J., 1997, "Shear Properties of Human Brain Tissue," ASME J. Biomech. Eng., 119(4), pp. 423–432.
[13] Estes, M. S., and McElhaney, J. H., 1970, "Response of Brain Tissue to Compressive Loading," ASME Paper No. 70-BHF-13.
[14] Panzer, M. B., Myers, B. S., Capehart, B. P., and Bass, C. R., 2012, "Development of a Finite Element Model for Blast Brain Injury and the Effects of CSF Cavitation," Ann. Biomed. Eng., 40(7), pp. 1530–1544.
[15] Subramaniam, D. R., Unnikrishnan, G., Sundaramurthy, A., Rubio, J. E., Kote, V. B., and Reifman, J., 2021, "Cerebral Vasculature Influences Blast-Induced Biomechanical Responses of Human Brain Tissue," Front. Bioeng. Biotechnol., 9, p. 744808.
[16] Zhang, L., Makwana, R., and Sharma, S., 2013, "Brain Response to Primary Blast Wave Using Validated Finite Element Models of Human Head and Advanced Combat Helmet," Front. Neurol., 4, p. 88.
[17] Singh, D., Cronin, D. S., and Haladuick, T. N., 2014, "Head and Brain Response to Blast Using Sagittal and Transverse Finite Element Models," Int. J. Numer. Method Biomed. Eng., 30(4), pp. 470–489.
[18] Wu, T., Hajiaghamemar, M., Giudice, J. S., Alshareef, A., Margulies, S. S., and Panzer, M. B., 2021, "Evaluation of Tissue-Level Brain Injury Metrics Using Species-Specific Simulations," J. Neurotrauma, 38(13), pp. 1879–1888.
[19] Budday, S., Sommer, G., Birkl, C., Langkammer, C., Haybaeck, J., Kohnert, J., Bauer, M., Paulsen, F., Steinmann, P., Kuhl, E., and Holzapfel, G. A., 2017, "Mechanical Characterization of Human Brain Tissue," Acta Biomater., 48, pp. 319–340.
[20] Coats, B., and Margulies, S. S., 2006, "Material Properties of Porcine Parietal Cortex," J. Biomech., 39(13), pp. 2521–2525.
[21] Jin, X., Zhu, F., Mao, H., Shen, M., and Yang, K. H., 2013, "A Comprehensive Experimental Study on Material Properties of Human Brain Tissue," J. Biomech., 46(16), pp. 2795–2801.
[22] Prange, M. T., and Margulies, S. S., 2002, "Regional, Directional, and Age-Dependent Properties of the Brain Undergoing Large Deformation," ASME J. Biomech. Eng., 124(2), pp. 244–252.
[23] Li, Z., Ji, C., Li, D., Luo, R., Wang, G., and Jiang, J., 2020, "A Comprehensive Study on the Mechanical Properties of Different Regions of 8-Week-Old Pediatric Porcine Brain Under Tension, Shear, and Compression at Various Strain Rates," J. Biomech., 98, p. 109380.
[24] Begonia, M. T., Prabhu, R., Liao, J., Horstemeyer, M. F., and Williams, L. N., 2010, "The Influence of Strain Rate Dependency on the Structure-Property Relations of Porcine Brain," Ann. Biomed. Eng., 38(10), pp. 3043–3057.
[25] Haslach, H. W., Leahy, L. N., Riley, P., Gullapalli, R., Xu, S., and Hsieh, A. H., Jr., 2014, "Solid-Extracellular Fluid Interaction and Damage in the Mechanical Response of Rat Brain Tissue Under Confined Compression," J. Mech. Behav. Biomed. Mater., 29, pp. 138–150.
[26] Hosseini-Farid, M., Ramzanpour, M., McLean, J., Ziejewski, M., Karami, G., 2020, "A Poro-Hyper-Viscoelastic Rate-Dependent Constitutive Modeling for the Analysis of Brain Tissues," J. Mech. Behav. Biomed. Mater., 102, p. 103475.
[27] Karimi, A., Rahmati, S. M., and Razaghi, R., 2017, "A Combination of Experimental Measurement, Constitutive Damage Model, and Diffusion Tensor Imaging to Characterize the Mechanical Properties of the Human Brain," Comput. Methods Biomech. Biomed. Eng., 20(12), pp. 1350–1363.
[28] Laksari, K., Shafieian, M., and Darvish, K., 2012, "Constitutive Model for Brain Tissue Under Finite Compression," J. Biomech., 45(4), pp. 642–646.
[29] Libertiaux, V., Pascon, F., and Cescotto, S., 2011, "Experimental Verification of Brain Tissue Incompressibility Using Digital Image Correlation," J. Mech. Behav. Biomed. Mater., 4(7), pp. 1177–1185.
[30] Prevost, T. P., Balakrishnan, A., Suresh, S., and Socrate, S., 2011, "Biomechanics of Brain Tissue," Acta Biomater., 7(1), pp. 83–95.
[31] Rashid, B., Destrade, M., and Gilchrist, M. D., 2012, "Temperature Effects on Brain Tissue in Compression," J. Mech. Behav. Biomed. Mater., 14, pp. 113–118.
[32] Goldsmith, W., 2001, "The State of Head Injury Biomechanics: Past, Present, and Future: Part 1," Crit. Rev. Biomed. Eng., 29(5-6), pp. 441–600.
[33] Arbogast, K. B., and Margulies, S. S., 1998, "Material Characterization of the Brainstem From Oscillatory Shear Tests," J. Biomech., 31(9), pp. 801–807.
[34] Chatelin, S., Deck, C., and Willinger, R., 2013, "An Anisotropic Viscous Hyperelastic Constitutive Law for Brain Material Finite-Element Modeling," J. Biorheology, 27(1-2), pp. 26–37.
[35] Haslach, H. W., Jr., Gipple, J. M., and Leahy, L. N., 2017, "Influence of High Deformation Rate, Brain Region, Transverse Compression, and Specimen Size on Rat Brain Shear Stress Morphology and Magnitude," J. Mech. Behav. Biomed. Mater., 68, pp. 88–102.
[36] Zhang, J., Green, M. A., Sinkus, R., and Bilston, L. E., 2011, "Viscoelastic Properties of Human Cerebellum Using Magnetic Resonance Elastography," J. Biomech., 44(10), pp. 1909–1913.
[37] MacManus, D. B., Pierrat, B., Murphy, J. G., and Gilchrist, M. D., 2017, "Region and Species Dependent Mechanical Properties of Adolescent and Young Adult Brain Tissue," Sci. Rep., 7(1), p. 13729.
[38] Lujan, T. J., Underwood, C. J., Jacobs, N. T., and Weiss, J. A., 2009, "Contribution of Glycosaminoglycans to Viscoelastic Tensile Behavior of Human Ligament," J. Appl. Physiol., 106(2), pp. 423–431.
[39] Hrapko, M., van Dommelen, J. A. W., Peters, G. W. M., and Wismans, J. S. H. M., 2008, "The Influence of Test Conditions on Characterization of the Mechanical Properties of Brain Tissue," ASME J. Biomech. Eng., 130(3), p. 031003.
[40] Gefen, A., and Margulies, S. S., 2004, "Are In Vivo and in Situ Brain Tissues Mechanically Similar?," J. Biomech., 37(9), pp. 1339–1352.
[41] Kaster, T., Sack, I., and Samani, A., 2011, "Measurement of the Hyperelastic Properties of Ex Vivo Brain Tissue Slices," J. Biomech., 44(6), pp. 1158–1163.

[42] Lippert, S. A., Rang, E. M., and Grimm, M. J., 2004, "The High Frequency Properties of Brain Tissue," Biorheology, 41(6), pp. 681–691.
[43] Miller, K., Chinzei, K., Orssengo, G., and Bednarz, P., 2000, "Mechanical Properties of Brain Tissue in-Vivo: Experiment and Computer Simulation," J. Biomech., 33(11), pp. 1369–1376.
[44] Pervin, F., and Chen, W. W., 2009, "Dynamic Mechanical Response of Bovine Gray Matter and White Matter Brain Tissues Under Compression," J. Biomech., 42(6), pp. 731–735.
[45] Rashid, B., Destrade, M., and Gilchrist, M. D., 2012, "Mechanical Characterization of Brain Tissue in Compression at Dynamic Strain Rates," J. Mech. Behav. Biomed. Mater., 10, pp. 23–38.
[46] Rashid, B., Destrade, M., and Gilchrist, M. D., 2014, "Mechanical Characterization of Brain Tissue in Tension at Dynamic Strain Rates," J. Mech. Behav. Biomed. Mater., 33, pp. 43–54.
[47] Tamura, A., Hayashi, S., Watanabe, I., Nagayama, K., and Matsumoto, T., 2007, "Mechanical Characterization of Brain Tissue in High-Rate Compression," J. Biomech. Sci. Eng., 2(3), pp. 115–126.
[48] Weickenmeier, J., de Rooij, R., Budday, S., Ovaert, T. C., and Kuhl, E., 2017, "The Mechanical Importance of Myelination in the Central Nervous System," J. Mech. Behav. Biomed. Mater, 76, pp. 119–124.
[49] Zhang, J., Yoganandan, N., Pintar, F. A., Guan, Y., Shender, B., Paskoff, G., and Laud, P., 2011, "Effects of Tissue Preservation Temperature on High Strain-Rate Material Properties of Brain," J. Biomech., 44(3), pp. 391–396.
[50] Bell, E. D., Converse, M., Mao, H., Unnikrishnan, G., Reifman, J., and Monson, K. L., 2018, "Material Properties of Rat Middle Cerebral Arteries at High Strain Rates," ASME J. Biomech. Eng., 140(7), p. 071004.
[51] Ogden, R. W., 1972, "Large Deformation Isotropic Elasticity – on the Correlation of Theory and Experiment for Incompressible Rubberlike Solids," Proc. R. Soc. London, 326(1567), pp. 565–584.
[52] Rivlin, R. S., and Saunders, D. W., 1951, "Large Elastic Deformations of Isotropic Materials VII. Experiments on the Deformation of Rubber," Philos. Trans. R. Soc. London, 243(865), pp. 251–288.
[53] D'Errico, J., 2022, "Fminsearchbnd, Fminsearchcon," accessed Sept. 15, 2021, https://www.mathworks.com/matlabcentral/fileexchange/8277-fminsearchbnd-fminsearchcon
[54] Puso, M. A., and Weiss, J. A., 1998, "Finite Element Implementation of Anisotropic Quasi-Linear Viscoelasticity Using a Discrete Spectrum Approximation," ASME J. Biomech. Eng., 120(1), pp. 62–70.
[55] Fung, Y. C., 1993, *Biomechanics: Mechanical Properties of Living Tissues*, 2nd ed., Springer, New York.
[56] Chatelin, S., Vappou, J., Roth, S., Raul, J. S., and Willinger, R., 2012, "Towards Child Versus Adult Brain Mechanical Properties," J. Mech. Behav. Biomed. Mater., 6, pp. 166–173.
[57] Pearson, N., Boiczyk, G. M., Kote, V. B., Sundaramurthy, A., Subramaniam, D. R., Rubio, J. E., Unnikrishnan, G., Reifman, J., and Monson, K., 2022, "A Strain Rate-Dependent Constitutive Model for Göttingen Minipig Cerebral Arteries," ASME J. Biomech. Eng., 144(8), p. 081007.
[58] Mihai, L. A., Budday, S., Holzapfel, G. A., Kuhl, E., and Goriely, A., 2017, "A Family of Hyperelastic Models for Human Brain Tissue," J. Mech. Phys. Solids, 106, pp. 60–79.
[59] Haslach, H. W., Jr., Leahy, L. N., and Hsieh, A. H., 2015, "Transient Solid-Fluid Interactions in Rat Brain Tissue Under Combined Translational Shear and Fixed Compression," J. Mech. Behav. Biomed Mater., 48, pp. 12–27.
[60] Budday, S., Sommer, G., Holzapfel, G. A., Steinmann, P., and Kuhl, E., 2017, "Viscoelastic Parameter Identification of Human Brain Tissue," J. Mech. Behav. Biomed Mater., 74, pp. 463–476.
[61] Moran, R., Smith, J. H., and Garcia, J. J., 2014, "Fitted Hyperelastic Parameters for Human Brain Tissue From Reported Tension, Compression, and Shear Tests," J. Biomech., 47(15), pp. 3762–3766.
[62] Singh, D., Boakye-Yiadom, S., and Cronin, D. S., 2019, "Comparison of Porcine Brain Mechanical Properties to Potential Tissue Simulant Materials in Quasi-Static and Sinusoidal Compression," J. Biomech., 92, pp. 84–91.
[63] Li, Z., Yang, H., Wang, G., Han, X., and Zhang, S., 2019, "Compressive Properties and Constitutive Modeling of Different Regions of 8-Week-Old Pediatric Porcine Brain Under Large Strain and Wide Strain Rates," J. Mech. Behav. Biomed. Mater., 89, pp. 122–131.
[64] Darvish, K. K., and Crandall, J. R., 2001, "Nonlinear Viscoelastic Effects in Oscillatory Shear Deformation of Brain Tissue," Med. Eng. Phys., 23(9), pp. 633–645.
[65] de Rooij, R., and Kuhl, E., 2016, "Constitutive Modeling of Brain Tissue: Current Perspectives," ASME Appl. Mech. Rev., 68(1), p. 010801.
[66] Holmes, M. H., and Mow, V. C., 1990, "The Nonlinear Characteristics of Soft Gels and Hydrated Connective Tissues in Ultrafiltration," J. Biomech., 23(11), pp. 1145–1156.
[67] Wu, T., Alshareef, A., Giudice, J. S., and Panzer, M. B., 2019, "Explicit Modeling of White Matter Axonal Fiber Tracts in a Finite Element Brain Model," Ann. Biomed. Eng., 47(9), pp. 1908–1922.
[68] Budday, S., Sommer, G., Haybaeck, J., Steinmann, P., Holzapfel, G. A., and Kuhl, E., 2017, "Rheological Characterization of Human Brain Tissue," Acta Biomater., 60, pp. 315–329.
[69] Budday, S., Nay, R., de Rooij, R., Steinmann, P., Wyrobek, T., Ovaert, T. C., and Kuhl, E., 2015, "Mechanical Properties of Gray and White Matter Brain Tissue by Indentation," J. Mech. Behav. Biomed. Mater., 46, pp. 318–330.
[70] Christ, A. F., Franze, K., Gautier, H., Moshayedi, P., Fawcett, J., Franklin, R. J., Karadottir, R. T., and Guck, J., 2010, "Mechanical Difference Between White and Gray Matter in the Rat Cerebellum Measured by Scanning Force Microscopy," J. Biomech., 43(15), pp. 2986–2992.
[71] Felfelian, A. M., Baradaran Najar, A., Jafari Nedoushan, R., and Salehi, H., 2019, "Determining Constitutive Behavior of the Brain Tissue Using Digital Image Correlation and Finite Element Modeling," Biomech. Model Mechanobiol., 18(6), pp. 1927–1945.
[72] Moerman, K. M., Holt, C. A., Evans, S. L., and Simms, C. K., 2009, "Digital Image Correlation and Finite Element Modelling as a Method to Determine Mechanical Properties of Human Soft Tissue In Vivo," J. Biomech., 42(8), pp. 1150–1153.
[73] Maghsoudi-Ganjeh, M., Mariano, C. A., Sattari, S., Arora, H., and Eskandari, M., 2021, "Developing a Lung Model in the Age of COVID-19: A Digital Image Correlation and Inverse Finite Element Analysis Framework," Front. Bioeng. Biotechnol., 9, p. 684778.
[74] Feng, Y., Okamoto, R. J., Namani, R., Genin, G. M., and Bayly, P. V., 2013, "Measurements of Mechanical Anisotropy in Brain Tissue and Implications for Transversely Isotropic Material Models of White Matter," J. Mech. Behav. Biomed. Mater., 23, pp. 117–132.
[75] Nicolle, S., Lounis, M., and Willinger, R., 2004, "Shear Properties of Brain Tissue Over a Frequency Range Relevant for Automotive Impact Situations: New Experimental Results," Stapp Car Crash J., 48, pp. 239–258.
[76] Nicolle, S., Lounis, M., Willinger, R., Palierne, J-F., 2005, "Shear Linear Behavior of Brain Tissue Over a Large Frequency Range," Biorheology, 42(3), pp. 209–223.
[77] Smith, D. H., and Meaney, D. F., 2000, "Axonal Damage in Traumatic Brain Injury," Neuroscientist, 6(6), pp. 483–495.

CHAPTER 4

REGION SPECIFIC ANISOTROPY AND RATE DEPENDENCE OF GÖTTINGEN MINIPIG BRAIN TISSUE

4.1 Abstract

Traumatic brain injury is a major cause of injury in civilian as well as military populations. Computational simulations of injurious events are an important tool to understanding the biomechanics of injury and evaluating injury criteria and safety measures. However, these computational models are highly dependent on the material parameters used for the tissues represented in them. Reported material properties of tissue from the cerebrum and cerebellum remain poorly defined at high rates and with respect to anisotropy. In this work, brain tissue from the cerebrum and cerebellum of male Göttingen minipigs was tested in one of three directions relative to axon fibers in oscillatory simple shear over a large range of strain rates from 0.025 to 250 s^{-1}. Brain tissue showed significant direction dependence in both regions, each with a single preferred loading direction. The tissue also showed strong rate dependence over the full range of rates considered. Transversely isotropic hyper-viscoelastic constitutive models were fit to experimental data using dynamic inverse finite element models to account for wave propagation observed at high strain rates. The fit constitutive models predicted the response in all directions well at rates below 100 s^{-1}, after which they adequately predict

the initial two loading cycles, with the exception of the 250 s^{-1} rate where models perform poorly. These constitutive models can be readily implemented in finite element packages and are suitable for simulation of both conventional and blast injury in porcine, especially Göttingen minipig, models.

4.2 Introduction

Traumatic brain injury (TBI) is a significant cause of injury and death in both civilian and military populations. In the United States alone, TBI accounts for approximately 2 million emergency department visits and over 50,000 deaths per year [1], and over 18% of US service members deployed to Iraq or Afghanistan between 2001 and 2007 sustained at least a mild TBI [2]. Finite element (FE) simulations are a vital tool for understanding the biomechanics of head injury [3, 4]. The results of these models are highly dependent on the material parameters used [5]. For simulations to be accurate, their material parameters should be calculated based on the modeled loading rates and modes. The need for high-quality constitutive models is especially critical for the brain where, despite decades of experimental modeling, reported properties still show a wide range of variation [6].

Previous work by our group focused on characterizing brain tissue from adolescent Göttingen minipigs in high-rate and quasi-static shear and compression [7]. While we produced hyper-viscoelastic constitutive models that predict the response of brain tissue in shear and compression at strain rates up to 300 s^{-1}, our experimental data did not include intermediate strain rates. This work also suggested that our simple shear experiments may have been confounded by inhomogeneous deformations in part due to

wave propagation at high rates. If this is the case, conventional methods of fitting constitutive models may provide poor fit quality and not accurately reflect the experimental results. Such issues may be unavoidable in high-rate brain tissue testing, but inverse FE modeling can be used to account for dynamic effects. Recently, multiple authors have used inverse methods to successfully fit hyperelastic [8-11], as well as hyper-viscoelastic [12, 13] and biphasic [14], constitutive models to experimental tests of brain tissue. However, no author has used these methods to model simple shear in brain tissue at high rates. The literature either focuses on compressive loading or only considers simple shear using rate-independent hyperelastic models.

Peak strain rates seen in finite element models of TBI can vary by several orders of magnitude depending on the type of injury being simulated (e.g., blast vs. impact), species, and material models used in the simulation. For example, in simulations of human blast injury, strain rates have been observed on the order of ten [15, 16] to several hundred per second [17]. In contrast, peak strain rates in simulations of impact injury have been observed at up to 235 s^{-1} in porcine models compared to 65 s^{-1} in humans [18]. Consequently, constitutive models should be generated from experimental data over a broad range of strain rates.

Oscillatory shear testing, either with a parallel plate shear tester or a rheometer, is a long-established means of testing brain tissue. Most of these studies have been limited to either strain rates below 50 s^{-1} [19-25] or low strain amplitudes (below 5% shear strain) [19-24, 26], with few authors examining both high strain rates and large deformations. Darvish and Crandall [27] subjected bovine cerebral tissue to oscillations at frequencies of 1-1000 Hz at amplitudes of up to 10.5% shear strain but, due to the

effects of resonance in their experimental system, were not able to use any rates above 30 Hz to develop constitutive models. Arbogast and Margulies [28] subjected porcine brainstem samples to frequency sweeps between 20 and 200 Hz at amplitudes of up to 7.5%, while Thibault and Margulies [29] subjected porcine cerebral tissue to frequency sweeps between 20 and 200 Hz at amplitudes up to 5%. However, both studies modeled the tissue response using linear viscoelasticity and did not attempt to fit data to a hyper-viscoelastic framework. To date, no author has performed oscillatory shear experiments at both high strains (over 10%) and high strain rates (up to 200 s^{-1}) as the basis of a hyper-viscoelastic model.

Brain tissue is broadly classified as either white or gray matter. Gray matter primarily comprises neuronal cell bodies and glial cells, while white matter contains axons that connect neurons and glial support cells. Most of these axons, especially those of larger diameter [30], are wrapped in myelin sheaths. In addition to their critical physiological functions, myelin content is correlated with increased tissue stiffness [31], suggesting that they may act as reinforcing fibers within the brain. In many regions of the brain, such as corpus callosum [32] and corona radiata [33], these fibers run in a predominant direction and may lead to a significant degree of anisotropy. Many authors have examined anisotropy in the brain. Arbogast and Margulies demonstrated that the brainstem is transversely isotropic in shear with a single preferred fiber direction [28]. In the cerebrum, published data on anisotropy is mixed, with some authors reporting that the region demonstrates significant anisotropy [24, 27, 34] while others report an isotropic response [33, 35]. To date, no studies have examined the effects of anisotropy in cerebellar tissue.

In this study, we subjected tissue from the cerebrum and cerebellum of juvenile male Göttingen minipigs to simple shear frequency sweeps at rates between 0.025 and 250 s^{-1} over large sub-failure deformations. Tissue from each region was tested in one of three different directions and was used to define a transversely isotropic hyper-viscoelastic constitutive model for each region using inverse FE methods.

4.3 Methods

4.3.1 Overview

Brain tissue samples from the cerebrum and cerebellum were removed from freshly euthanized Göttingen minipigs and tested in one of three directions relative to tractography-determined axonal fiber directions. Average experimental data was used to fit hyperviscoelastic constitutive models as well as to develop transversely isotropic hyperviscoelastic constitutive models which were fit using inverse finite element methods. Average experimental data was initially fit to constitutive models assuming a homogeneous deformation and then further used to fit dynamic inverse finite FE models which accounted for non-homogeneous deformations.

4.3.2 Sample Preparation

The Animal Care and Use Review Office of the US Army Medical Research and Development Command, Fort Detrick, MD, and the Institutional Animal Care and Use Committee at the University of Utah approved all experimental protocols. Tissue was harvested from 20 juvenile male Göttingen minipigs (4-5 months old). Pigs were euthanized immediately before tissue harvest via an overdose of phenytoin/pentobarbital.

The braincase was carefully opened with a hammer and chisel, and the brain was freed from the dura and cranial nerves before being removed intact and immersed in a solution of 7.5% polyethylene glycol buffered (PEG) saline (7.5% by weight polyethylene glycol in phosphate-buffered saline) [36] until testing. To prevent potential material property changes due to differing temperatures from confounding our results, all tissue was stored and tested at room temperature (21 °C).

Diffusion tensor imaging was obtained from one animal to define brain tractography. The excised brain was imaged by Preclinical Imaging Core Facility, University of Utah on 7 T MRI (Bruker BioSpec, Ettlingen, Germany). Resulting diffusion tensor imaging (DTI) and T2 MRI data were evaluated in DSI Studio [37] to determine fiber directions and identify suitable sites for tissue harvest in the cerebrum and the cerebellum. In the cerebrum, a region of the corona radiata with fibers running predominantly rostral-caudally was chosen (Figure 4.1), while in the cerebellum a region with fibers running predominantly medial-laterally was chosen (Figure 4.2). All tissue samples used for mechanical characterization were harvested from these regions in one of three directions based on predominant fiber orientation (Figure 4.3). Tissue was tested in either the A direction, where the fibers run in the shear plane and parallel to the direction of shear; the B direction, where the fibers run in the shear plane and normal to the direction of shear; or the C direction, where fibers run normal to both the shear plane and the direction of shear [28].

Immediately before testing, tissue was cut, using a custom die, to a cuboid with a size of 8 mm wide by 8 mm long and 5 mm thick in one of the three fiber orientations. A scalpel was run over the top face of the die to ensure a uniform thickness of the specimen

and remove any excess brain tissue. A total of 2-4 samples were harvested from the cerebrum and cerebellum of each animal for a target sample size of 12 per group (region and direction). After cutting, tissue samples were measured with digital calipers, and dimensions were recorded. Tissue samples were then immediately mounted between parallel aluminum plates on a custom oscillatory shear tester with a thin layer of cyanoacrylate adhesive. Due to the high driven strain rates used in these tests, tissue could not be tested in a bath. Tissue samples were instead inspected between each applied frequency, and additional PEG buffered saline was applied as needed if the tissue appeared to be drying out.

4.3.3 Tissue Tester

All material characterization was performed on a custom oscillatory shear testing device (Figure 4.4). The top plate was connected to a 250g load cell (Model 31 Low, Honeywell, Golden Valley, MN), while the bottom plate was connected to a voice coil actuator (LAS16-23, BEI Kimco, Vista, CA) controlled via a servo amplifier and driver (412CE, Copley Controls, Canton, MA). Load and displacement data were acquired from the load cell and an integrated Hall effect sensor in the voice coil, respectively, via a data acquisition unit (SCXI-1520, National Instruments, Austin, TX) using a custom LABVIEW VI.

4.3.4 Oscillation Tests

Each sample was subjected to a frequency sweep corresponding to five cycles with a shear strain amplitude of 20% at rates of 0.025. 0.25, 2.5, 12.5, 50, 100, 125, and

250 s^{-1} (driven frequencies of 0.02, 0.2, 2, 10, 40, 80, 100, and 200 Hz) around a mean shear strain of 0%. Data were simultaneously sampled from the load cell and displacement sensor with a sample rate set at 100 times the driven frequency (between 2 and 20 kHz) such that there were 500 data points for every oscillation.

4.3.5 Data Processing

Load and displacement time series data were first processed to remove any errant signal noise by passing it through a phaseless four-pole Butterworth filter specified in the SAE J211 standard [38] with a cutoff frequency of ten times the driven frequency. The 1st Piola-Kirchoff (1st PK) shear stress (T) was then calculated by dividing the load signal by the cross-sectional sample area (the product of tissue length and width). Shear strain (K) was defined as the ratio of displacement to specimen height.

Dynamic modulus was calculated at each driven strain rate by first algorithmically identifying the locations of the peaks and troughs in the oscillatory stress and strain data using the *findpeaks* function in MATLAB. The locations of these peaks and troughs were then used to calculate the amplitudes of the first cycles of the stress and strain waveforms, T_0 and K_0, respectively. These amplitudes were used to calculate the dynamic modulus using Eq 4.1. Finally, the phase angle (ϕ) was calculated using the cross-correlation function *xcorr* in MATLAB.

$$G = T_0/K_0 \qquad \text{Eq 4.1}$$

For each region and direction, we calculated the average shear stress and shear strain waveforms by first interpolating the stress and strain data from each individual sample such that each sample had values at the same discrete time points. We then

computed the average and standard deviation of the interpolated stress and strain waveforms which were used for all subsequent analysis.

4.3.6 Statistical Analysis

To determine whether region-specific or anisotropic constitutive models were needed, the effects of tissue anisotropy and tissue region were examined by comparing the dynamic moduli across all strain rates. First, a multivariate ANOVA was performed to compare the effects of region and direction on dynamic modulus. Where a statistical difference ($p < 0.05$) was detected, a Tukey Test was performed to evaluate pairwise differences in either region, tissue direction, or the combination of region and direction.

4.3.7 Constitutive Modeling

As a first step, average data from the cerebrum and cerebellum in a non-preferred (transverse-transverse) direction were used to fit a hyper-viscoelastic constitutive model [39] by optimizing an objective function in MATLAB, where the experimental deformation was assumed to be homogeneous. The 2nd Piola-Kirchoff stress ($\boldsymbol{S}$) was given by Eq 4.2,

$$\boldsymbol{S}(t) = \int_0^t G(t-s)\frac{\partial \boldsymbol{S}^e}{\partial s}\,ds \qquad \text{Eq 4.2}$$

where $\boldsymbol{S}^e$ is the elastic stress, and the reduced relaxation function $G(t)$ is given by a five-term Prony series (Eq 4.3),

$$G(t) = 1 + \sum_{i=1}^{5} g_i \exp\left(\frac{-t}{\tau_i}\right) \qquad \text{Eq 4.3}$$

where g_1 - g_5 are viscoelastic parameters, and τ_1 - τ_5 are defined such that values vary by one decade from $\tau_1 = 1\ s$ to $\tau_5 = 10^{-4}\ s$. For the elastic stress, we used a one-term Ogden model (Eq 4.4).

$$W = \frac{c}{m^2}(\lambda_1^m + \lambda_2^m + \lambda_3^m - 3) \quad \text{Eq 4.4}$$

The parameters c and m are the shear stiffness and a non-linearity parameter, respectively, while λ_i is the ith eigenvalue of the right Cauchy-Green stretch tensor. For this fitting, we assumed a homogeneous, simple shear deformation throughout the tissue (Eq 4.5),

$$\boldsymbol{F} = \begin{bmatrix} 1 & K & 0 \\ 0 & 1 & 0 \\ 0 & 0 & 1 \end{bmatrix} \quad \text{Eq 4.5}$$

where *K* is the shear strain calculated from the experimental displacement data (displacement divided by sample height).

The parameters c, m, and g_1 - g_5 were fit in MATLAB using the function *fminsearchbnd* [40] to optimize the objective function in Eq 4.6. Prior to fitting, experimental 1st PK stress was converted to 2nd PK stress.

$$\chi = \frac{1}{n_{samp}} \sum_{i=1}^{n_{samp}} \frac{\left(P_i^{Experimental} - P_i^{Model}\right)^2}{\max(P^{Experimental})} \quad \text{Eq 4.6}$$

4.3.8 Finite Element Modeling

To investigate constitutive model performance in the absence of assumptions about deformation homogeneity, FE models were constructed in FEBio for each of the three directions in the cerebrum and cerebellum (6 FE models total). All models consisted of a half symmetry 8 mm long by 4 mm wide and 5 mm tall cuboid of brain (Figure 4.5)

with symmetry boundary conditions (constrained Y) applied to the positive Y face. The top face of the brain model was connected to a fixed 1 mm thick rigid plate via a rigid contact to mimic the experimental conditions of the brain tissue connected to the load-cell-side plate in our shear tester. We did not explicitly model the bottom, moving platen in this simulation. Instead, the bottom face of the brain tissue was constrained in the Y and Z directions, and a sinusoidal X displacement was generated from the average strain vs. time data for each region applied.

Brain tissue was modeled as an uncoupled viscoelastic material with an uncoupled solid mixture chosen for the elastic material type. The uncoupled solid mixture, representing the matrix component, was defined using an uncoupled Ogden model. As preliminary simulations showed the deformation was substantially inhomogeneous, with both tensile and shear stresses contributing to the X-direction reaction force, we opted to use a fiber with exponential-power law material in FEBio [41] with the deviatoric fiber stress given by Eq 4.7,

$$\tilde{\boldsymbol{\sigma}} = H(\tilde{I_n} - 1)\frac{2\tilde{I_n}}{J}\frac{\partial\tilde{\psi}}{\partial\tilde{I_n}}\boldsymbol{n}\otimes\boldsymbol{n} \qquad \text{Eq 4.7}$$

where $H(x)$ is the Heaviside step function enforcing the fibers only contributing in tension, $\tilde{I_n}$ is the invariant defined by the square of the deviatoric fiber stretch $\tilde{\lambda}$ (Eq 4.8),

$$\tilde{I_n} = \tilde{\lambda}^2 = \boldsymbol{n_r}\cdot\tilde{\boldsymbol{C}}\cdot\boldsymbol{n_r} \qquad \text{Eq 4.8}$$

where $\tilde{\boldsymbol{C}}$ is the deviatoric right Cauchy-Green tensor, and the unit vector along the fiber in the reference configuration $\boldsymbol{n_r}$ is related to the unit vector along the fiber in the current configuration $\boldsymbol{n}$ (Eq 4.9).

$$\boldsymbol{n} = \tilde{\boldsymbol{F}}\cdot\boldsymbol{n}_r/\tilde{\lambda} \qquad \text{Eq 4.9}$$

The strain energy function for this fiber can then be given by Eq 4.10,

$$\tilde{\psi} = \frac{\xi}{\alpha\beta}\left(exp\left[\alpha\left(\tilde{I_n} - 1\right)^{\beta}\right] - 1\right) \qquad \text{Eq 4.10}$$

where $\xi > 0$ is the fiber modulus, $\alpha \geq 0$ is the coefficient of the exponential argument, and $\beta \geq 2$ is the power of the exponential argument.

A convergence study was performed to examine the optimal element type and number of elements by comparing the time value and magnitude of the first peak X reaction force in the model. The optimal models were meshed with 400 HEX8 elements, with eight elements in the X direction, two in the Y direction, and 25 in the Z direction.

Optimization of all matrix and viscoelastic parameters was performed in the non-preferred A direction for each region, keeping the other non-preferred (C) direction to be used for validation. Optimal material parameters for the constitutive models were found using the built-in FEBio optimization functionality. To reduce computational time, we leveraged the convolution integral present in the hyper-viscoelastic constitutive model to optimize parameters at the strain rates closest to the corresponding time constant and all rates preceding that rate. Thus, the hyperelastic parameters (c, m) were optimized for the quasi-static oscillations of 0.025 s^{-1}, g_1 was optimized for all oscillations through 0.25 s^{-1}, g_2 was optimized for all oscillations through 12.5 s^{-1}, g_3 was optimized for all oscillations through 125 s^{-1}, and $g_4 - g_5$ were optimized for all oscillations up through 250 s^{-1}. Optimization of the three fiber-specific parameters (ξ, α, β) was performed on all oscillations at 0.025 s^{-1} for each region's preferred (B) direction, leaving all subsequent rates to be used for validation. In order to reduce the likelihood that the solution was settling on a local minimum, multiple parameter scans were run for each optimization. Initially, a large range of values was scanned with a large step size. Subsequent scans were then performed with a progressively narrowing range and decreasing step size until

a scan with a step size of 10 (c, ξ) or 1 (m, α, β, g_i) was performed. An optimization was then run using the scanned value with the lowest objective value from this final scan.

4.4 Results

4.4.1 Experimental Observations

Due to early issues in data acquisition triggering and testing errors resulting in poorly adhered or otherwise deficient samples, the total sample size in all groups differed slightly from the 12 samples targeted. In the cerebrum, the sample size for each direction was A = 12, B = 10, and C = 11, while in the cerebellum, the sample size for each direction was A = 10, B =12, and C = 12.

Average stress-strain (hysteresis) curves for the cerebrum in the A-C directions are shown in Figures 4.6-4.8, respectively, while hysteresis curves for the cerebellum in the A-C directions are shown in Figures 4.9-4.11, respectively. The stress-shear curves show substantial degrees of hysteresis for all rates, regions, and directions tested, with the brain being significantly stiffer in loading vs. unloading. Comparisons between the first and last loading cycles showed that the first cycle is stiffer than the last for all but the highest rates. For all regions and directions, the first applied oscillation of 0.025 s^{-1} shows the most dramatic change between the first and last cycle, likely due to preconditioning of the sample.

In tests with strain rates below 100 s^{-1}, prescribed displacement waveforms showed minimal variation from the target amplitude of K = 0.2 for five cycles at a given driven frequency. At rates of 100 to 250 s^{-1}, drift was present in the displacement

waveform, with subsequent loading cycles applying higher amplitudes. However, this was consistent between tests, and peak deformation stayed below K = 0.25.

Measured stress waveforms showed greater variability, especially at high rates. Additionally, some degree of load cell drift is apparent at the lowest rate of 0.025 s^{-1}, which is not evident at higher rates. For oscillations at and above 50 s^{-1}, the amount of noise in the stress data increases significantly. This is particularly evident in the 100 and 125 s^{-1} rates, where the hysteresis curves appear to cross over each other at several points. At 250 s^{-1}, the curve shifts from advancing from the bottom left quadrant to the bottom right quadrant in a clockwise direction to advancing from the bottom left quadrant to the top left quadrant in a counter-clockwise direction. This phenomenon appears to be due to a change in the phase of stress and strain, with the stress curve beginning to lag the strain curve rather than precede it as at other rates. Generally, the preferred and non-preferred directions showed similar noise levels with the exception of the 50 s^{-1} where a significant spike in noise is present in the stress data for the preferred directions but is absent in the non-preferred directions.

For all groups, the dynamic modulus increased non-linearly from rates of 0.025 s^{-1} to 50 s^{-1} before decreasing slightly at 100 s^{-1}, with the means of some groups continuing to decrease while others leveled out or began to increase again (Figure 4.12). There is also a noticeable increase in scatter at the highest rates, potentially a result of increased experimental noise. Multivariate ANOVA suggested significant differences ($p < 0.01$) between loading directions for both the cerebrum and cerebellum. In the cerebrum, pairwise t-tests showed that the B direction was significantly stiffer than both the A ($p < 0.001$) and C ($p < 0.001$) directions, which did not significantly differ ($p = 0.58$).

Pairwise t-tests in the cerebellum showed that the B direction was significantly stiffer than the C direction ($p = 0.008$) but not the A direction ($p = 0.08$). As in the cerebrum, the A and C directions in the cerebellum showed no significant difference ($p = 0.76$). While no significant difference was present between the A and B directions, the mean dynamic modulus is noticeably higher at all rates in the B direction compared to the A direction, which has comparable means to the C direction. Thus, it seems most accurate to conclude that brain tissue from both the cerebrum and cerebellum shows a transversely-isotropic response, with the preferred direction being the B direction.

For all groups, the stress waveform led the strain waveform by approximately 20 degrees between 0.025 s^{-1} and 12.5 s^{-1} before increasing to around 40 degrees at a rate of 50 s^{-1} (Figure 4.13). At 100 s^{-1}, there was considerable variation in phase angle, with stress leading strain between 50 and 60 degrees in the cerebrum and 36 and 63 degrees in the cerebellum. Some individual samples showed a phase lag at this rate, where the stress waveform began to lag the strain waveform, leading to more variation in the data. At 125 s^{-1}, the mean phase angle decreased and a similarly large degree of variance to the 100 s^{-1} rate was present, with some, but not all, samples exhibit phase lag. At 250 s^{-1}, the mean phase angle for all groups ranged between -6 and -65 degrees, and almost all individual samples show some degree of phase lag. Preliminary evaluation of farm pig brain tissue and silicone gel with similar stiffnesses to brain tissue [42]cut to different heights suggests that the degree of this phase lag appears to be tied to sample height, with thicker samples showing a more pronounced degree of negative phase shift than thinner samples, suggesting wave propagation is occurring through the tissue.

4.4.2 Constitutive Modeling

4.4.2.1 Assuming a Homogeneous Deformation

Constitutive models assuming a homogeneous deformation (simulated using MATLAB) performed well at rates of 0.025 s^{-1} to 12.5 s^{-1}, showing a low degree of phase shift and relatively low RMSE values for both the cerebellum (Figure 4.14) and cerebrum (Figure 4.15) and; phase angle and root mean squared error (RMSE) values for each model at each rate shown in Table 4.1. At 50 s^{-1}, there is a noticeable increase in both error and phase shift for both regions. At the two highest rates, there is a large, negative phase shift between the model and the experimental data, indicating that the model is predicting stress values occurring substantially earlier than observed experimentally, suggesting that the assumption of a homogeneous deformation is incorrect. These models also poorly predict the general stress response at these highest rates, overpredicting the final two cycles at the 125 s^{-1} rate and substantially underpredicting stress values at the 250 s^{-1} rate.

4.4.2.2 Without Restrictions on Deformation Homogeneity

FEBio simulations for low-rate cases resulted in model fits similar to those assuming a homogeneous deformation, but substantial differences were apparent at higher rates. At the lower rates (0.025 and 12.5 s^{-1}), shear stress distributions were closely similar to one another, all showing the broadly uniform stress distribution in the center shear plane observed for 0.025 s^{-1} (Figure 4.16). However, areas of lower stress develop on the left and right sides of the model, and regions of higher stress are seen in the four corners of the model at the rigid plate and fixed boundaries. Generally, the model remains

hexahedral even at high deformations at the lower rates, though some curvature develops in the elements at the rigid contact and fixed boundaries. At 50 s^{-1}, the model exhibits a similar stress distribution to lower rates at low strains ($K < 0.1$) but develops a noticeable stress concentration in the top half of the model as strains increase. At higher strains, the model develops a slight curvature on the left and right sides, with the side facing the direction of motion becoming slightly concave. When the motion stops at the peak or minimum of the sinusoidal oscillation, the model recovers a roughly hexahedral state similar to lower rates. At the three highest rates (100-250 s^{-1}), substantial wave propagation is present in the model, with stress waves noticeably developing at the bottom, oscillating face, and advancing towards the rigid contact at the top face. The model also develops substantial curvature at these rates as the stress wave propagates through the sample. These effects become especially pronounced at 250 s^{-1}.

Visual inspection of the models shows the tendency of the inverse FE model to somewhat overpredict the magnitude of maximum and minimum stresses to varying degrees in all directions and at all rates, with the biggest degree of overprediction seen in the C direction. At 125 s^{-1}, the model tends to overpredict the magnitude of stresses after the first two oscillations and overpredicts the magnitude after the first trough at 250 s^{-1}. FE-derived stress predictions in the cerebrum for all oscillations are compared to experimental stresses in the A, B, and C directions in Figure 4.17-4.19, respectively. Phase and error values at all rates for each of these directions are shown in Table 4.2. For all directions, the lowest rate of 0.025 s^{-1} shows a relatively high degree of phase shift and error. Error and the magnitude of phase shift are substantially lower between 0.25 and 50 s^{-1}, with the highest error in the A direction. Above 50 s^{-1}, both error and phase

shift increase, with all directions showing some negative phase shift, indicating the model is leading the experimental data somewhat at these rates. At 100 and 125 s^{-1}, the MATLAB fits have a similar or lower phase angle to the inverse FE fits, while at 250 s^{-1}, the inverse FE fits have a lower phase shift.

Inverse FE fits for the cerebellum are shown in Figures 4.20-4.22 for the A, B, and C directions, respectively. Table 4.3 shows the phase angle difference and error for the cerebellar fits. Similar to the cerebrum, error, and phase angle are relatively high for all regions at 0.025 s^{-1} before decreasing for rates up to 100 s^{-1}. However, error and phase are notably higher at these rates, with a pronounced increase above 12.5 s^{-1}. At 100 s^{-1}, there is a lower degree of phase shift compared to the cerebrum though error values remain high. Visual inspection of the plots shows that the cerebellar models tend to underpredict maximum while slightly overpredicting minimum stress, especially at rates below 100 s^{-1} and in the C direction. Fits for the 100 s^{-1} and 125 s^{-1} rates are better than in the cerebrum though they degrade in quality after the second oscillation. In contrast to the cerebrum, the model poorly fits the initial loading at 250 s^{-1} before better-predicting stresses at subsequent oscillations, which is especially notable in the A and C directions. Table 4.4 shows the optimized parameters for both the cerebrum and cerebellum models. The models have similar Ogden model components, though the cerebellum model has a higher shear modulus and lower non-linearity parameter than the cerebrum model. The viscoelastic components are similar at lower rates for both models, but the cerebrum model has higher values at g_3 and g_5, suggesting increased sensitivity to high-rate loading. The cerebrum model also exhibits a much lower degree of anisotropy than the

cerebellum model, with a fiber stiffness (ξ) and an exponential coefficient (α) over five times higher in the cerebellum model compared to the cerebrum model.

Comparisons of experimental dynamic modulus with dynamic modulus calculated from the FE model for both the cerebellar and cerebral regions are shown in Figure 4.23. Dynamic modulus values for the cerebellar model are generally lower than the mean values from the experimental data, but stay within one standard deviation. In the cerebral model, dynamic moduli from the FE models show greater deviation from the mean experimental response than in the cerebellar models though still stay within one deviation at rates up to 50 s^{-1}, before being overpredicted at rates of 100 to 250 s^{-1}.

Comparisons of experimental phase angle data with phase angle values calculated from the FE model for both the cerebellar and cerebral regions are shown in Figure 4.24. In both the cerebral and cerebellar regions, the phase angle for all directions stays between 0 and 6 degrees up to 50 s^{-1} in the cerebellum and 125 s^{-1} in the cerebrum. At rates above this, phase angles from at least one loading direction show a negative phase shift up to -16 degrees compared to the largest negative phase shift of -65 degrees seen in the experimental data.

Lastly, Figure 4.25 shows the predicted shear (XZ) stress for a single ramp loading at the tested strain rates to a shear of K = 0.2 when inertial effects are not enforced in the stress expression, and a homogeneous deformation is assumed. As the anisotropic model has no effect on the shear stress given a homogeneous deformation, results are presented for the cerebrum and cerebellum. Notably, predicted cerebral stresses are markedly higher than cerebellar stresses at all rates and scale more at higher

rates. The peak stress grows from 1.3 times higher in the cerebrum than the cerebellum at 0.025 s^{-1} to 2.2 times higher at a rate of 250 s^{-1}.

4.5 Discussion

The objective of this study was to develop anisotropic hyper-viscoelastic constitutive models of Göttingen minipig cerebrum and cerebellum tissue over a large range of strain rates relevant to conventional and blast TBI. Results show that the cerebrum and cerebellum are highly rate dependent, with stiffness developing non-linearly as a function of strain rate. Additionally, results showed that tissue from the cerebrum and cerebellum is transversely-isotropic with a preferred fiber direction. Samples showed high degrees of wave propagation through the tissue at high rates, which complicated the constitutive model fitting with traditional optimization methods. However, dynamic inverse finite element modeling was able to achieve adequate constitutive model fits.

Results show that brain tissue dynamic modulus increases exponentially as a function of strain rate. While previous work from our group [7], as well as multiple other authors [26, 27, 29, 35, 43, 44], have demonstrated substantial rate dependence of brain tissue subject to simple shear (either single ramp or oscillatory loading), previous modeling of Göttingen minipig brain tissue only captured loading at QS and high rates (150 and 300 s^{-1}). It was not calibrated at intermediate rates, which may be necessary for injuries other than blast. Both Darvish and Crandall [27] and Thibault and Margulies [29] demonstrated a non-linear increase in stiffness at frequencies between 1 and 1000 Hz and 20 and 200 Hz, respectively, with no drop off as seen in our data at a frequency of 80 Hz

(100 s^{-1}), suggesting that signal noise may be affecting our results at these rates. Reported strain magnitudes at 100 Hz ranged from about 500 – 5000 Pa in the previous studies compared to around 1000-4000 in our results, though direct comparisons are difficult due to differences in species, animal age, and time between death and sample testing.

Phase angle plots show a relatively stable phase shift between the stress and strain waveforms between rates of 0.025 and 12.5 s^{-1} before the phase angle increases at 50 and 100 s^{-1}. Phase angle then decreases and becomes negative at the three highest rates as stress begins to lag strain. In a viscoelastic material subject to harmonic oscillation, stress should lead strain between 0 (purely elastic response) and 90 degrees (purely viscous response). At the two highest rates, our results show a negative phase angle, with strain leading stress, which was also demonstrated by Darvish and Crandall [27] in porcine brains. This phenomenon suggests that inertial effects are present at high rates, which need to be accounted for. Namely, there is likely a substantial degree of wave propagation between the moving bottom plate and the fixed top plate where the load was measured, as the FE models predicted. However, this was not immediately visible on test videos of high-rate tests; strains should be verified experimentally using digital image correlation (DIC) in future work.

The increase in phase angle between 12.5 s^{-1} and 100 s^{-1} suggests that the internal damping (the tangent of the phase angle) increases as a function of driven frequency. This, in turn, violates the continuous relaxation spectrum assumption underlying the Fung quasi-linear viscoelastic (QLV) model [45] used here, which states that internal damping will remain relatively constant between several decades of driven oscillatory frequencies. While the QLV models used in this work generally fit the data well, there was a

noticeable trend towards overprediction of stresses at rates of 100 s^{-1} and above, especially in subsequent loading cycles, which may suggest models with increased damping at high rates may perform better. While this effect is not seen to as large of a degree in phase angle data calculated from the FE models, this may be a result of constitutive model selection and may not be indicative of the physical response of the tissue. Future work should aim to explore constitutive models accounting for discontinuous damping, either through discrete element models [25] or a fully nonlinear viscoelastic model [27].

Both the cerebrum and cerebellum were shown to be transversely isotropic, with a single preferred direction in the B direction, where DTI-identified fibers were oriented parallel to the shear plane but transverse to the direction of shear. Regional differences became more apparent as the strain rate increased, and the cerebrum appeared to have a larger degree of anisotropy than the cerebellum. Transverse isotropy was previously observed in this orientation in the brainstem by Arbogast and Margulies [28]. Both Jin et al. [46] and Prange and Margulies [47] tested samples from a portion of the corona radiata similar to our work. They found a significant difference in stiffness in a direction they suggest has a fiber orientation similar to the A direction in this work. However, both authors assumed that fibers predominantly ran outward (laterally and superiorly) from the corona radiata instead of rostral-caudally, as the DTI we performed here shows, suggesting that the fiber orientation was closer to the B direction we found was stiffest. Conversely, both Budday et al. [33] and Nicolle et al. [35] showed no significant effect of direction. However, Budday tested tissue at QS rates where any variation between regions may be lost in natural variance. Nicolle tested tissue at either very low strains

(0.0033%) or low rates (0.8 s^{-1}), conditions where directional differences may be difficult to detect.

The finite element models presented in this work show a substantial degree of shear wave propagation from the oscillations applied to the bottom surface of the model to the measurement at the top surface. Examination of shear stress waveforms of individual elements in the finite element model suggests that it takes about 2.9 ms for the shear wave to travel the 5 mm from the bottom to the top of the cerebellum model at driven strain rates of 100, 125, and 250 s^{-1}, a wave speed of 1.7 m/s, compared to a travel time of 2.4 ms with a wave speed of 2.1 m/s in the cerebrum model. The higher wave velocity in the cerebrum may explain the lower degree of phase shift seen in the MATLAB fit-constitutive models between the cerebrum and cerebellum. Note that the phase shift discussed in MATLAB and inverse model fits is not the same as the phase angle calculated along with the dynamic modulus, and is presented to quantify fit quality in addition to error. Jian et al. [48] measured acoustic shear wave speeds in porcine brain tissue exposed to ultrasonic radiation and reported shear wave speeds between 1.5 to 2 m/s, while Hamhaber et al. [49] reported a mean velocity of 1.88 ± 0.58 m/s in elastography experiments on human brain tissue subject to mechanical excitation of about 80 Hz (the driven frequency for the 100 s^{-1} tests reported here). These results agree with the results predicted by our finite element simulations. As a result of the substantial wave propagation demonstrated here, future high-rate experiments on brain tissue should either aim to limit sample thickness to limit the travel distance for shear waves or account for it during constitutive model fitting.

Unsurprisingly, the MATLAB constitutive model fits, which did not account for inhomogeneous deformations or dynamic effects, performed poorly. While the models performed well at rates below 125 s^{-1}, they underperformed the inverse FE fit models at all rates but 0.025, 100, and 125 s^{-1} in the cerebrum and 0.025 and 12.5 s^{-1} in the cerebellum. Critically, the poorly matched parameters at a high rate could lead to an inaccurate material response when used in dynamic simulations of brain injury, possibly making the tissue appear substantially stiffer. Additionally, the fourth invariant-dependent anisotropic model implemented in the inverse FE fit models could not be implemented using the modeling framework of the MATLAB models, as the assumption of a homogeneous, simple shear deformation would have led to no shear stress due to the fibers, with fiber stress only contributing axially. Anisotropy could be added by accounting for matrix-fiber interaction terms based on higher order invariants, but that may misrepresent the anisotropic response of the tissue given that inverse FE fit models could account for the observed direction dependence using just fiber terms.

While the inverse finite element constitutive model fits performed better than the MATLAB fits, they still had substantial limitations. Inverse FE fits still show a substantial error, especially the lowest and highest rates, particularly regarding improper matching of model phase. While the phase shift is markedly improved from the MATLAB models at high rates, predicted stress waveforms still lead to experimental stress waveforms, suggesting an overprediction of wave velocity. The inverse FE fits also struggle to match amplitude through all oscillations at high rates. Future work should aim to improve these models by examining different constitutive models to address issues with damping and predicted wave amplitude.

The FE-fit models for both the cerebrum and cerebellum generally provide good prediction of experimental stresses. At rates below 100 s^{-1}, the cerebral model predicts experimental stress over all oscillations particularly well but shows overprediction of maximum stresses at 2.5 and 12.5 s^{-1} and minimum loads at 12.5 and 50 s^{-1}, with the largest degree of over-prediction in the A and C directions. At 100 s^{-1} and 125 s^{-1}, the cerebral models provide good prediction of the first cycle of loading with predictive quality degrading over successive cycles. At 250 s^{-1}, the cerebral models provide good prediction of the initial quarter of a cycle of loading, before tending to substantially overpredict the magnitude of stress at all subsequent cycles. A similar trend holds in the cerebellum, though the cerebellar models show a more substantial degree of underprediction of peak stress at rates below 100 s^{-1}. The cerebellar models perform slightly better than cerebral models at 100 and 125 s^{-1}, though still shows issues in prediction after the first two cycles. At 250 s^{-1}, the cerebellar model performs notably poorer than the cerebral model during the initial quarter of a cycle in the A and C directions but then performs better at subsequent cycles. In the B direction, there is substantial phase shift present in the first quarter cycle of loading before the phase shift reducing at subsequent rates, though peak stress magnitude is still substantially overpredicted. Evaluation of dynamic modulus values calculated from the FE models also demonstrates poorer model performance above 50 s^{-1} in the cerebellum and 100 s^{-1} in the cerebrum, with the FE model being overly stiff relative to the experimental data.

The constitutive models presented here can predict the first two cycles of loading at all rates up to 125 s^{-1} and initial ramp loading at 250 s^{-1} in multiple fiber directions for both the cerebrum and cerebellum. At 250 s^{-1}, it is expected that the initial ramp loading

could capture the initial blast overpressure wave seen in simulations of blast injury [3, 50], though could struggle predicting stresses from wave reflections.

4.5.1 Limitations

Experimentally recorded load data exhibited large degrees of variation at the QS (0.025 s^{-1}) and four highest (50 – 250 s^{-1}) rates. At the QS rate, the load data is subject to drift over the 300-sec-long test, which seems to skew the results. While attempts were made to compensate for this drift during data post-processing, substantial preconditioning effects at this rate made it difficult to isolate the drift fully. As a result, data quality at this rate is diminished compared to subsequent rates but was still sufficient to be used to fit hyperelastic and anisotropic parameters, which showed little change in fit values when additional, higher-rate data were considered. The cerebrum shows a substantially larger degree of variation for all rates than the cerebellum, especially at 50 s^{-1}. Examination of individual stress traces shows a high degree of variation between the phase and amplitude of individual stress waveforms with no clear outliers at all rates. Given this group's harvesting location and testing orientation, animal-to-animal variations in overall fiber density and orientations, as well as slight variations in die location and rotation between brains, may be responsible for this.

At high rates, substantial noise becomes evident in load data, especially at the two highest rates where load data loses its roughly sinusoidal shape, and higher frequency oscillations can be seen in the data. While some degree of higher frequency oscillation is predicted by the FE models presented here, suggesting that this could be an expected physical response of the tissue, it is also worth noting that frequency domain inspection

of high-rate tests shows spikes close to the 410 Hz ringing frequency of the load cell-side test fixtures. Thus, it seems possible that some of the variations in high-rate tests may be due to the influence of excitation of our load-cell-side test fixtures, resulting in poorer quality fitting. Future work at high rates should aim to use fixtures with higher ringing frequencies to reduce the risk of excitation.

In addition to issues with noise, the experimental data used in the creation of inverse finite element models had a few notable limitations. Tissue deformations were not mapped during experiments and only the motion of the voice-coil attached plate was simulated in the inverse finite element models. Thus, the actual degree of wave propagation and inhomogeneous deformation predicted in the model cannot be experimentally validated. Future work should aim to explicitly map sample deformations during tests using digital image correlation (DIC) to improve model quality. Inverse finite element modeling coupled with DIC deformation data has previously been used to model brainstem in compression [13] successfully and soft tissue phantoms [51], albeit at relatively low rates. Additionally, the experimental response used to fit constitutive models at all rates above the QS rate was substantially preconditioned and may not be representative of the in vivo state of the brain and may be substantially softened. Future work should aim to examine the effects of pre-conditioning at high rates.

4.6 Conclusion

The study provides the first set of experimentally validated transversely-isotropic hyper-viscoelastic constitutive models of Göttingen minipig cerebral and cerebellar tissue subjected to oscillatory shear loading over a wide range of strain rates relevant to both

impact and blast TBI. Our results demonstrate that both the cerebrum and cerebellum have a single preferred direction and can be modeled as transversely-isotropic. Additionally, results showed a large degree of wave propagation and inhomogeneous deformations at high strain rates necessitating the need of inverse finite element models to capture the response of the tissue in constitutive models. The resulting constitutive models were able to match phase and tissue response at low and high rates in multiple loading directions, but still show some degree of overprediction of stress magnitudes at high rates and a small amount of phase shift. Additional refinement of the models to damp out the response at high rates and further evaluate experimental deformations may be needed.

4.7 Acknowledgements

Funding for this study was provided by the U.S. DoD (Funder ID: 10.13039/100000005), the Defense Health Program managed by the U.S. Army Military Operational Medicine Research Program Area Directorate (Fort Detrick, MD) (Funder ID: 10.13039/100000090), the HJF was supported by the U.S. Army Medical Research and Development Command (Contract No. W81XWH-17-2-0008; Funder ID: 10.13039/100016156), and the University of Utah was partially supported by the National Science Foundation (Award No. 2027367; Funder ID: 10.13039/100000147).

The authors would also like to thank Dr. Jeffery A. Weiss and Dr. Steve A. Maas for their assistance in developing and troubleshooting the finite element models presented here.

4.8 Disclaimer

The opinions and assertions contained herein are the private views of the authors and are not to be construed as official or as reflecting the views of the U.S. Army, the U.S. Department of Defense (DoD), or The Henry M. Jackson Foundation for the Advancement of Military Medicine, Inc. (HJF). This paper has been approved for public release with unlimited distribution.

4.9 References

[1] Taylor, C.A., et al., Traumatic Brain Injury-Related Emergency Department Visits, Hospitalizations, and Deaths - United States, 2007 and 2013. *MMWR Surveill. Summ.*, 2017. **66**(9): 1-16.

[2] Tanielian, T.L., *Invisible Wounds of War : Psychological and Cognitive Injuries, Their Consequences, and Services to Assist Recovery*. 2008, Santa Monica, CA: RAND Corporation.

[3] Sundaramurthy, A., et al., A 3-D Finite-Element Minipig Model to Assess Brain Biomechanical Responses to Blast Exposure. *Front Bioeng Biotechnol*, 2021. **9**.

[4] Sundaramurthy, A., et al., Blast-Induced Biomechanical Loading of the Rat: An Experimental and Anatomically Accurate Computational Blast Injury Model. *J. Neurotrauma*, 2012. **29**(13): 2352-2364.

[5] Zhao, W., B. Choate, and S. Ji, Material Properties of the Brain in Injury-Relevant Conditions - Experiments and Computational Modeling. *J. Mech. Behav. Biomed. Mater.*, 2018. **80**: 222-234.

[6] Meaney, D.F., B. Morrison, and C. Dale Bass, The Mechanics of Traumatic Brain Injury: A Review of What We Know and What We Need to Know for Reducing Its Societal Burden. *J. Biomech. Eng.*, 2014. **136**(2).

[7] Boiczyk, G.M., et al., Rate- and Region-Dependent Mechanical Properties of Gottingen Minipig Brain Tissue in Simple Shear and Unconfined Compression. *J. Biomech. Eng.*, 2023. **145**(6).

[8] Feng, Y., et al., Characterizing White Matter Tissue in Large Strain Via Asymmetric Indentation and Inverse Finite Element Modeling. *J. Mech. Behav. Biomed. Mater.*, 2017. **65**: 490-501.

[9] Kaster, T., I. Sack, and A. Samani, Measurement of the Hyperelastic Properties of Ex Vivo Brain Tissue Slices. *J. Biomech.*, 2011. **44**(6): 1158-1163.

[10] Moran, R., J.H. Smith, and J.J. Garcia, Fitted Hyperelastic Parameters for Human Brain Tissue from Reported Tension, Compression, and Shear Tests. *J. Biomech.*, 2014. **47**(15): 3762-3766.

[11] MacManus, D.B., et al., Region and Species Dependent Mechanical Properties of Adolescent and Young Adult Brain Tissue. *Sci. Rep.*, 2017. **7**(1).

[12] Hosseini-Farid, M., et al., A Compressible Hyper-Viscoelastic Material Constitutive Model for Human Brain Tissue and the Identification of Its Parameters. *Int J Non Linear Mech* . 2019. **116**: 147-154.

[13] Felfelian, A.M., et al., Determining Constitutive Behavior of the Brain Tissue Using Digital Image Correlation and Finite Element Modeling. *Biomech. Model. Mechanobiol.*, 2019. **18**(6): 1927-1945.

[14] Hosseini-Farid, M., et al., A Poro-Hyper-Viscoelastic Rate-Dependent Constitutive Modeling for the Analysis of Brain Tissues. *J. Mech. Behav. Biomed. Mater.*, 2020. **102**.

[15] Subramaniam, D.R., et al., Cerebral Vasculature Influences Blast-Induced Biomechanical Responses of Human Brain Tissue. *Front Bioeng Biotechnol*, 2021. **9**: 744808.

[16] Zhang, L., R. Makwana, and S. Sharma, Brain Response to Primary Blast Wave Using Validated Finite Element Models of Human Head and Advanced Combat Helmet. *Front. Neurol.*, 2013. **4**: 88.

[17] Singh, D., D.S. Cronin, and T.N. Haladuick, Head and Brain Response to Blast Using Sagittal and Transverse Finite Element Models. *Int. J. Numer. Method. Biomed. Eng.*, 2014. **30**(4): 470-89.

[18] Wu, T., et al., Evaluation of Tissue-Level Brain Injury Metrics Using Species-Specific Simulations. *J. Neurotrauma*, 2021. **38**(13): 1879-1888.

[19] Bilston, L., Z. Liu, and N. Phan-Thien, Linear Viscoelastic Properties of Bovine Brain Tissue in Shear. *Biorheology*, 1997. **34**(6): 377-385.

[20] Hrapko, M., et al., Characterisation of the Mechanical Behaviour of Brain Tissue in Compression and Shear. *Biorheology*, 2008. **45**(6): 663-76.

[21] Chatelin, S., et al., Towards Child Versus Adult Brain Mechanical Properties. *J. Mech. Behav. Biomed. Mater.*, 2012. **6**: 166-173.

[22] Brands, D.W., P.H. Bovendeerd, and G.W. Peters, *Finite Shear Behavior of Brain Tissue under Impact Loading*, in *ASME International Mechanical Engineering Congress and Exposition*. 2000, American Society of Mechanical Engineers: Orlando, Florida, USA. p. 175-88.

[23] Bilston, L., Z. Liu, and N. Phan-Thien, Large Strain Behaviour of Brain Tissue in Shear: Some Experimental Data and Differential Constitutive Model. *Biorheology* 2001. **38**(4): 335-45.

[24] Feng, Y., et al., Measurements of Mechanical Anisotropy in Brain Tissue and Implications for Transversely Isotropic Material Models of White Matter. *J. Mech. Behav. Biomed. Mater.*, 2013. **23**: 117-132.

[25] Budday, S., et al., Rheological Characterization of Human Brain Tissue. *Acta Biomater.*, 2017. **60**: 315-329.

[26] Nicolle, S., M. Lounis, and R. Willinger, Shear Properties of Brain Tissue over a Frequency Range Relevant for Automotive Impact Situations: New Experimental Results. *Stapp Car Crash J*, 2004. **48**: 239-258.

[27] Darvish, K.K. and J.R. Crandall, Nonlinear Viscoelastic Effects in Oscillatory Shear Deformation of Brain Tissue. *Med Eng Phys*, 2001. **23**(9): 633-645.

[28] Arbogast, K.B. and S.S. Margulies, Material Characterization of the Brainstem from Oscillatory Shear Tests. *J. Biomech.*, 1998. **31**(9): 801-807.

[29] Thibault, K.L. and S.S. Margulies, Age-Dependent Material Properties of the Porcine Cerebrum: Effect on Pediatric Inertial Head Injury Criteria. *J. Biomech.*, 1998. **31**(12): 1119-26.

[30] Simons, M. and K. Trajkovic, Neuron-Glia Communication in the Control of Oligodendrocyte Function and Myelin Biogenesis. *J. Cell Sci.*, 2006. **119**(Pt 21): 4381-9.

[31] Weickenmeier, J., et al., The Mechanical Importance of Myelination in the Central Nervous System. *J. Mech. Behav. Biomed. Mater.*, 2017. **76**: 119-124.

[32] Budde, M.D. and J. Annese, Quantification of Anisotropy and Fiber Orientation in Human Brain Histological Sections. *Front. Integr. Neurosci.*, 2013. **7**: 3.

[33] Budday, S., et al., Mechanical Characterization of Human Brain Tissue. *Acta Biomater.*, 2017. **48**: 319-340.

[34] Velardi, F., F. Fraternali, and M. Angelillo, Anisotropic Constitutive Equations and Experimental Tensile Behavior of Brain Tissue. *Biomech. Model. Mechanobiol.*, 2006. **5**(1): 53-61.

[35] Nicolle, S., et al., Shear Linear Behavior of Brain Tissue over a Large Frequency Range. *Biorheology*, 2005. **42**(3): 209-223.

[36] Lujan, T.J., et al., Contribution of Glycosaminoglycans to Viscoelastic Tensile Behavior of Human Ligament. *J Appl Physiol (1985)*, 2009. **106**(2): 423-431.

[37] Yeh, F.C., et al., Deterministic Diffusion Fiber Tracking Improved by Quantitative Anisotropy. *PLoS One*, 2013. **8**(11): e80713.

[38] Bell, E.D., et al., Material Properties of Rat Middle Cerebral Arteries at High Strain Rates. *J. Biomech. Eng.*, 2018.

[39] Puso, M.A. and J.A. Weiss, Finite Element Implementation of Anisotropic Quasi-Linear Viscoelasticity Using a Discrete Spectrum Approximation. *J. Biomech. Eng.*, 1998. **120**(1): 62-70.

[40] D'Errico, J. *Fminsearchbnd, Fminsearchcon*. 2022 [cited 2021 September 15 2021]; Available from: https://www.mathworks.com/matlabcentral/fileexchange/8277-fminsearchbnd-fminsearchcon.

[41] Maas, S.A. and J.A. Weiss. *Febio Theory Manual*. 2007 [cited 2023 2/16/2023]; Available from: https://help.febio.org/docs/FEBioTheory-4-0/.

[42] Brands, D.W., P.H. Bovendeerd, and J.S. Wismans, On the Potential Importance of Non-Linear Viscoelastic Material Modelling for Numerical Prediction of Brain Tissue Response: Test and Application. *Stapp Car Crash J*, 2002. **46**: 103-21.

[43] Rashid, B., M. Destrade, and M.D. Gilchrist, Mechanical Characterization of Brain Tissue in Simple Shear at Dynamic Strain Rates. *J. Mech. Behav. Biomed. Mater.*, 2013. **28**: 71-85.

[44] Donnelly, B.R. and J. Medige, Shear Properties of Human Brain Tissue. *J. Biomech. Eng.*, 1997. **119**(4): 423-432.

[45] Fung, Y.C., *Biomechanics: Mechanical Properties of Living Tissues.* 2 ed. 1993, New York: Springer.

[46] Jin, X., et al., A Comprehensive Experimental Study on Material Properties of Human Brain Tissue. *J. Biomech.*, 2013. **46**(16): 2795-2801.

[47] Prange, M.T. and S.S. Margulies, Regional, Directional, and Age-Dependent Properties of the Brain Undergoing Large Deformation. *J. Biomech. Eng.*, 2002. **124**(2): 244-252.

[48] Jiang, Y., et al., Measuring the Linear and Nonlinear Elastic Properties of Brain Tissue with Shear Waves and Inverse Analysis. *Biomech. Model. Mechanobiol.*, 2015. **14**(5): 1119-28.

[49] Hamhaber, U., et al., Three-Dimensional Analysis of Shear Wave Propagation Observed by in Vivo Magnetic Resonance Elastography of the Brain. *Acta Biomater.*, 2007. **3**(1): 127-37.

[50] Mao, H., et al., Untangling the Effect of Head Acceleration on Brain Responses to Blast Waves. *J. Biomech. Eng.*, 2015. **137**(12): 124502.

[51] Moerman, K.M., et al., Digital Image Correlation and Finite Element Modelling as a Method to Determine Mechanical Properties of Human Soft Tissue in Vivo. *J. Biomech.*, 2009. **42**(8): 1150-3.

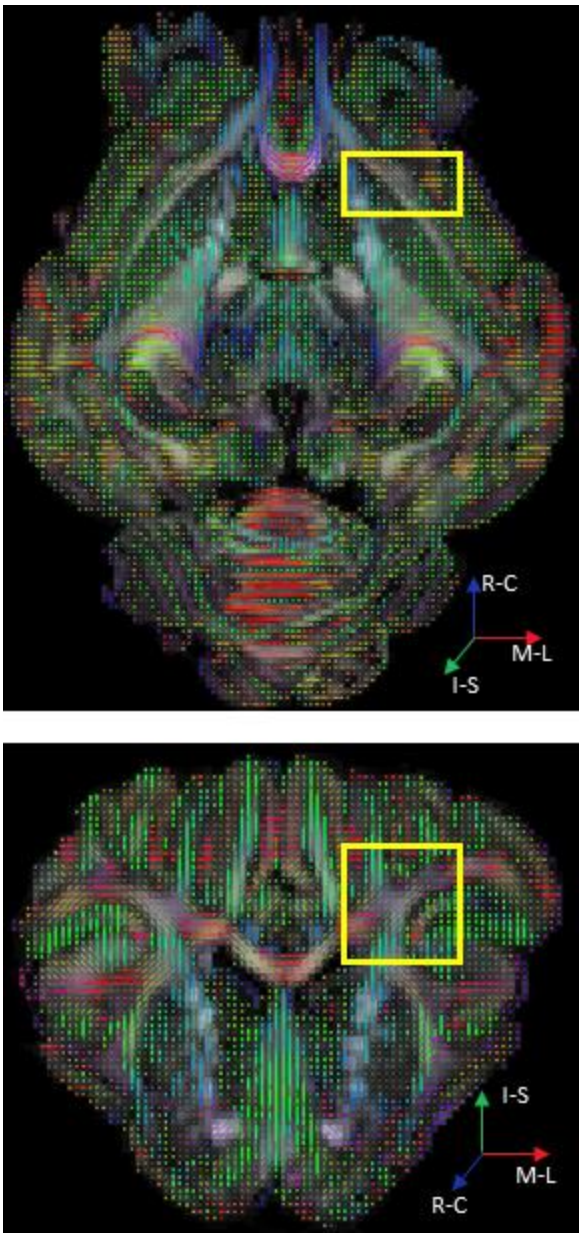

Figure 4.1 | Fiber direction in a mid-transverse (top) and coronal (bottom) section of the cerebrum. The region of tissue harvest and approximate size of samples in the B direction is shown by the yellow square. Note that in this region, fibers run in the rostral-caudal (R-C) direction in the center of the sample but disperse both inferior-superior (I-S) and medial-lateral (M-L) away from the center.

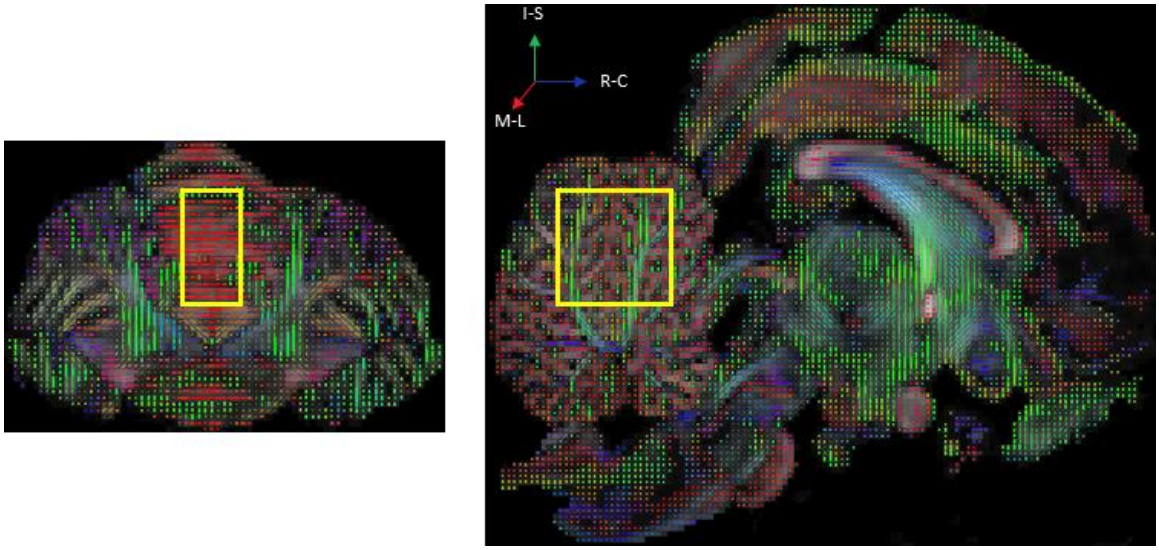

Figure 4.2 | Fiber directions on a coronal (left) and mid-sagittal (right) section of the cerebellum. The region of tissue harvest and approximate size of samples in the B direction is shown by the yellow square. Note that in this region fibers are mainly oriented in the medial-lateral (M-L) direction, though some are oriented in the inferior-superior (I-S) direction as well.

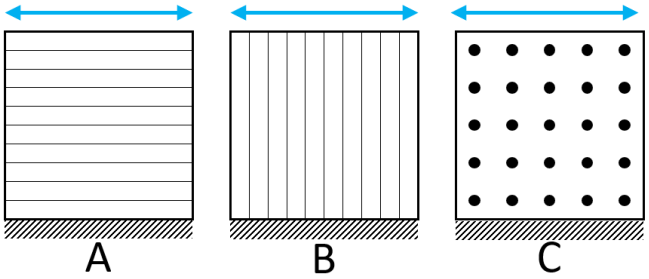

Figure 4.3 | Schematic of the A, B, and C directions relative to axon fiber direction (black lines and dots) and direction of applied shear (blue arrows).

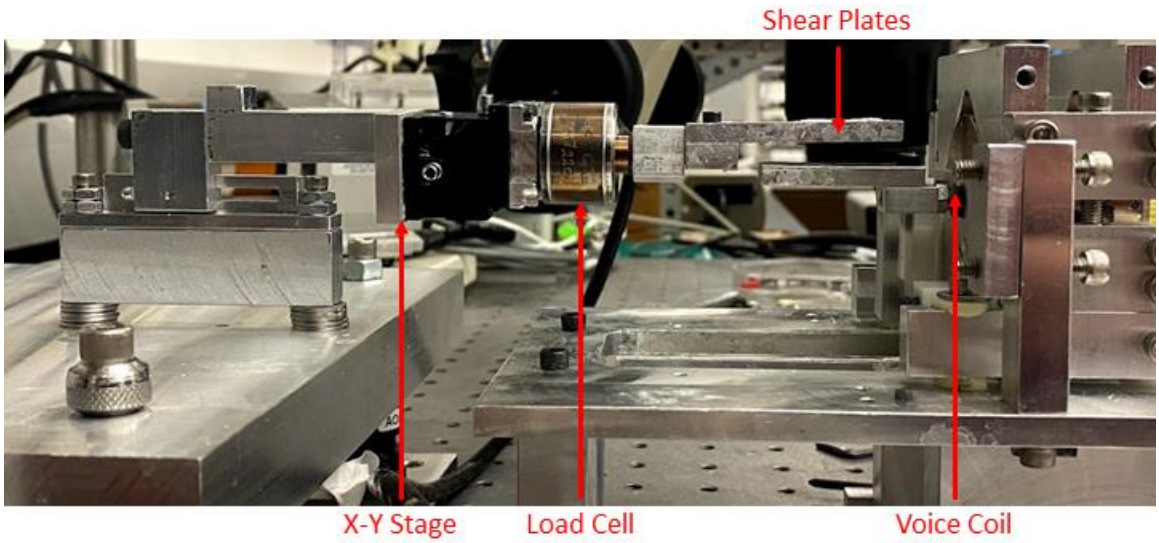

Figure 4.4 | Custom shear tester.

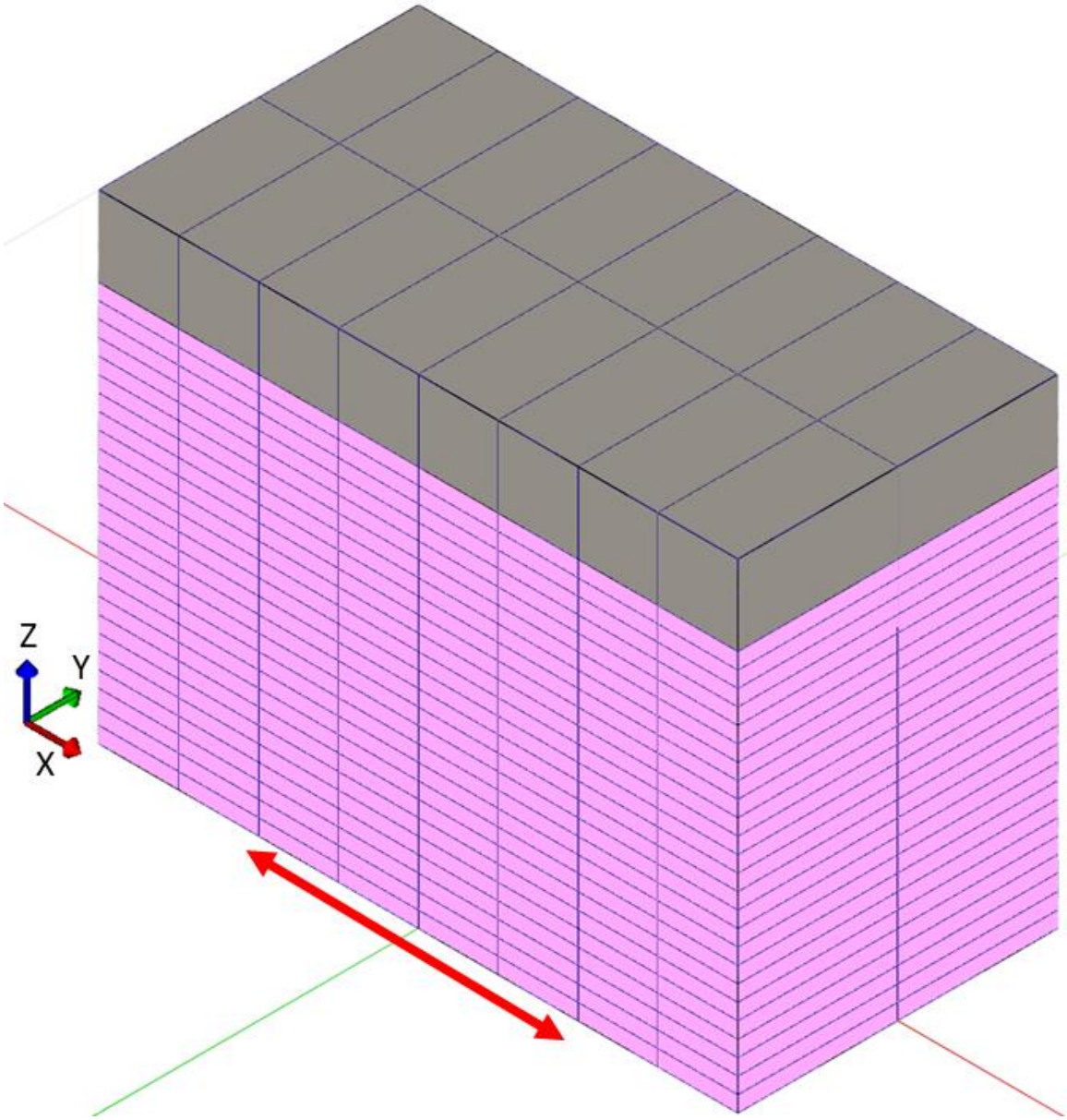

Figure 4.5 | Geometry of the finite element brain model. The top gray cuboid is the rigid body while the bottom pink cuboid is the brain tissue. Oscillatory displacements are applied to the bottom face in the direction shown by the red arrow and reaction forces are read between the two cuboids.

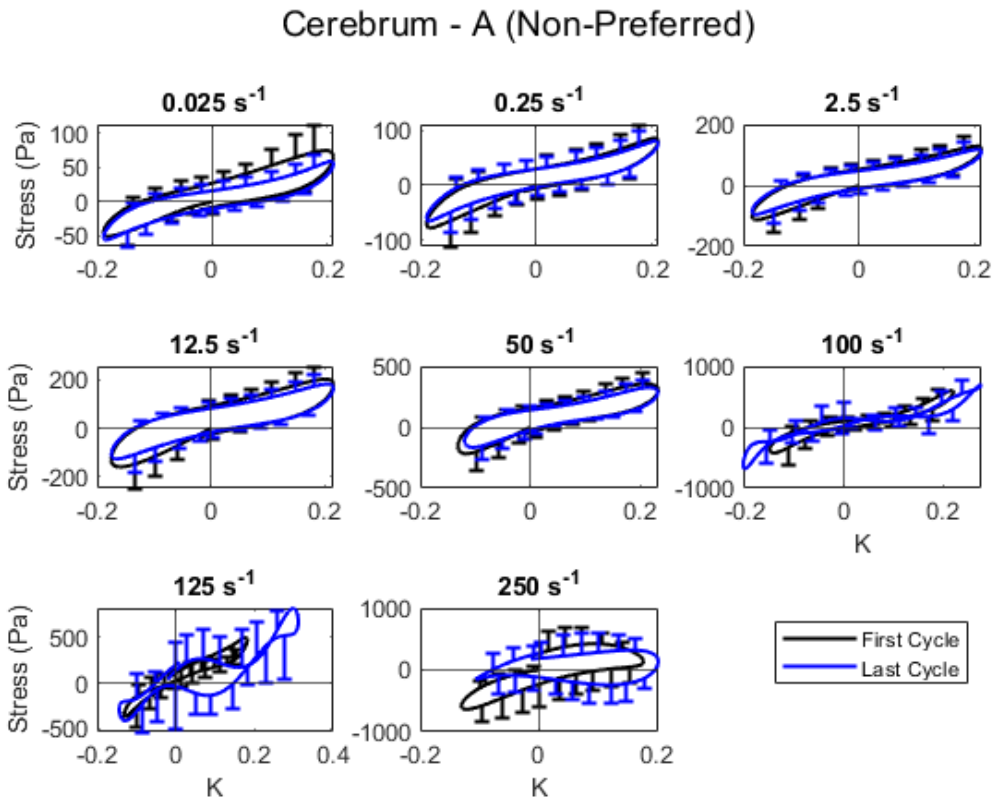

Figure 4.6 | Shear stress (average ± standard deviation) – shear strain hysteresis curves for the cerebrum in the non-preferred (A) direction.

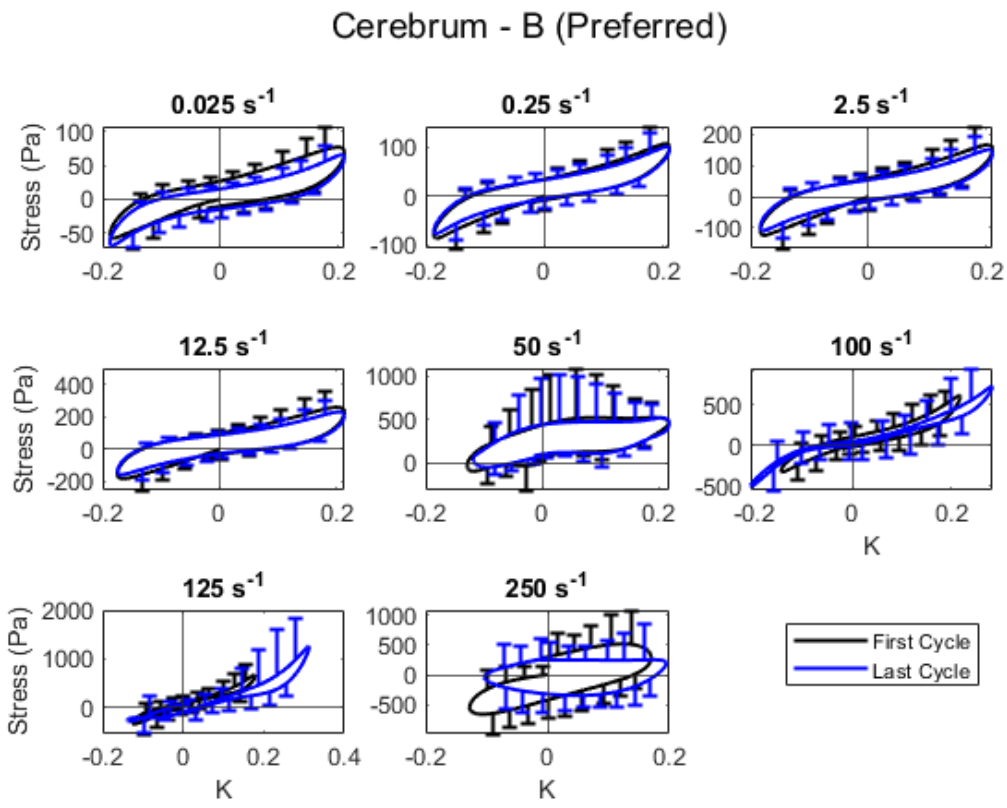

Figure 4.7 | Shear stress (average ± standard deviation) – shear strain hysteresis curves for the cerebrum in the preferred (B) direction.

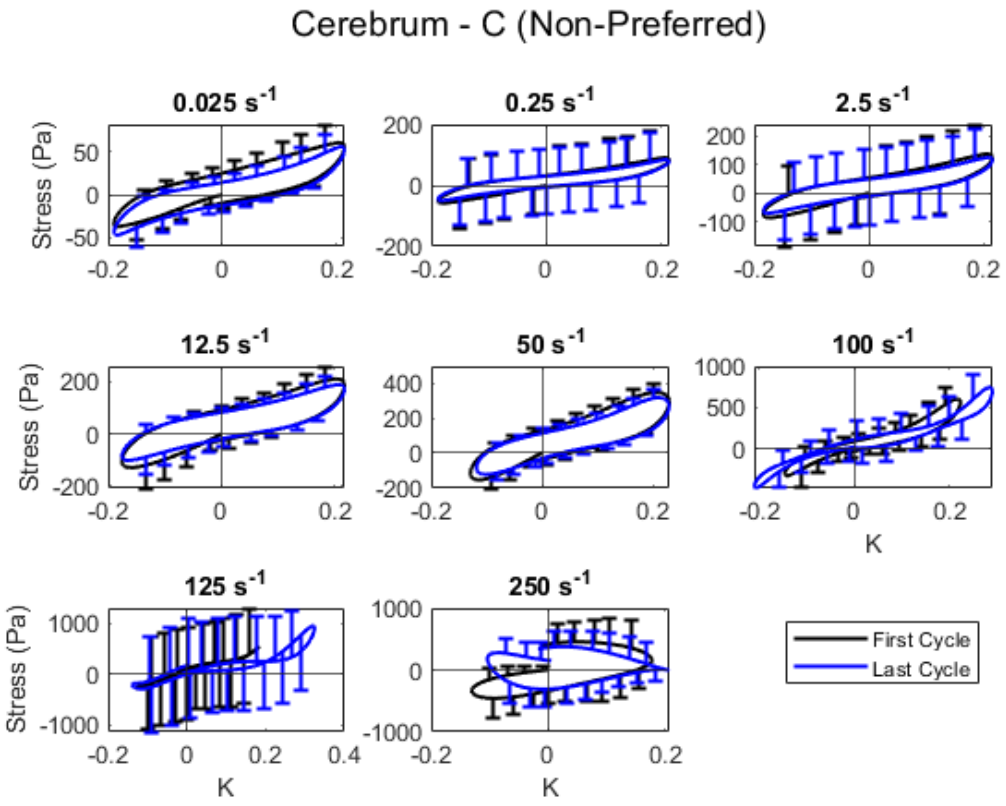

Figure 4.8 | Shear stress (average ± standard deviation) – shear strain hysteresis curves for the cerebrum in the non-preferred (C) direction.

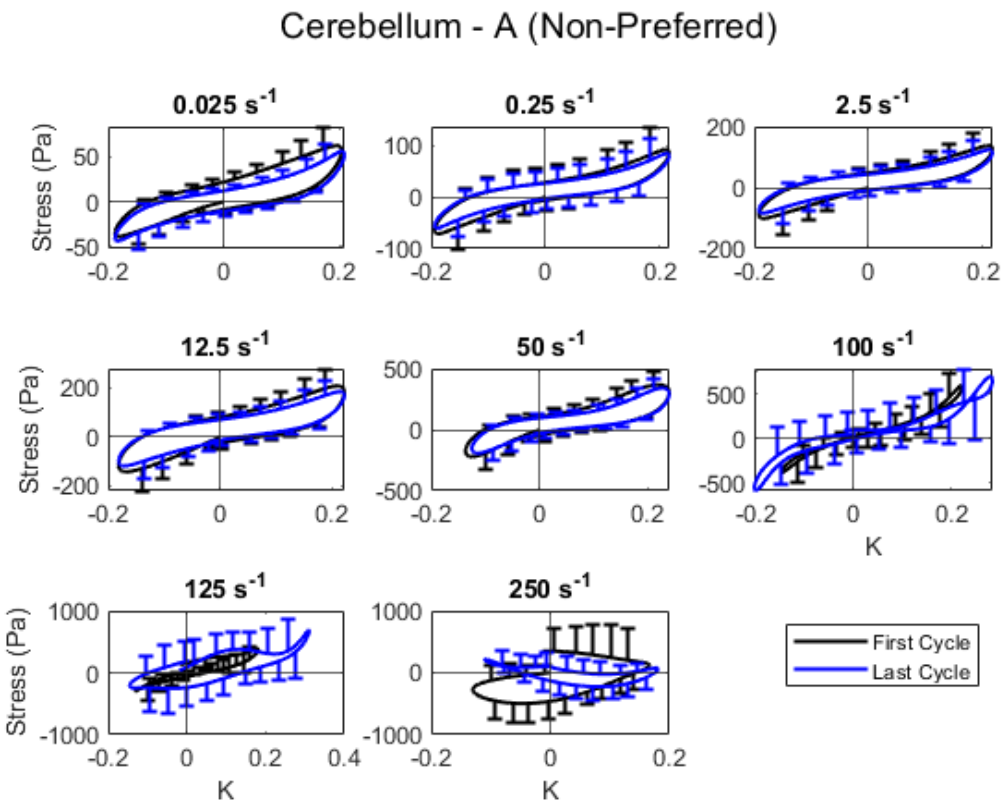

Figure 4.9 | Shear stress (average ± standard deviation) – shear strain hysteresis curves for the cerebellum in the non-preferred (C) direction.

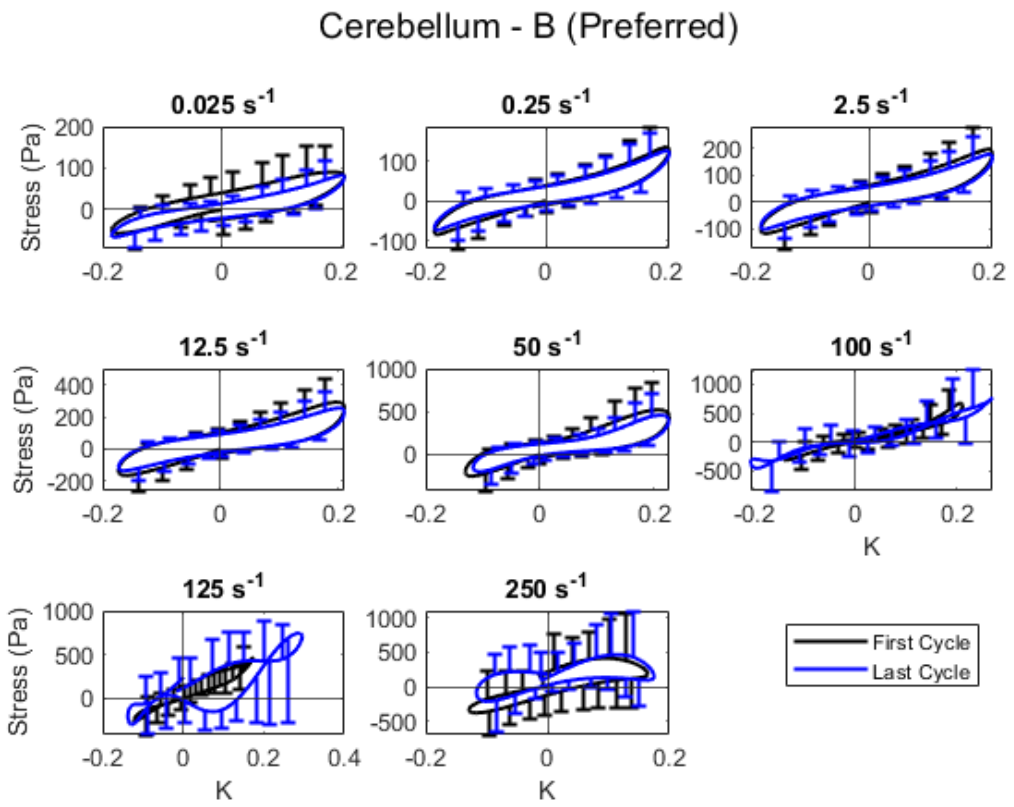

Figure 4.10 | Shear stress (average ± standard deviation) – shear strain hysteresis curves for the cerebellum in the preferred (B) direction.

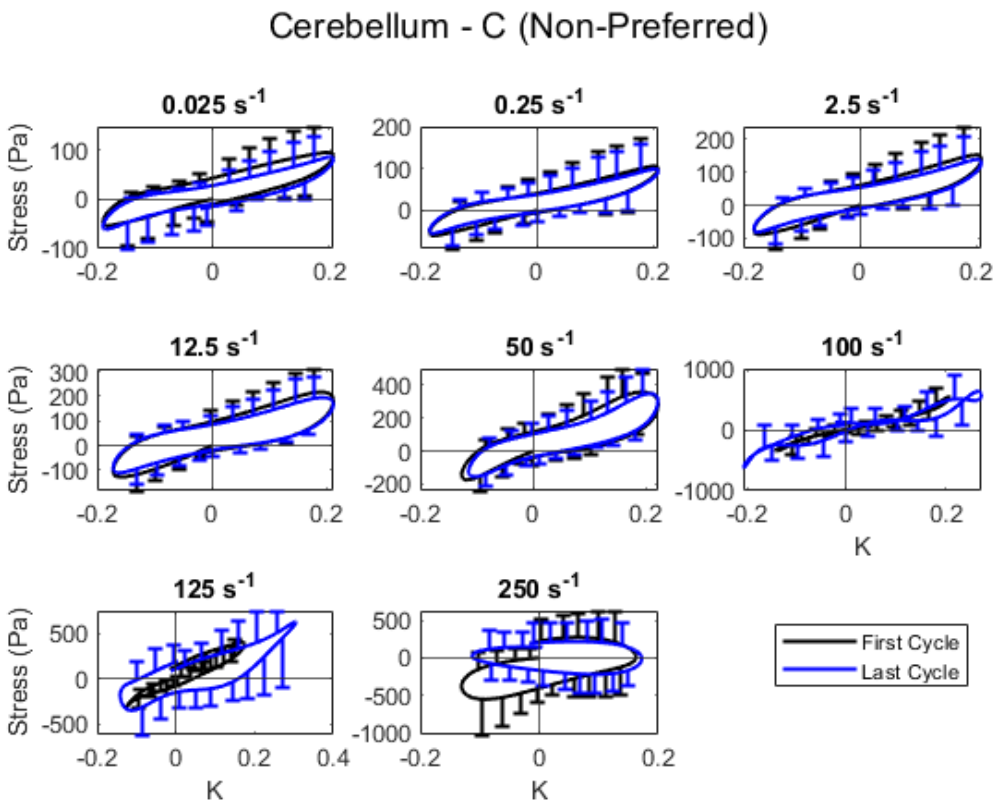

Figure 4.11 | Shear stress (average ± standard deviation) – shear strain hysteresis curves for the cerebellum in the non-preferred (C) direction.

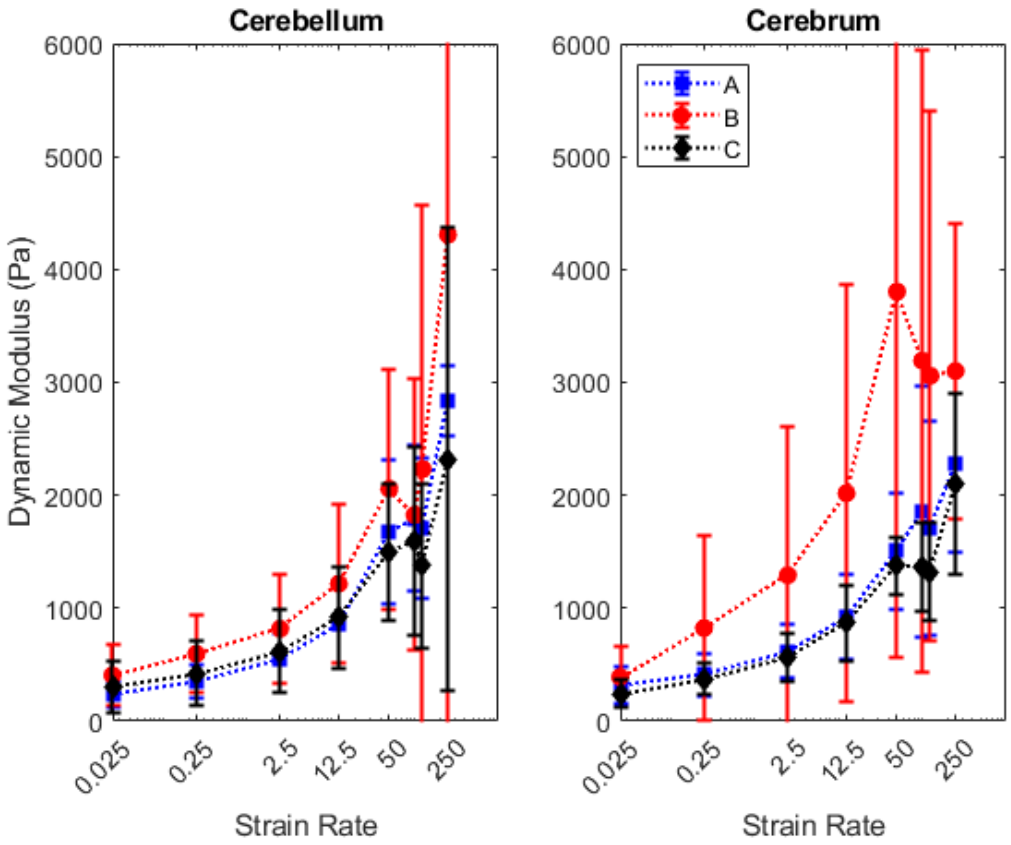

Figure 4.12 | Dynamic modulus (average ± standard deviation) as a function of strain rate and loading direction for the cerebellum and cerebrum.

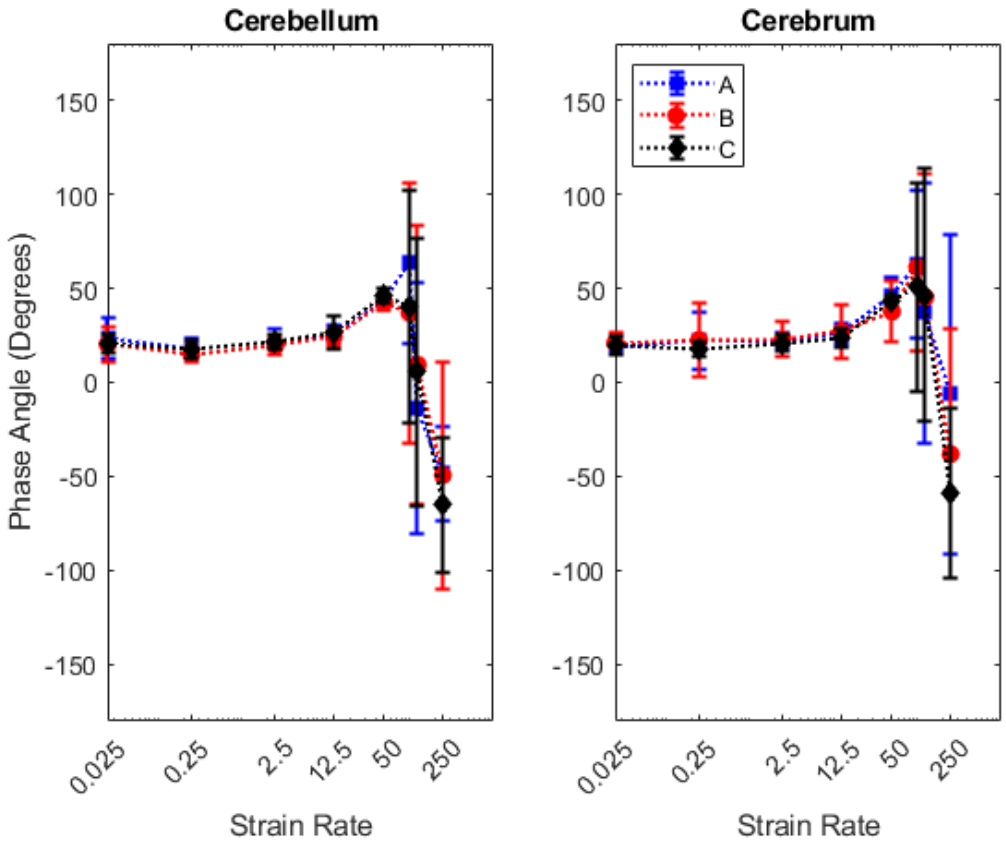

Figure 4.13 | Phase angle (average ± standard deviation) phase angle as a function of strain rate and loading direction for both the cerebellum and cerebrum.

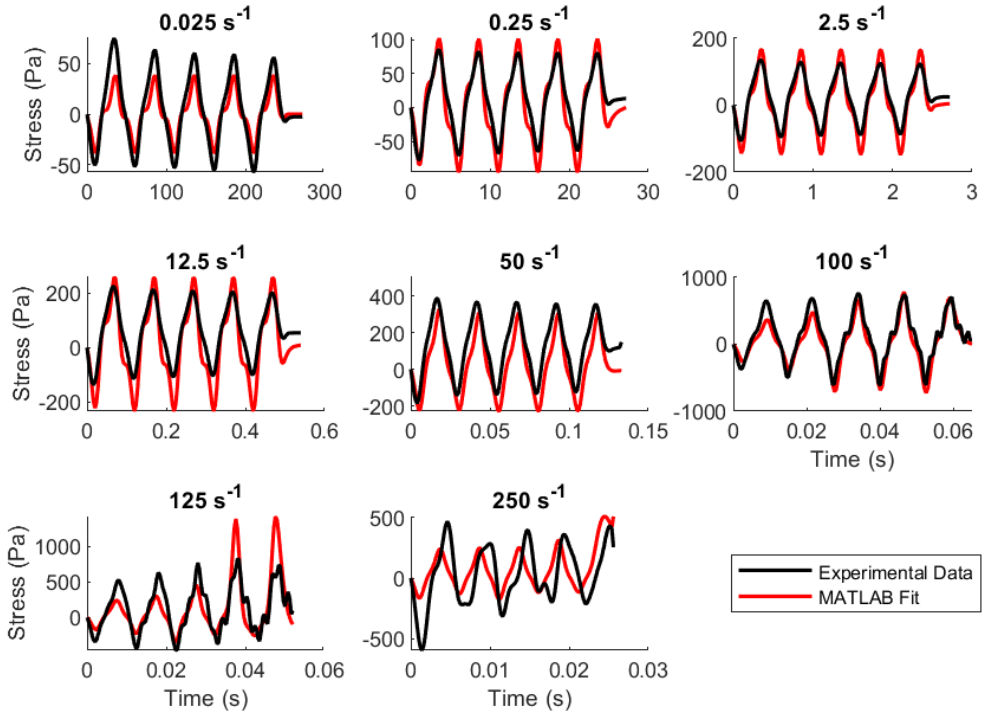

Figure 4.14 | Experimental data and MATLAB fits for the cerebrum in the A (non-preferred) direction.

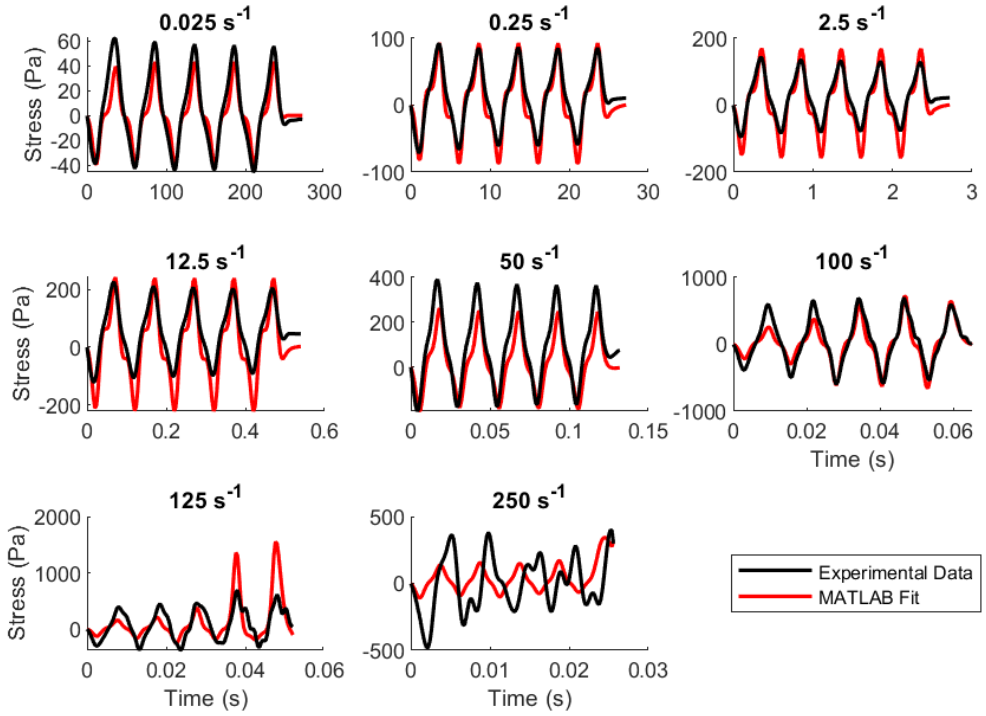

Figure 4.15 | Experimental data and MATLAB fits for the cerebellum in the A (non-preferred) direction.

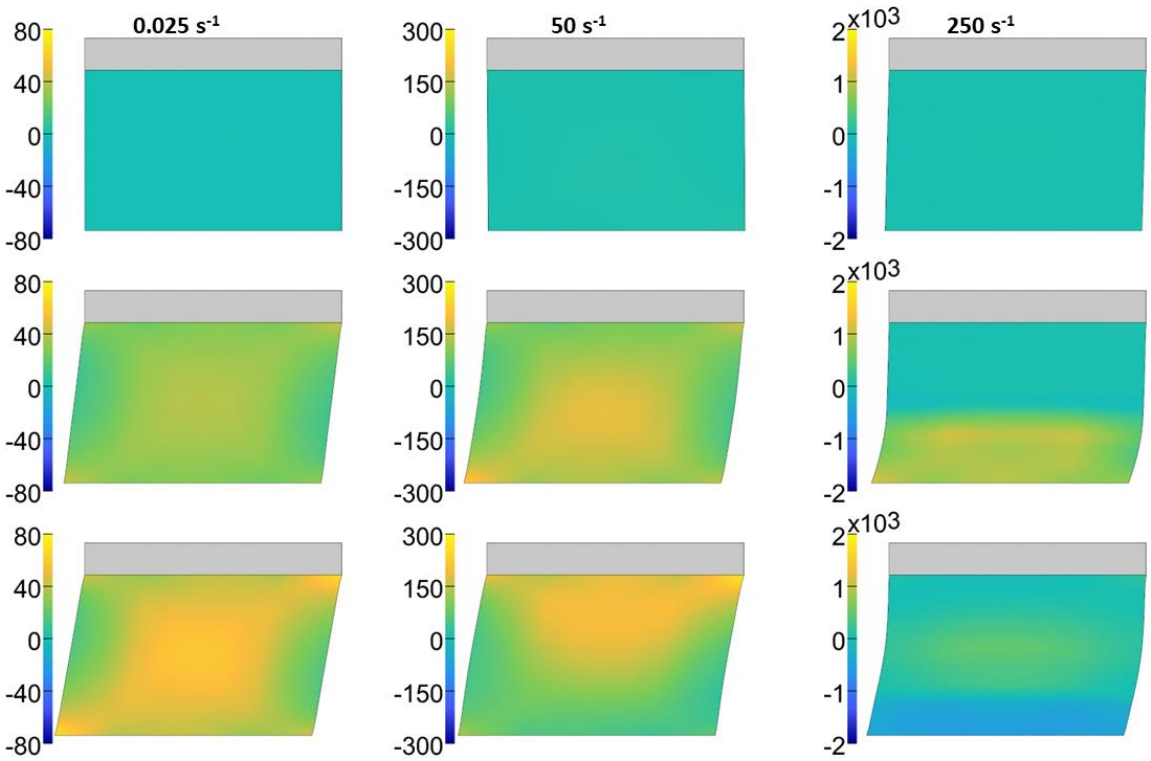

Figure 4.16 | Shear (XZ) stress distribution at the center plane for the finite element model during the first loading cycle at 0.025, 50, and 250 s^{-1}.

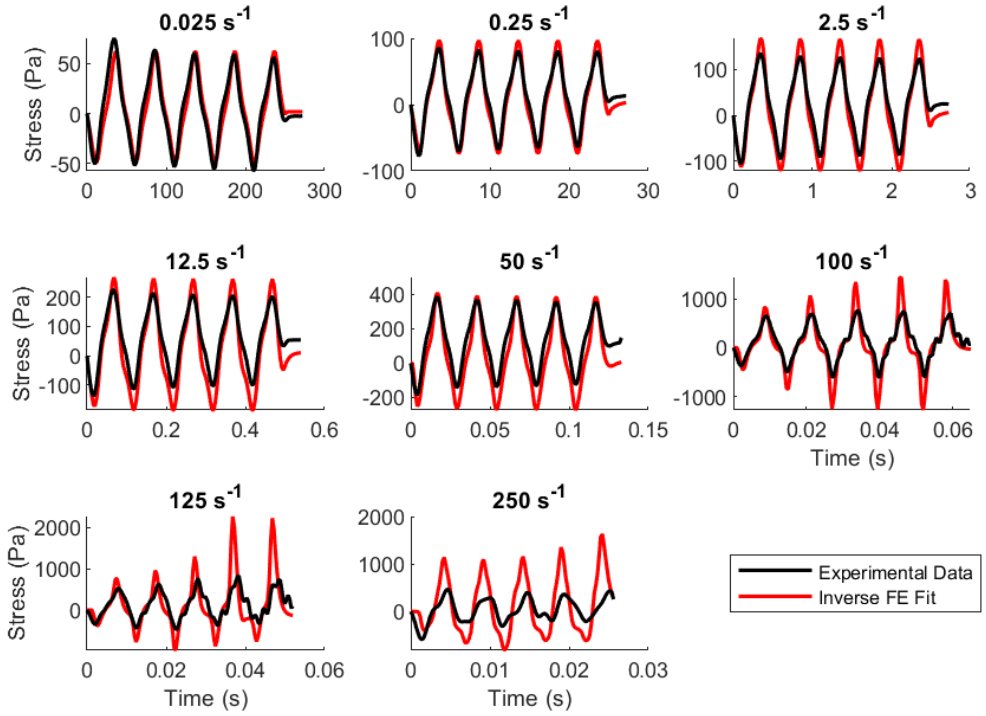

Figure 4.17 | Experimental data and inverse finite element fits for the cerebrum in the A (non-preferred) direction.

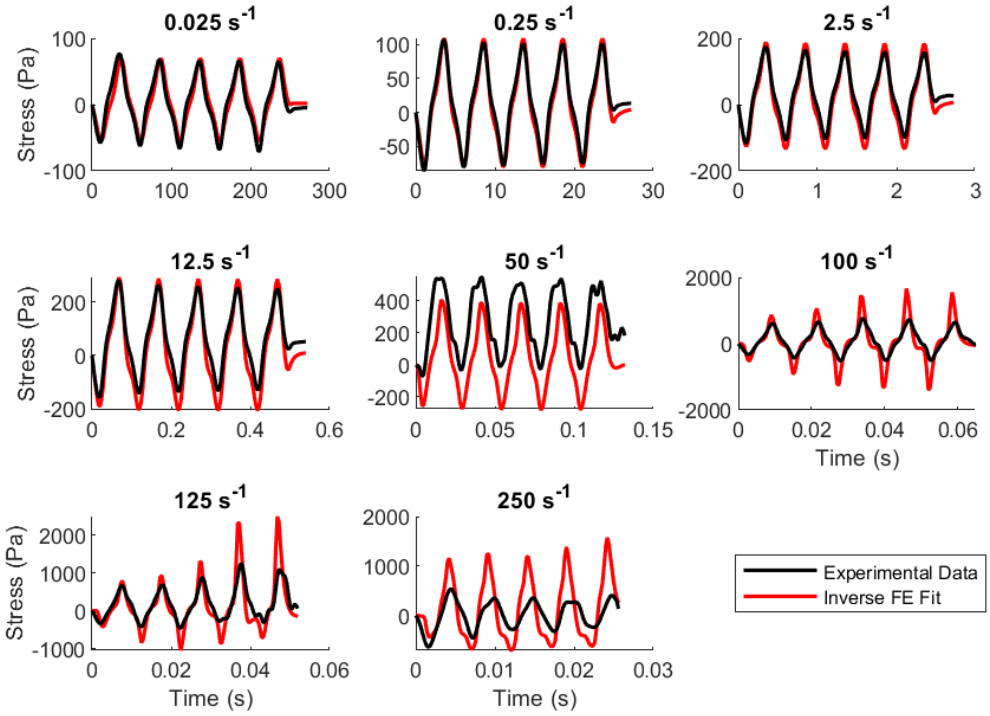

Figure 4.18 | Experimental data and inverse finite element fits for the cerebrum in the B (preferred) direction.

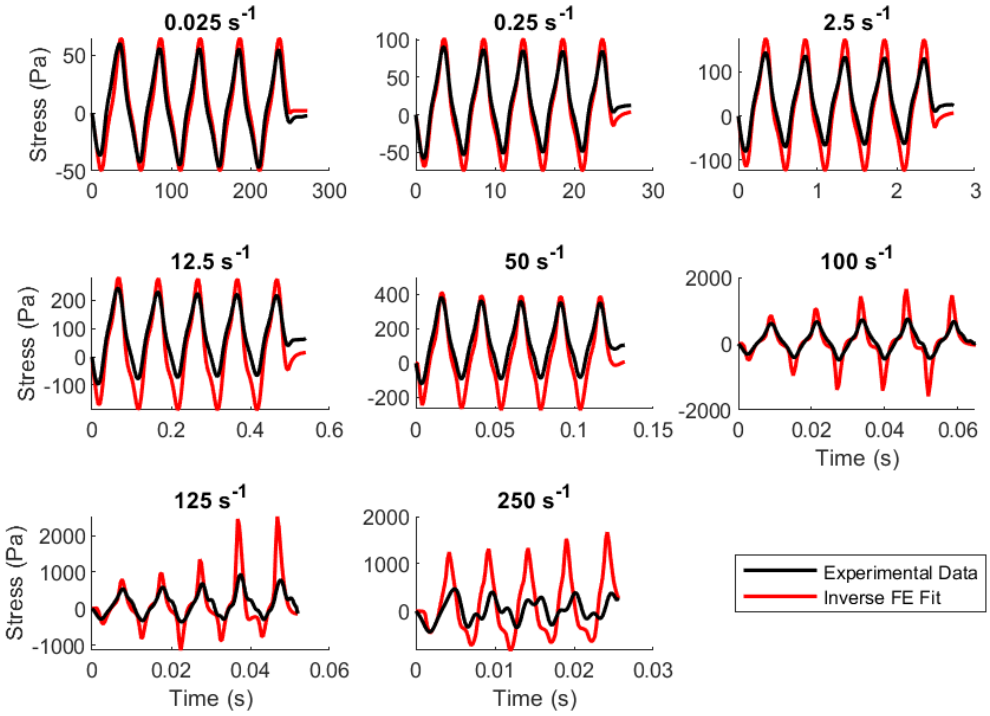

Figure 4.19 | Experimental data and inverse finite element fits for the cerebrum in the C (non-preferred) direction.

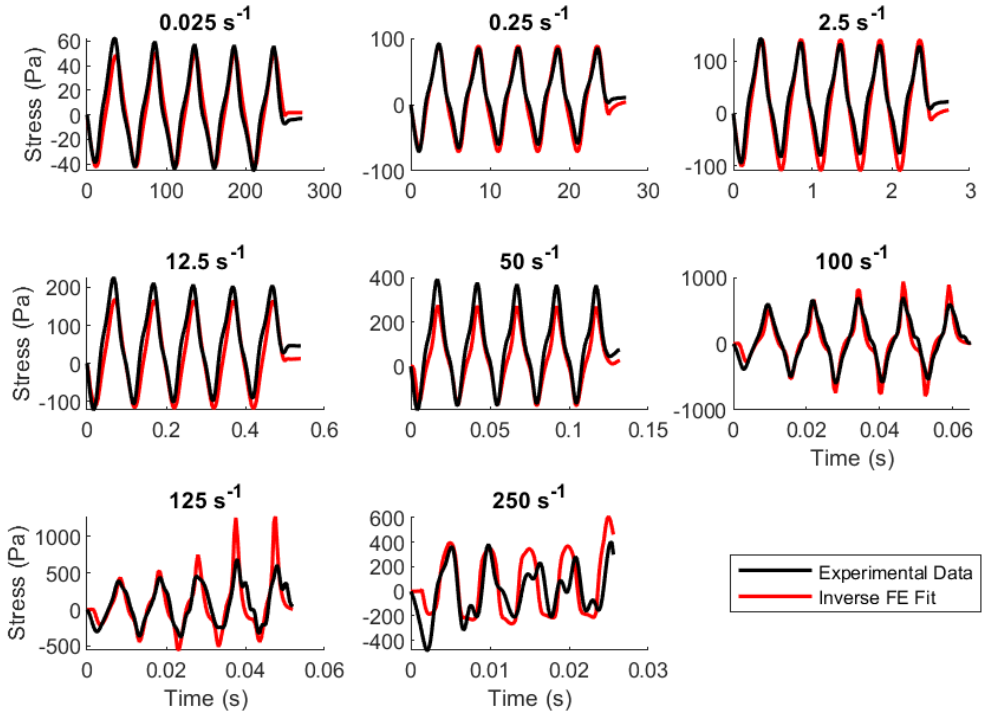

Figure 4.20 | Experimental data and inverse finite element fits for the cerebellum in the A (non-preferred) direction.

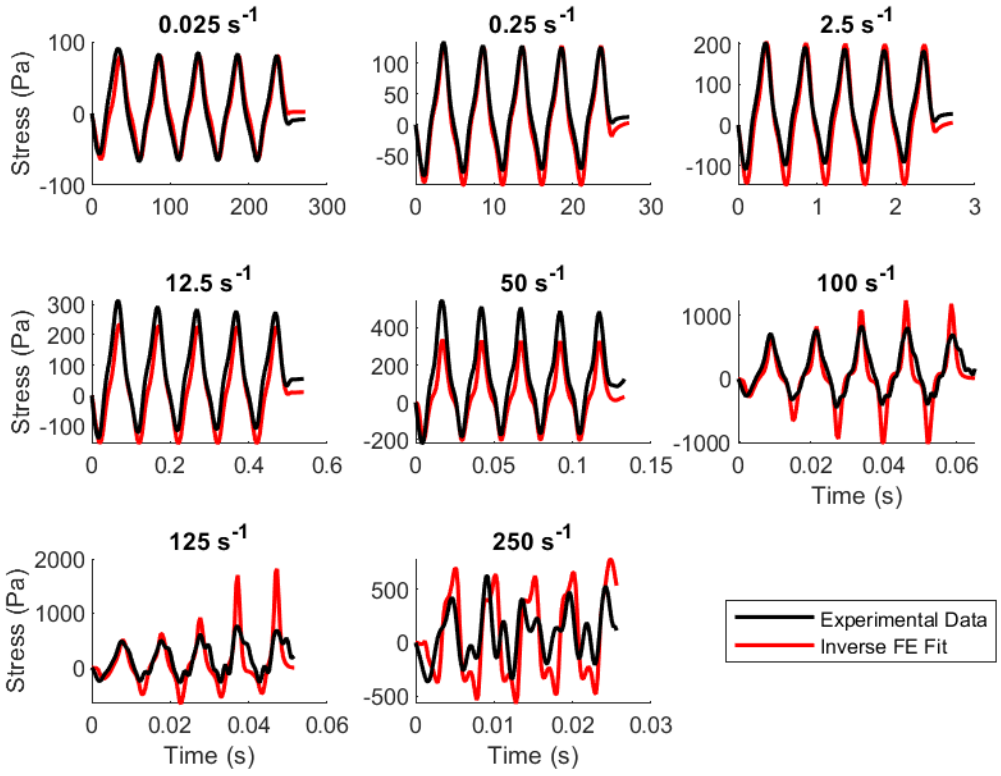

Figure 4.21 | Experimental data and inverse finite element fits for the cerebellum in the B (preferred) direction.

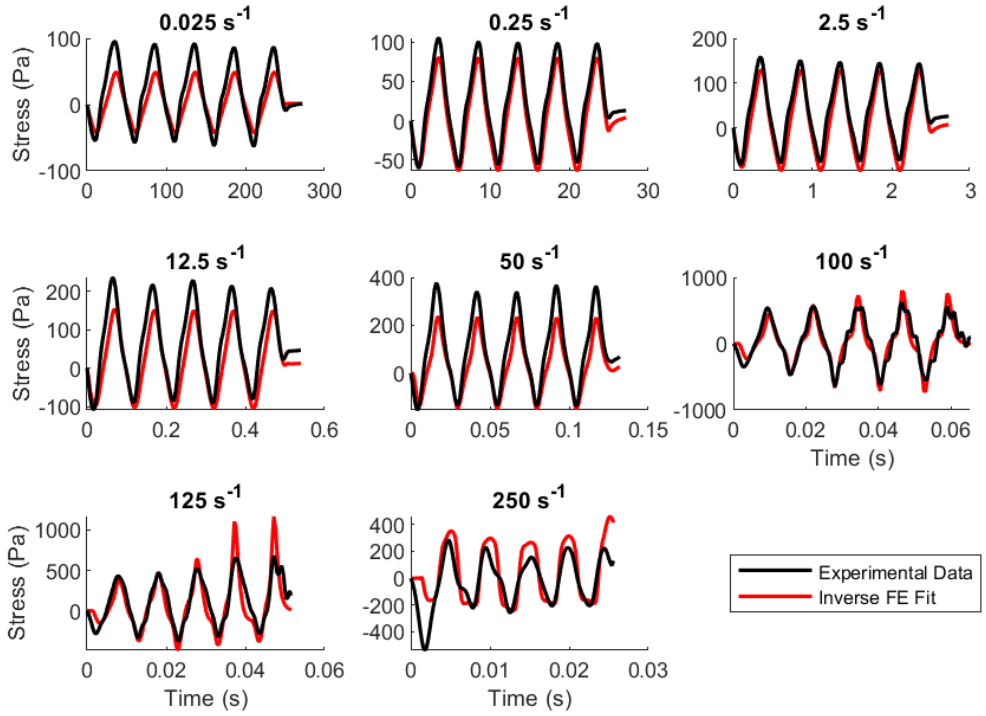

Figure 4.22 | Experimental data and inverse finite element fits for the cerebellum in the C (non-preferred) direction.

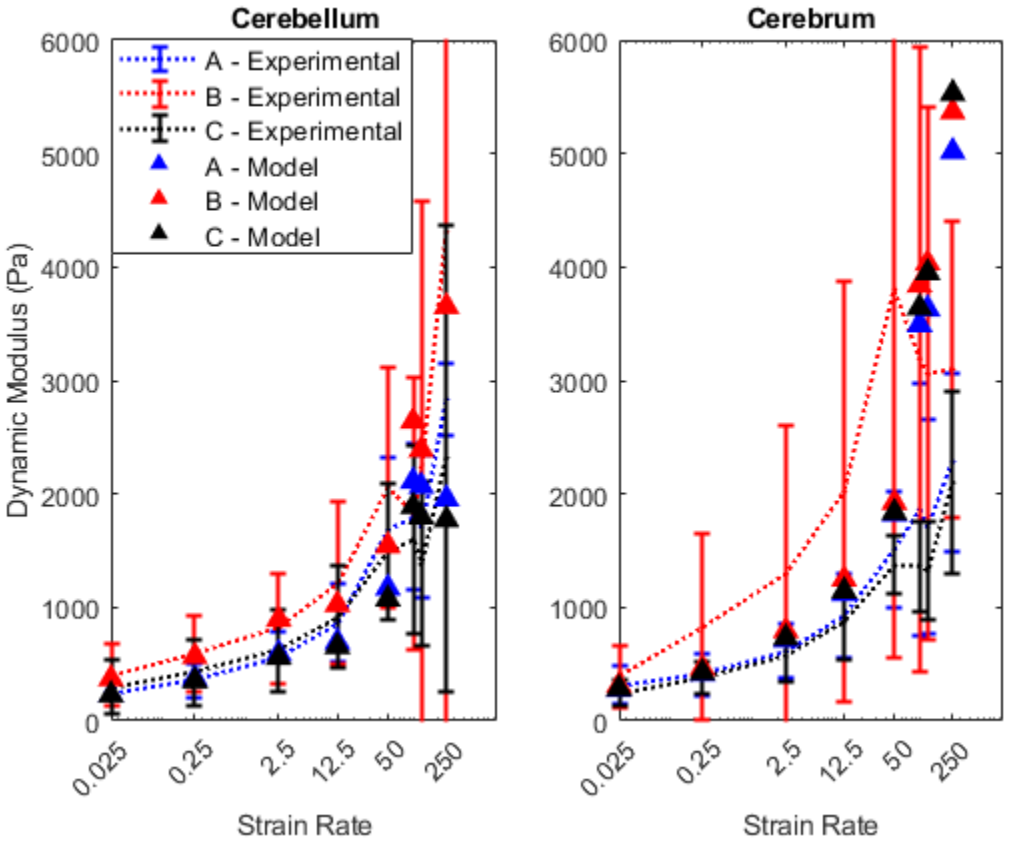

Figure 4.23 | Experimental dynamic modulus (dotted lines, average ± standard deviation) and dynamic modulus from FE models (triangles) as a function of strain rate and loading direction for the cerebellum and cerebrum.

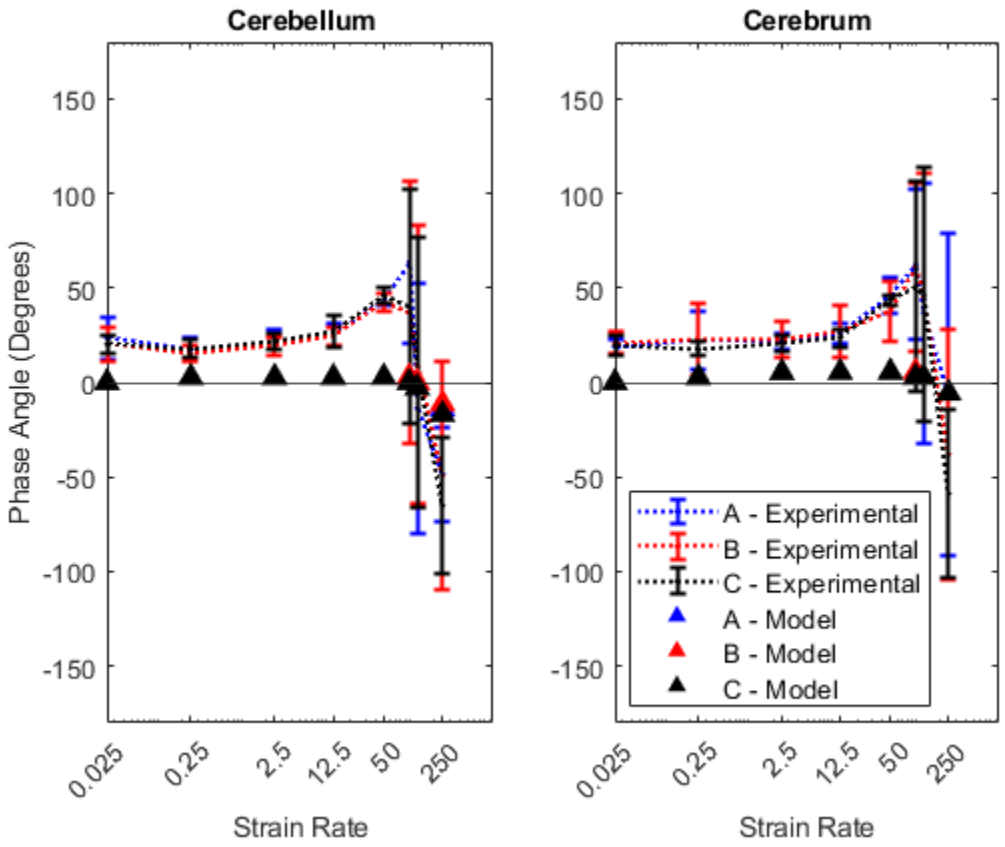

Figure 4.24 | Experimental phase angle (dotted lines, average ± standard deviation) and phase angle from FE simulations (triangles) as a function of strain rate and loading direction for both the cerebellum and cerebrum.

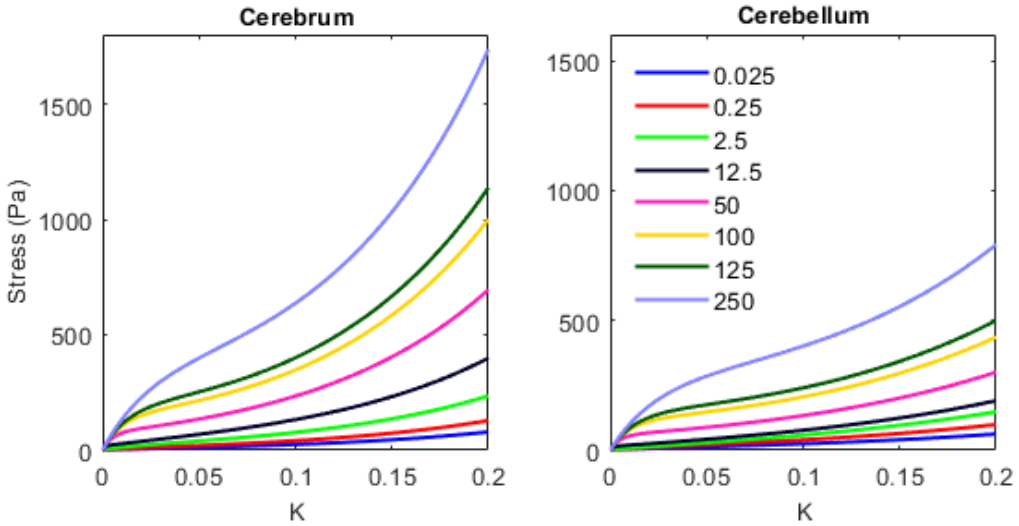

Figure 4.25 | Predicted stresses from the constitutive model in single ramp, homogeneous simple shear for the cerebrum and cerebellum when inertial terms are not considered.

Table 4.1 | Error and phase angle for MATLAB model fits average stress and strain data from the cerebrum and cerebellum in the non-preferred (A) direction. Negative phase shift denotes model leads experimental data.

Region	**Error Mode**	**Strain Rate (s^{-1})**							
		0.025	**0.25**	**2.5**	**12.5**	**50**	**100**	**125**	**250**
Cerebrum	Phase (°)	1.4	-5.2	2.3	3.2	17.3	3.2	-12.4	-50.1
	RMSE	0.2	0.3	0.2	0.2	0.4	0.3	0.7	1.0
Cerebellum	Phase (°)	8.4	-2.0	2.0	7.5	16.4	-5.5	-13.8	-81.2
	RMSE	0.3	0.2	0.2	0.3	0.4	0.4	0.8	1.3

Table 4.2 | Error and phase angle for cerebrum inverse finite element fits for all directions. Negative phase shift denotes model leads experimental data.

Direction	**Error Mode**	**Strain Rate (s^{-1})**							
		0.025	**0.25**	**2.5**	**12.5**	**50**	**100**	**125**	**250**
A	Phase (°)	13.68	0.7	0.7	0.7	4.3	-9.4	-24.5	-30.2
	RMSE	0.31	0.2	0.2	0.2	0.2	0.4	0.7	0.8
B	Phase (°)	13.7	1.4	1.4	1.4	16.6	-12.2	-13.0	-31.7
	RMSE	0.3	0.1	0.1	0.1	0.4	0.5	0.5	0.8
C	Phase (°)	15.1	2.2	1.4	1.4	5.0	-9.4	-15.1	-48.3
	RMSE	0.3	0.1	0.1	0.2	0.2	0.4	0.6	1.0

Table 4.3 | Error and phase angle for cerebellum inverse finite element fits for all directions. Negative phase shift denotes model leads experimental data.

Direction	Error Mode	Strain Rate (s^{-1})							
		0.025	**0.25**	**2.5**	**12.5**	**50**	**100**	**125**	**250**
A	Phase (°)	13.7	1.4	8.6	15.1	7.9	-2.9	-13.0	-15.1
	RMSE	0.3	0.1	0.2	0.3	0.2	0.4	0.5	0.8
B	Phase (°)	13.7	2.2	8.6	15.1	6.5	-2.2	-3.6	30.2
	RMSE	0.3	0.1	0.2	0.3	0.2	0.5	0.6	0.9
C	Phase (°)	15.1	2.9	9.3	18.0	10.8	-1.4	-7.9	10.8
	RMSE	0.3	0.1	0.2	0.4	0.3	0.4	0.5	0.6

Table 4.4 | Optimized parameters from the inverse finite element models of the cerebrum and cerebellum

Region	Parameter									
	c (Pa)	**m**	**g_1**	**g_2**	**g_3**	**g_4**	**g_5**	**ξ (Pa)**	**α**	**β**
Cerebrum	323	22.1	0.8	1.1	3.1	0	92.2	300	4.6	2
Cerebellum	352.4	16.3	0.9	1.1	0	0	65.1	1611	24.6	2

CHAPTER 5

CONCLUSION

The work presented in this dissertation focuses on constitutive modeling of brain tissue at strain rates and in loading modes relevant to the simulation of blast injury. It also describes preliminary work focused on quantifying microvascular disruption resulting from large brain tissue deformations. In Chapter 3, we fit hyper-viscoelastic constitutive models to experimental data from quasi-static and high-rate shear and compression tests on Göttingen minipig brain tissue which can be implemented in finite element simulations of blast injury. In Chapter 4, we conducted oscillatory shear tests over a large rate continuum to better define the response of brain tissue in simple shear over a broader range of rates than in Chapter 3, as well as to evaluate anisotropy. Evidence of wave propagation in high-rate tests led to the development of inverse finite element models to fit anisotropic hyper-viscoelastic constitutive models suitable for the simulation of both conventional and blast injury. Summaries of important findings from these chapters and future work are discussed in this chapter.

5.1 Summary of Chapter 3: Rate- and Region-Dependent Mechanical Properties of Göttingen Minipig Brain Tissue in Simple Shear and Unconfined Compression

1. Brain tissue from the cerebrum, cerebellum, and brainstem exhibits pronounced rate dependence with a significant difference in shear modulus between 150 and 300 s^{-1} and QS rates but no difference between 150 and 300 s^{-1} in either shear or compression.
2. One- and two-term Ogden hyperelastic models provided equivalent fits in both quasi-static shear and compression, performing better than the Mooney-Rivlin model.
3. Two sets of hyper-viscoelastic models were fit, one fit to either shear or compression data (unidirectional) and the other simultaneously fit to both shear and compression data (bidirectional). The unidirectional compression and shear models provide the best quality fit for all brain regions. However, bidirectional models still offer a good fit, especially at high rates though they may struggle to predict the low-rate shear response.

5.2 Summary of Chapter 4: Region-Specific Anisotropy and Rate Dependence in Göttingen Minipig Brain Tissue

1. Tissue from the cerebrum and cerebellum was shown to be transversely isotropic in simple shear, with the preferred direction corresponding to fibers parallel to the shear plane and perpendicular to the direction of loading.
2. Tissue in all regions and directions showed a pronounced phase shift between stress and strain waveforms at rates above 100 s^{-1}, suggesting wave propagation

through the tissue samples at high rates. The presence of wave propagation was further validated by examination of finite element models of experiments. Consequently, inverse finite element models were developed to fit transversely isotropic hyper-viscoelastic constitutive models.

3. The inverse finite element fits predicted stress well for all loading cycles up to 50 s^{-1} for all regions and loading directions. At 100 and 125 s^{-1}, the model fits predicted the first two cycles of loading well before overpredicting stresses in subsequent cycles. At 250 s^{-1}, the cerebral model can predict the initial ramp loading well, while the cerebellar model predicts all loading after the first ramp well.

5.3 Future Work

1. In Chapter 3, we observed variations in the concavity of average shear stress-strain curves at both QS and high rates. Work by Haslach et al. [1, 2] suggests that tension or compression superimposed on simple shear loading may change the concavity observed during ramp tests. This dependence on transverse tension/compression may be doubly important in the brain as the propensity of brain tissue to deform under its weight [3] may suggest that the tissue is under a substantial degree of pre-strain *in vivo*. Experiments comparing various degrees of transverse compression and tension combined with simple shear loading should be performed over a range of strain rates to develop a constitutive model which can account for any change in response as a function of pre-compression/tension.

Additional work should also quantify the degree of pre-strain evident in brain tissue.

2. The influence of mixed white/gray matter samples in Chapters 3 and 4 may be a substantial source of error due to variations in material properties between white and gray matter [4]. Future work should attempt to move away from modeling mixed samples towards smaller, isolated white or gray matter tissues or work to separate the effects of white and gray matter through finite element modeling.
3. The constitutive model development in this paper focused on tissue from Göttingen minipigs. While this is useful for developing finite element injury models in porcine models, it cannot be readily adapted to human injury models, the ultimate goal of injury simulations. Ideally, further characterization of brain tissue should aim to use human brain tissue recovered either as a byproduct from surgical resection or tissue donor programs, assuming that tissue can be retrieved within a few hours of death. The study of human brain tissue will additionally allow for the direct quantification of the differences in material properties between porcine and human brain tissue.
4. The inverse finite element models in Chapter 4 were developed without information about the local experimental deformations. Future inverse finite element modeling should be refined by including experimental deformation maps recorded using digital image correlation (DIC) [5]. DIC should be captured from multiple directions to develop a 3D deformation field. Even recording deformations in the shear plane would be useful in the experimental quantification of wave propagation.

5. Brain tissue is highly hydrated and has been shown to exhibit biphasic or poroelastic behavior [6-8]. Permeability [9, 10] and compression, shear, and tension tests should be performed on brain tissue and used to develop either poroelastic or poro-viscoelastic constitutive models for brain tissue. These models should also be compared to quasi-linear and non-linear viscoelastic models to evaluate benefits compared to more common models in the literature.
6. We observed a trend of brain tissue tearing at lower strains at higher rates than QS rates in single ramp shear experiments. While we did not quantify this relationship due to difficulties defining failure in the experiments conducted in Chapter 3, this trend may warrant further investigation, as bulk tissue failure may be correlated with axon disruption. Examination of tissue failure, either represented by visible tearing on test video or from load signals, should be evaluated as a function of strain rate in both shear and tension. This work should also aim to test separate white and gray matter specimens and factor in fiber direction to relate failure to axon damage [11].

5.4 References

[1] Haslach, H.W., Jr., J.M. Gipple, and L.N. Leahy, Influence of High Deformation Rate, Brain Region, Transverse Compression, and Specimen Size on Rat Brain Shear Stress Morphology and Magnitude. *J. Mech. Behav. Biomed. Mater.*, 2017. **68**: 88-102.

[2] Haslach, H.W., Jr., L.N. Leahy, and A.H. Hsieh, Transient Solid-Fluid Interactions in Rat Brain Tissue under Combined Translational Shear and Fixed Compression. *J. Mech. Behav. Biomed. Mater.*, 2015. **48**: 12-27.

[3] Budday, S., et al., Fifty Shades of Brain: A Review on the Mechanical Testing and Modeling of Brain Tissue. *Arch. Comput. Methods Eng.*, 2019. **27**(4): 1187-1230.

[4] Budday, S., et al., Mechanical Characterization of Human Brain Tissue. *Acta Biomater.*, 2017. **48**: 319-340.

[5] Moerman, K.M., et al., Digital Image Correlation and Finite Element Modelling as a Method to Determine Mechanical Properties of Human Soft Tissue in Vivo. *J. Biomech.*, 2009. **42**(8): 1150-3.

[6] Greiner, A., et al., Poro-Viscoelastic Effects During Biomechanical Testing of Human Brain Tissue. *Front. Mech. Eng.*, 2021. **7**.

[7] Hosseini-Farid, M., et al., A Poro-Hyper-Viscoelastic Rate-Dependent Constitutive Modeling for the Analysis of Brain Tissues. *J. Mech. Behav. Biomed. Mater.*, 2020. **102**.

[8] Comellas, E., et al., Modeling the Porous and Viscous Responses of Human Brain Tissue Behavior. *Comput. Methods Appl. Mech. Eng.*, 2020. **369**.

[9] Reynaud, B. and T.M. Quinn, Anisotropic Hydraulic Permeability in Compressed Articular Cartilage. *J. Biomech.*, 2006. **39**(1): 131-7.

[10] Holmes, M.H. and V.C. Mow, The Nonlinear Characteristics of Soft Gels and Hydrated Connective Tissues in Ultrafiltration. *J. Biomech.*, 1990. **23**(11): 1145-1156.

[11] Cloots, R.J., et al., Micromechanics of Diffuse Axonal Injury: Influence of Axonal Orientation and Anisotropy. *Biomech. Model. Mechanobiol.*, 2011. **10**(3): 413-22.

APPENDIX A

INVERSE FINITE ELEMENT MODEL SENSITIVITY ANALYSIS

To evaluate our inverse finite element fitting and modeling approach, we performed a sensitivity analysis in FEBio using UncertainSCI [1, 2]. To examine the sensitivity of the constitutive models presented in Chapter 4 to single ramp loading, we developed single ramp FE models for each of the eight strain rates evaluated, from 0.025 to 250 s^{-1} by applying a constant strain rate displacement to the bottom face of the brain tissue cuboid model to a maximum displacement consistent with a value of K = 0.2. For the A direction models, we evaluated the sensitivity at each rate to the Ogden and Prony series parameters (the parameters optimized on the A direction model in Chapter 4). Additionally, we evaluated a B direction model at the lowest rate of 0.025 s^{-1} (the only optimized B direction rate in Chapter 4) to examine model sensitivity to the fiber component parameters.

The FEBio UncertainSCI script runs a specified FE model several times and varies the input parameters randomly between a set minimum and maximum bounds, where any value of the parameter has the same probability of being sampled (i.e., a beta distribution with parameters $\alpha = \beta = 1$). The number of samples taken is controlled by setting the order of a polynomial used in the polynomial chaos expansion method used by UncertainSCI. For our analysis we used a fourth order polynomial, resulting in 340

evaluated material parameter sets (individual model runs) for the A direction models and 45 evaluated sets for the B direction model. Sensitivity was tested over the full range of values considered during optimization in Chapter 4 and is detailed in Table A.1.

The resulting global sensitivities (first order Sobol indices) reported by FEBio UncertainSCI for the A direction models is shown in Table A.2. For the A direction models, all rates show the highest sensitivity to the stiffness parameter c from the one-term Ogden model governing the hyperelastic response of the material. The sensitivity to the non-linearity parameter m from the Ogden model is also high for all rates. To further isolate the effects of the Prony series model, we reran the sensitivity analysis in the A direction considering just the 5 g_i parameters (Table A.3). As assumed in Chapter 4, a model's sensitivity to a given g_i parameter is increased when the inverse of strain rate is close to the corresponding value of τ_i. The values of g_2 and g_3 are at their highest for strain rates with an inverse on the order of the corresponding τ_i value (2.5 s^{-1} for $\tau_2 = 0.1$ and 12.5 s^{-1} for $\tau_3 = 0.01$). Interestingly, this does not hold true for g_1, where the lowest rate has the highest sensitivity or g_4 and g_5 which show the highest sensitivities at 100 s^{-1} and 250 s^{-1} respectively. In the case of g_1 this is likely due to the other parameters having very little effect on the lowest rate oscillation, while g_5 is showing the most sensitivity at the rate with the lowest inverse strain rate value. For most values of g_i, sensitivities are high but not necessarily maximized at the strain rate that the values were optimized for in Chapter 4, with the values of $g_1, g_3,$ and g_5 having the highest sensitivity of any g_i parameter at the rates they were optimized at, though g_2 and g_4 show relatively low sensitivities at the rates they were optimized through (12.5 s^{-1} and 125 s^{-1}). However, both parameters show relatively low sensitivity even at their maximum values, suggesting

they may have little impact on the constitutive model results. This is especially true for g_4 which optimized to 0 in both the cerebral and cerebellar models in Chapter 4.

Global sensitivities of fiber model parameters for a 0.025 s^{-1} ramp in the B direction (Table A.4) show the greatest sensitivity to the exponential power parameter β, followed by the fiber stiffness parameter ξ, and finally the exponential coefficient parameter α. While model sensitivity to β is high, optimizations for both the cerebral and cerebellar models in Chapter 4 optimized it to its minimum value of 2, suggesting that the parameter results in the model becoming overly stiff. Unsurprisingly, the fiber stiffness parameter, which acts to linearly stiffen the strain energy function, also has a significant impact on model value, more so than the exponential coefficient parameter. However, both the α and ξ parameters saw a similar increase from the cerebral to the cerebellar model in Chapter 4, increasing by 535% and 537% respectively despite the sensitivity of ξ being almost twice that of α.

References

[1] Burk, K.M., A. Narayan, and J.A. Orr, Efficient Sampling for Polynomial Chaos-Based Uncertainty Quantification and Sensitivity Analysis Using Weighted Approximate Fekete Points. *Int. J. Numer. Method. Biomed. Eng.*, 2020. **36**(11): e3395.

[2] Maas, S.A. *Febio Uncertainsci*. Available from: https://github.com/febiosoftware/FEBioUncertainSCI.

Table A.1 | Minimum and maximum parameter values for the sensitivity analysis.

	Parameter									
	A Direction							**B Direction**		
	c **(Pa)**	m	g_1	g_2	g_3	g_4	g_5	ξ **(Pa)**	α	β
Minimum	1	-30	0.01	0.01	0.01	0.01	0.1	10	0.01	2
Maximum	10,000	30	5	5	50	5	200	10,000	250	10

Table A.2 | Global sensitivity values for Ogden and Prony series parameters.

Parameter	Strain Rate (s^{-1})							
	0.025	**0.25**	**2.5**	**12.5**	**50**	**100**	**125**	**250**
c	6.2E-1	6.1E-1	5.9E-1	5.8E-1	5.9E-1	6.1E-1	6.0E-1	5.6E-1
m	4.1E-01	3.3E-1	3.3E-1	2.2E-1	1.9E-01	2.0E-1	2.0E-1	2.5E-1
$\mathbf{g_1}$	9.5E-2	1.8E-1	4.3E-2	1.2E-2	5.0E-3	7.0E-3	8.6E-3	6.0E-2
$\mathbf{g_2}$	1.0E-2	1.4E-2	2.6E-2	9.6E-3	5.1E-3	7.6E-3	1.1E-2	8.6E-2
$\mathbf{g_3}$	8.8E-3	2.0E-2	1.5E-1	3.1E-1	3.1E-1	2.7E-1	2.6E-1	2.0E-1
$\mathbf{g_4}$	1.2E-2	4.1E-3	2.0E-3	1.7E-3	1.3E-3	4.0E-3	7.5E-3	7.0E-2
$\mathbf{g_5}$	1.0E-2	4.9E-3	2.2E-3	4.0E-3	1.2E-2	3.4E-2	5.2E-2	1.4E-1

Table A.3 | Global sensitivity values for Prony series parameters.

Parameter	Strain Rate (s^{-1})							
	0.025	**0.25**	**2.5**	**12.5**	**50**	**100**	**125**	**250**
$\mathbf{g_1}$	9.7E-1	8.5E-1	1.7E-1	2.6E-2	1.4E-2	1.2E-1	2.4E-2	5.5E-3
$\mathbf{g_2}$	1.3E-2	6.2E-2	1.0E-1	2.4E-2	1.5E-2	9.5E-2	2.0E-2	4.9E-3
$\mathbf{g_3}$	1.4E-2	8.5E-2	7.3E-1	9.4E-1	9.0E-1	9.0E-1	9.2E-1	3.3E-1
$\mathbf{g_4}$	1.4E-6	8.7E-6	9.9E-5	3.1E-4	2.9E-3	9.7E-2	1.8E-2	3.3E-3
$\mathbf{g_5}$	2.2E-5	1.4E-4	1.6E-3	5.9E-3	7.8E-2	1.2E-1	1.4E-1	8.3E-1

Table A.4 | Global sensitivity values for fiber model parameters in the B direction at a strain rate of 0.025 s^{-1}

Parameter	**Global Sensitivity**
α	1.2E-1
β	8.7E-1
ξ	2.5E-1

APPENDIX B

COMPARISON OF EXPERIMENTAL TISSUE STIFFNESS VALUES TO LITERATURE

To contextualize the experimental brain tissue values reported here, we present stiffness values from the experiments in Chapters 3 and 4 compared to values from shear experiments on brain tissue from literature, as shown in Figure B.1. Linear stiffnesses values from all regions evaluated in Chapter 3 as well as dynamic moduli values for all regions and directions evaluated in Chapter 4 are compared with reported stiffness values from Arbogast and Margulies [1] (porcine brainstem tissue tested in 2 directions in oscillatory shear), Rashid et al. [2] (ramp shear tests on porcine cerebral tissue), Thibault and Margulies [3] (oscillatory shear tests on porcine brain tissue), Nicolle et al. [4] (oscillatory shear tests on porcine cerebral tissue at low frequencies with high applied strain and high frequencies with very low applied strain), Darvish and Crandall [5] (oscillatory shear tests on bovine cerebral tissue), Gipple and Haslach [6] (oscillatory shear tests on murine cerebral tissue), Bilston et al. 1998 [7] (oscillatory shear tests on bovine cerebral tissue), Brands et al. [8] (oscillatory shear tests on porcine cerebral tissue), Chatelin et al. [9] (oscillatory shear tests on brainstem and cerebrum samples from juvenile pigs), and Bilston et al. 2001 [10] (oscillatory shear tests on bovine cerebral tissue).

Experimental derived stiffness values from both Chapters 3 and 4 fall in the same order of magnitude as those reported by Rashid et al., Darvish and Crandall, Chatelin et al., Arbogast and Margulies, and Brands et al. Additionally, stiffnesses for the cerebral and cerebellar tissue from Chapters 3 and 4 share a similar response, suggesting that the difference in shear testing methods between the two chapters produce similar results. All experimental stiffness values are noticeably softer than values reported by Bilston et al., Nicolle et al., and Gipple and Haslach. This variation in results may be due to differences in species, age, storage conditions, and testing conditions, suggesting the importance of considering these factors both when designing experiments and picking material models for FE simulations.

References

[1] Arbogast, K.B. and S.S. Margulies, Material Characterization of the Brainstem from Oscillatory Shear Tests. *J. Biomech.*, 1998. **31**(9): 801-807.

[2] Rashid, B., M. Destrade, and M.D. Gilchrist, Mechanical Characterization of Brain Tissue in Simple Shear at Dynamic Strain Rates. *J. Mech. Behav. Biomed. Mater.*, 2013. **28**: 71-85.

[3] Thibault, K.L. and S.S. Margulies, Age-Dependent Material Properties of the Porcine Cerebrum: Effect on Pediatric Inertial Head Injury Criteria. *J. Biomech.*, 1998. **31**(12): 1119-26.

[4] Nicolle, S., et al., Shear Linear Behavior of Brain Tissue over a Large Frequency Range. *Biorheology*, 2005. **42**(3): 209-223.

[5] Darvish, K.K. and J.R. Crandall, Nonlinear Viscoelastic Effects in Oscillatory Shear Deformation of Brain Tissue. *Med Eng Phys*, 2001. **23**(9): 633-645.

[6] Gipple, J.M. and H.W. Haslach, Jr., Damage to the Rat Cerebrum under in Vitro Sinusoidal Translational Shear Deformation. *J. Mech. Behav. Biomed. Mater.*, 2020. **110**: 103969.

[7] Bilston, L., Z. Liu, and N. Phan-Thien, Linear Viscoelastic Properties of Bovine Brain Tissue in Shear. *Biorheology*, 1997. **34**(6): 377-385.

[8] Brands, D.W., P.H. Bovendeerd, and G.W. Peters, *Finite Shear Behavior of Brain Tissue under Impact Loading*, in *ASME International Mechanical Engineering Congress and Exposition*. 2000, American Society of Mechanical Engineers: Orlando, Florida, USA. p. 175-88.

[9] Chatelin, S., et al., Towards Child Versus Adult Brain Mechanical Properties. *J. Mech. Behav. Biomed. Mater.*, 2012. **6**: 166-173.

[10] Bilston, L., Z. Liu, and N. Phan-Thien, Large Strain Behaviour of Brain Tissue in Shear: Some Experimental Data and Differential Constitutive Model. *Biorheology* 2001. **38**(4): 335-45.

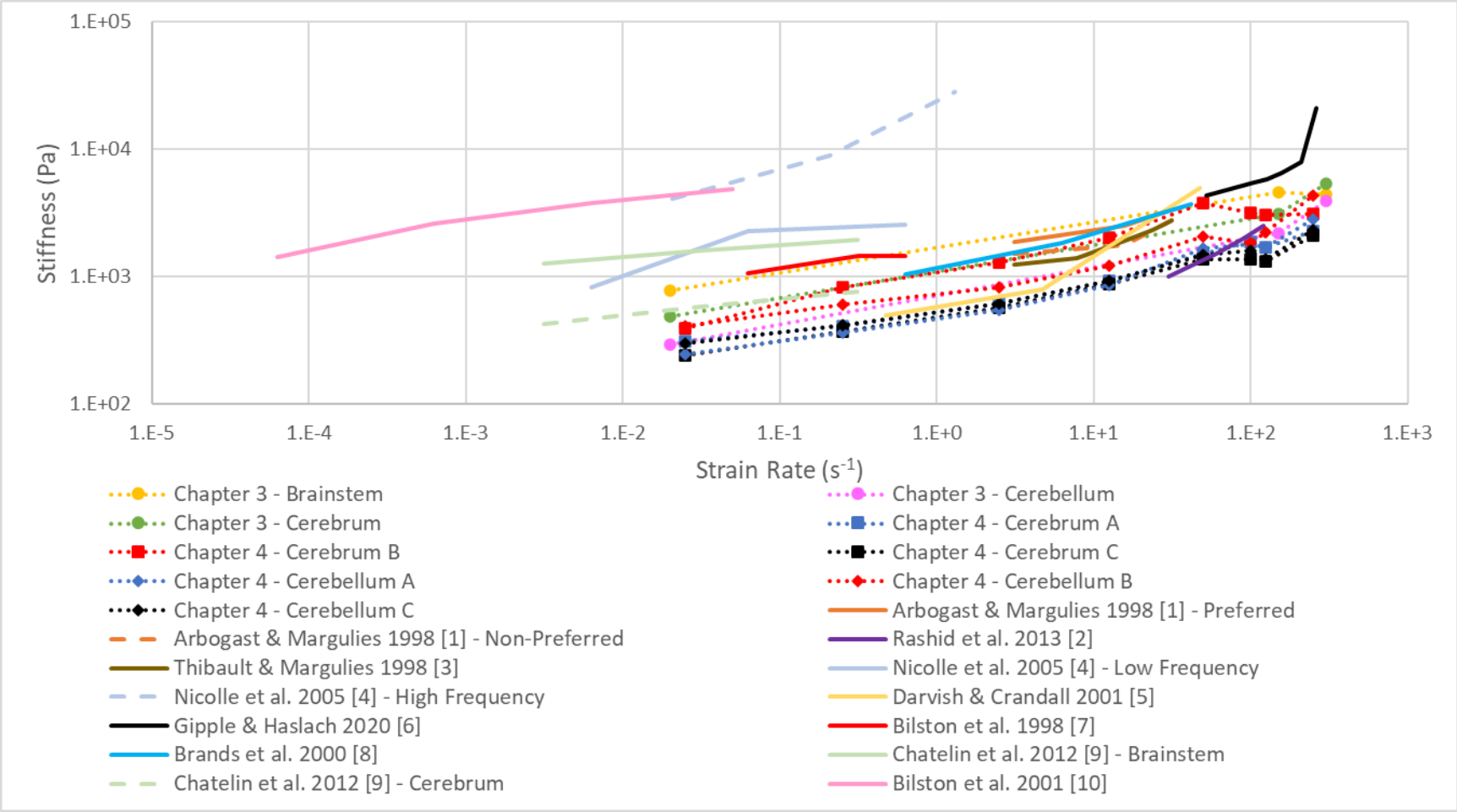

Figure B.1 | Comparison of experimentally derived stiffness and dynamic modulus values from Chapter 3 and Chapter 4, respectively, compared with selected stiffness or dynamic modulus values from literature.